

TOPICS IN QUANTUM NANOSTRUCTURE
PHYSICS: SPIN-ORBIT EFFECTS AND
FAR-INFRARED RESPONSE

TEMES DE FÍSICA DE NANOESTRUCTURES
QUÀNTIQUES: EFECTES D'SPIN-ÒRBITA I
RESPOSTA EN L'INFRAROIG LLUNYÀ

PER EN

FRANCESC MALET I GIRALT

TESI

PRESENTADA PER A OPTAR AL GRAU DE
DOCTOR PER LA UNIVERSITAT DE BARCELONA

Maig de 2008

Programa de Doctorat
Física Avançada
del Departament d'Estructura i Constituents de la Matèria.
Bienni 2005-2007.

Universitat de Barcelona.

El Doctor Martí Pi i Pericay, del Departament d'Estructura i Constituents de la Matèria de la Universitat de Barcelona

CERTIFICA:

Que la memòria presentada pel llicenciat Francesc Malet i Giralt amb títol “Topics in quantum Nanostructure Physics: Spin-Orbit effects and Far-Infrared Response” ha estat realitzada sota la seva direcció i constitueix la Tesi Doctoral de l'esmentat llicenciat, autoritzant-ne la presentació mitjançant el present escrit.

Barcelona, Maig de 2008.

Martí Pi i Pericay

Agraïments

En primer lloc, vull donar les gràcies a en Martí Pi per haver-me donat l'oportunitat de realitzar aquesta tesi doctoral sota la seva tutela i, amb no menys motius, a qui perfectament podria constar com a segon director o com a tutor d'aquesta, en Manuel Barranco. A tots dos els agraeixo enormement l'haver-me acollit al seu grup de recerca, així com el suport, disponibilitat, confiança, paciència i valuosos consells que han sabut donar-me i oferir-me durant aquests anys.

També vull agrair a l'Enrico Lipparini, i extensivament a la seva família, l'hospitalitat i amabilitat en les meves estades a Trento (Itàlia). Exactament el mateix vull dir d'en Llorenç Serra quan he estat treballant amb ell a Palma de Mallorca. Tots dos també m'han aconsellat i ajudat quan ha estat necessari i, sens dubte, les discussions que amb ells he tingut sobre molts dels temes que componen aquesta tesi m'han resultat molt profitoses.

A en Ricardo Mayol li vull agrair, a més de la seva amabilitat durant la tutela del D.E.A, la contínua disponibilitat per intentar resoldre tot tipus d'incidències informàtiques que han anat sorgint durant tot aquest temps treballant amb la *carraca* que d'ell vaig heretar.

I, finalment, als meus bromistes companys de despatx: Xavi, Alberto, Mariona, Víctor, Marta; així com a d'altres amics i companys de Departament com en Pol, la Maria o en Dani, i per descomptat als fets durant la llicenciatura, els agraeixo les bones estones passades plegats en tot aquest temps a la Facultat.

A la meua mare

A la memòria del meu avi

Contents

Introducció	3
1 Ground state and dipole response of quantum ring systems	7
1.1 Density Functional Theory	7
1.1.1 The Local Spin-Density Approximation	9
1.1.2 Time-Dependent Local Spin-Density Functional Theory	12
1.2 Single quantum rings under electric and magnetic fields	17
1.2.1 Ground state	18
1.2.2 Density dipole response	25
1.3 Vertically coupled quantum rings	25
1.3.1 Homonuclear quantum ring molecules	26
1.3.2 Heteronuclear quantum ring molecules	29
1.4 Concentric quantum rings	33
1.4.1 Variable inter-ring distance	34
1.4.2 Variable perpendicular magnetic field	42
2 Spin-orbit effects in quantum nanostructures	49
2.1 Quantum wells submitted to perpendicular magnetic fields	51
2.1.1 Single-particle states	51
2.1.2 Electromagnetic-wave excitations	58
2.2 Exchange-correlation effects in quantum wires submitted to in-plane magnetic fields	64
2.2.1 Noncollinear LSDA	65
2.2.2 Subband structure	67
2.2.3 Conductance	74
A Quantum wells with spin-orbit interaction under tilted magnetic fields	79
B Analytical second-order perturbation theory solution for noninteracting quantum wires	81
Resum, conclusions i perspectives	85

Bibliography

93

Curriculum Vitae

103

Introducció

El *fenòmen Nano* ha anat traspasant durant els últims anys les fronteres de la comunitat científica i, avui en dia, és difícil no haver sentit a parlar alguna vegada de conceptes com les nanopartícules, els nanoxips, els nanofàrmacs o els nanoaliments, només per donar-ne alguns exemples. Prova d'aquesta moda és el fet que marques comercials fabricants de cotxes o reproductors de música digital s'hi han inspirat per donar nom a un dels seus –molt petits– models. Sens dubte, els ressò dels continus avanços en Nanociència i en la seva vessant aplicada, la Nanotecnologia, així com de les seves potencials aplicacions en un futur pròxim en camps tan diversos com la computació quàntica, el tractament contra el càncer o múltiples indústries, han contribuït a aquesta divulgació popular.

La Nanotecnologia és l'estudi, disseny, síntesi, manipulació i aplicació de materials i dispositius mitjançant el control de la Matèria a l'escala del nanòmetre (la mil·lionèsima d'un mil·límetre) o, dit d'una altra manera, dels àtoms i les molècules. Aquesta nova i emergent ciència aplicada barreja múltiples disciplines científico-tècniques com la Física, la Química, la Bioquímica, la Biologia Molecular, l'Electrònica o la Informàtica i per als seus propòsits contempla l'utilització, entre d'altres, de metalls, plàstics, carboni, cadenes d'ADN o semiconductors. La branca basada en aquests últims i en concret les seves peces bàsiques, les anomenades *nanostructures semiconductoras*, són l'objecte d'estudi d'aquesta tesi.

Essencialment, aquestes estructures es poden definir com a sistemes semiconductors que generalment contenen un cert nombre d'electrons de conducció (per això sovint se les anomena *nanostructures electròniques*) i on almenys una de les tres dimensions de l'espai es troba confinada a l'escala nanomètrica. La seva fabricació es basa en el fet que l'estructura de bandes dels semiconductors varia d'un compost a un altre. Per tant, quan dues capes semiconductoras diferents es posen en contacte a la interfície hi ha canvis abruptes en algunes propietats bàsiques. Això s'il·lustra esquemàticament als panells superior i central de la figura 1, on s'agafen com a exemples el AlGaAs i el GaAs, dos dels compostos més utilitzats en la fabricació de nanoestructures. En particular, apareix un gradient de potencial químic –energia de Fermi (ε_F) en el llenguatge de semiconductors– que origina un camp elèctric i fa que electrons del material amb ε_F més gran flueixin cap a l'altre fins que el sistema uniformitza el seu potencial químic. La càrrega positiva (negativa) resultant al AlGaAs (GaAs) fa pujar (baixar) la banda de conducció (ε_C) respecte al nivell de Fermi, tal i com passa quan es dopa un semiconductor amb impureses

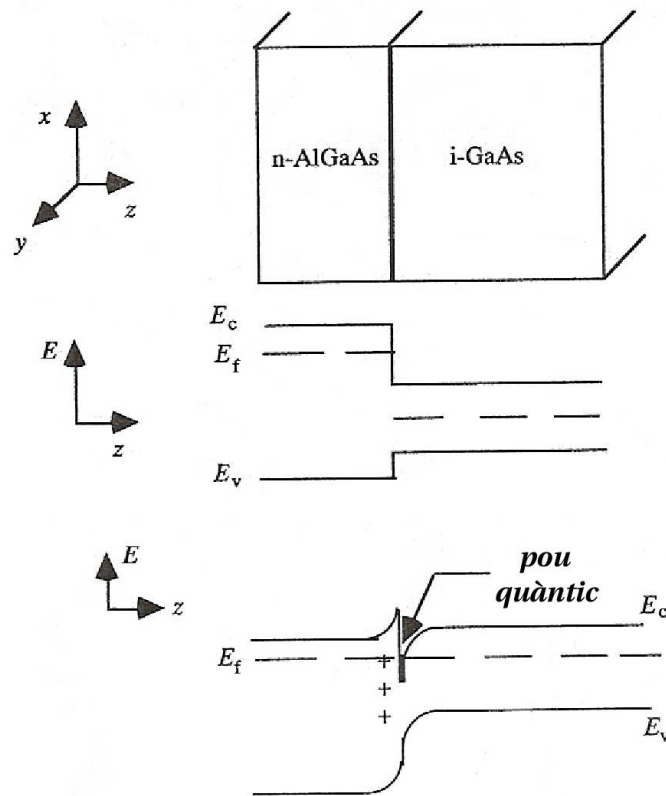


Figura 1: Imatge esquemàtica de la formació d'un pou quàntic

acceptadores (donadores), i dóna lloc al fet que en una estreta zona (que usualment es pren al llarg de l'eix z i s'anomena direcció de creixement) dins del GaAs es compleixi la condició $\varepsilon_F < \varepsilon_C$, formant-se així un pou de potencial on electrons de conducció queden atrapats (panell inferior de la figura 1).

Si es realitza un apil·lament de diverses capes, amb gruix i composició adequadament seleccionats, es pot controlar la formació d'un pou de només uns nanòmetres de gruix en una de les capes internes. El fet que aquestes dimensions siguin comparables o inferiors a la longitud de de Broglie dels electrons en aquests sistemes –uns 50 nm en el cas del GaAs– fa que els efectes quàntics en la dimensió confinada siguin importants i es parli així de la formació d'un pou quàntic (*quantum well*) o d'un *gas d'electrons quasi-bidimensional*. Com que les altres dues dimensions són diversos ordres de magnitud més grans, el pou quàntic es pot imaginar com un 'full de paper semiconductor' sobre el pla del qual electrons de conducció tenen limitat el seu moviment. La seva realització experimental va ser duta a terme per primera vegada a principis dels anys 70 per part de grups d'investigació dels Laboratoris Bell i IBM mitjançant tècniques epitaxials de creixement que permeten anar dipositant capes monoatòmiques de material l'una sobre de l'altra i, entre d'altres aplicacions, van servir com a base per als díodes làser.

Ben aviat es va pensar en anar més enllà i considerar la possibilitat de crear objectes de dimensionalitat més reduïda 'retallant' sobre aquests 'fulls'. Des de mitjans dels anys 80, la constant evolució de les tècniques nanolitogràfiques i de nanograt ha permès

disposar de les ‘tisores’ adequades per aconseguir aquest objectiu i s’han pogut fabricar nanoestructures cada vegada més petites i complexes. Així, confinant els electrons del pou quàntic inicial en una dimensió addicional es van obtenir els *fil·ls quàntics*, ‘tires de paper’ amb una amplada característica de l’ordre del centenar de nanòmetres. Estenent el confinament a les tres dimensions de l’espai es van crear els *punts quàntics*, que en el cas de ser circulars acostumen a tenir un diàmetre de l’ordre dels 10-100 nm. I, més tard, els ‘discs’ formats per aquests últims es van poder ‘perforar’ mitjançant tècniques d’oxidació utilitzant la punta d’un microscopi de força atòmica, donant lloc així als anomenats *anells quàntics*. Recentment, a més, utilitzant mètodes de creixement autoordenat s’han pogut obtenir també sistemes d’anells concèntrics i de verticalment acoblats. Bàsicament, aquesta tècnica consisteix en el creixement de capes successives amb diferent paràmetre de xarxa. Això pot provocar la inestabilitat de l’estat homogeni inicial del sistema, donant lloc a una transició de fase que el porta a un estat inhomogeni i forma espontàniament punts quàntics sobre una de les capes. Si aquesta última es cobreix després amb una de nova de composició adequada, es pot modificar la topologia dels punts i convertir-los en anells. Com que es troben confinats en les tres dimensions espacials, els punts i els anells quàntics es poden pensar com a sistemes tancats i se’ls sol caracteritzar pel nombre N d’electrons de conducció que contenen. En canvi, els pous i fil·ls quàntics tenen almenys una dimensió lliure i que a la pràctica es considera infinita; així, per a aquests sistemes s’acostuma a prendre el nombre d’electrons també com infinit i a descriure’ls en termes de la seva densitat, que és finita.

Una propietat important de totes aquestes estructures és que, a causa de les característiques del seu procés de fabricació, així com de la pròpia natura dels materials utilitzats, presenten asimetries inherents. Aquestes poden donar lloc a la presència de camps elèctrics que, com a efecte de la Relativitat Especial, es transformen en camps magnètics en el sistema de referència dels electrons, interaccionant amb els seus spins, acoblant-los al seu moment i donant origen a l’anomenada *interacció d’spin-òrbita*. D’entre les diferents possibles fonts n’hi ha dues que es consideren especialment importants en aquests sistemes. En primer lloc, la majoria de materials més utilitzats en la fabricació de nanoestructures, com per exemple el GaAs, són semiconductors amb estructura cristal·lina Zinc Blenda, que no té centre d’inversió. Aquesta asimetria dóna lloc a l’anomenada contribució d’spin-òrbita de Dresselhaus. En segon lloc, el pou quàntic que origina el gas quasi-bidimensional inicial no és en general simètric –com es pot intuir de la figura 1– i produeix el conegut com acoblament de Bychkov-Rashba, que té una propietat molt interessant: la seva intensitat pot ser controlada externament mitjançant l’aplicació d’un voltatge extern. Això el fa d’especial potencial aplicació en *Spintrònica*, una nova tecnologia basada en el control, la manipulació i el transport de l’spin electrònic i que té com a dispositiu més representatiu –encara només a nivell teòric– l’anomenat transistor d’spin, basat en un fil quàntic amb interacció de Bychkov-Rashba i que generalitza l’usual transistor d’efecte de camp.

Aquesta tesi és un resum dels treballs publicats llistats al *Curriculum Vitae* que

s'adjunta al final de la memòria i es divideix en dos capítols principals. En el primer s'estudia l'estat fonamental i la resposta dipolar de sistemes formats per anells quàntics amb un nombre d'electrons variable. En una primera part es considera un sol anell sotmès simultàniament a un camp elèctric en el pla i a un camp magnètic perpendicular a aquest. Després es consideren dos sistemes dobles d'anells quàntics; en primer lloc, i en analogia amb una molècula real, un compost per dos anells acoblats verticalment amb una distància de separació variable. En segon lloc, un altre format per dos anells concèntrics, considerant dues situacions: primer a camp aplicat nul i variant el radi de l'anell més gran, i després fixant els dos radis i estudiant el sistema en funció d'un camp magnètic aplicat perpendicularment al pla dels anells. Per tot això, s'utilitza el formalisme de la teoria del funcional de la densitat en la seva aproximació local per obtenir els estats fonamentals, i la seva versió dependent del temps per als càlculs de les respostes dipolars. Una breu introducció als dos formalismes es fa abans de mostrar els respectius resultats.

El segon capítol s'ocupa de l'estudi dels efectes de la interacció d'spin-òrbita en pous i fils quàntics sotmesos a camps magnètics externs. Primer, mitjançant un tractament analític aproximat, es calculen les correccions de Rashba i de Dresselhaus a les freqüències de ciclotró i de Larmor, als nivells de Landau i a les excitacions induïdes per ones electromagnètiques externes en pous quàntics. Després es consideren fils quàntics sotmesos a camps magnètics continguts en el pla del sistema, estudiant-s'hi els efectes d'intercanvi-correlació per tal de veure si se n'alteren els resultats coneguts sense aquesta interacció. Com es veurà, l'acoblament d'spin-òrbita fa que en general les nanoestructures continguin spins no colineals. En aquestes condicions el formalisme utilitzat al primer capítol no és vàlid i cal utilitzar-ne una generalització aplicable a aquestes situacions, de la qual es fa una introducció al principi de la pertinent secció.

Un resum i les conclusions extretes del treball realitzat s'exposen al final de la tesi, així com les seves possibles continuacions de cara un futur immediat. Finalment, s'inclou un apèndix ampliant alguns dels resultats presentats al capítol 2.

Chapter 1

Ground state and dipole response of quantum ring systems

Because of their particular topology, quantum ring (QR) systems exhibit unique physical phenomena that make them very interesting from both a purely theoretical and a technological point of view. In this sense they allow, for example, the observation of Aharonov-Bohm oscillations [Aha59] and related effects such as the so-called ‘persistent current’ [But83, Cha94], which is one of the best examples of quantum mechanical phase coherence. Also, and similarly to quantum dots (QDs), they are good candidates for being implemented in quantum computation schemes [Fol05]. Understanding the electronic properties of these nanostructures is essential for their eventual application in practical devices.

In this chapter we address the ground state (gs) and the dipole response of three quantum ring systems: a single ring and two quantum ring ‘diatomic molecules’, first vertically and then concentrically coupled, as a function of different parameters such as the electron number, the intensity of externally applied electric and magnetic fields and the inter-ring distance. For this purpose, we employ one of the most successful and accurate approaches when dealing with electronic nanostructures: the Density Functional Theory (DFT).

1.1 Density Functional Theory

It is considered that DFT as we know it today was born in 1964 with the famous Physical Review by Hohenberg and Kohn [Hoh64]. In it, the authors proved in a rigorous mathematical way that the full many-particle ground state of an inhomogeneous electron gas, including the *full* electron-electron (e-e) interaction, can be described by a unique functional of the density, which in turn obeys a variational principle. That is, for the correct $\rho_0(\mathbf{r})$, $E[\rho_0(\mathbf{r})]$ equals the ground state energy E_0 . These are known as the Hohenberg-Kohn (HK) theorems, and represented two big steps forward relative to other well-known approaches, such as the Hartree or the Hartree-Fock ones. On the one hand, the replace-

ment of the electronic wave function by the electronic density as basic quantity constituted a high simplification of the problem in the computational sense, since the number of variables was reduced from $3N$ –three spatial components for each of the N electrons– to only the three spatial components of the density, which in addition is a simpler both conceptually and practically quantity to deal with. On the other hand, the exchange-correlation part of the electron-electron interaction, neglected or only partially taken into account in the above-mentioned approaches, is completely treated in the Kohn-Sham (KS) formalism, although in an approximate –yet very precise– way. Indeed, the HK theorems state the *existence* of a one-to-one functional correspondence between the density and the Hamiltonian of the system but do not provide any clue on its exact explicit form, which is actually unknown and therefore must be approximated. This functional is usually written as

$$E[\rho(\mathbf{r})] = T_0[\rho(\mathbf{r})] + \frac{1}{2} \int \rho(\mathbf{r}) V_H(\mathbf{r}) d\mathbf{r} + \int \rho(\mathbf{r}) V_{conf}(\mathbf{r}) d\mathbf{r} + E_{xc}[\rho(\mathbf{r})], \quad (1.1)$$

where $T_0[\rho(\mathbf{r})]$ is the kinetic energy of an auxiliary system of *noninteracting* particles with the same density $\rho(\mathbf{r})$ of the real system and $V_H(\mathbf{r}) = \frac{e^2}{\epsilon} \int d\mathbf{r}' \rho(\mathbf{r}')/|\mathbf{r} - \mathbf{r}'|$ and $V_{conf}(\mathbf{r})$ are, respectively, the usual Hartree and confining potentials, the shape of the latter depending of course on the system under study. Thus, all the unknown quantities, namely the exchange-correlation contribution and the difference between the exact kinetic energy and that of the auxiliary system are contained in the so-called *exchange-correlation functional* E_{xc} . For the noninteracting system the kinetic energy and the density can be written in terms of independent-particle orbitals φ_i as

$$T_0 = \sum_{i=1}^N \int \varphi_i^*(\mathbf{r}) \left(-\frac{\hbar^2}{2m} \nabla^2 \right) \varphi_i(\mathbf{r}) d\mathbf{r} = \frac{\hbar^2}{2m} \sum_{i=1}^N \int |\nabla \varphi_i(\mathbf{r})|^2 d\mathbf{r} \quad (1.2)$$

and

$$\rho(\mathbf{r}) = \sum_{i=1}^N |\varphi_i(\mathbf{r})|^2, \quad (1.3)$$

respectively.

One year after the publication of the HK theorems, Kohn and Sham [Koh65] derived, from the stationary property of $E[\rho]$ subjected to the particle-number conservation, the selfconsistent equations that provide the single-particle (sp) wave functions and energies of the ground state, the so-called Kohn-Sham equations:

$$\left[\frac{\delta T_0}{\delta \varphi_i^*} + V_{conf} + V_H + \frac{\delta E_{xc}}{\delta \rho} \right] \varphi_i = \varepsilon_i \varphi_i, \quad (1.4)$$

where ε_i is the energy of the i th sp orbital φ_i . Notice that if the exact form of E_{xc} and its variation with respect the density were known, the Kohn-Sham formalism would lead

to the exact energy of the system. Unfortunately, this is not the case and therefore this part of the functional has to be approximated. Once this is done in a suitable way, by selfconsistently solving the KS equations one can obtain the ground state density –Eq. (1.3)– and total energy –Eq. (1.1)– of the *real* N -electron system. The latter is also given by the alternative expression [Lun83]

$$E[\rho(\mathbf{r})] = \sum_{i=1}^N \varepsilon_i - \frac{1}{2} \int \rho(\mathbf{r}) V_H(\mathbf{r}) d\mathbf{r} + E_{xc}[\rho(\mathbf{r})] - \int \frac{\delta E_{xc}}{\delta \rho} \rho(\mathbf{r}) d\mathbf{r} . \quad (1.5)$$

A numerical comparison between Eqs. (1.1) and (1.5) is often taken as a convergence criterion and as a matter of fact we have used it to check the accuracy of all the DFT results presented in this thesis.

The quest for ever more accurate and more widely applicable exchange-correlation functionals is one of the main tasks in DFT. Here we make use of an extremely simple –though surprisingly accurate– approximation for E_{xc} that constitutes the core of most modern DFT codes: the *Local Spin-Density Approximation*.

1.1.1 The Local Spin-Density Approximation

If one considers that both the charge and the spin density vary slowly from one point of the system to another, it can be assumed that, in the vicinity of a given point \mathbf{r} , the (*inhomogeneous*) electron gas can be well approximated by an infinite *homogeneous* one –for which very accurate expressions of the exchange-correlation functional are known– with the same density $\rho(\mathbf{r})$ and magnetization $m(\mathbf{r})$ of the actual system. Indeed, it is well known that the task of determining good approximations for the exchange-correlation energy is much simpler if the latter enters the game together with the density. This approach is therefore referred to as the *Local Spin-Density Approximation* (LSDA) and allows one to write E_{xc} in the simple form

$$E_{xc}^{LSDA}[\rho(\mathbf{r}), m(\mathbf{r})] = \int \rho(\mathbf{r}) \mathcal{E}_{xc}[\rho(\mathbf{r}), m(\mathbf{r})] d\mathbf{r} , \quad (1.6)$$

where $\mathcal{E}_{xc}[\rho(\mathbf{r}), m(\mathbf{r})]$ is the exchange-correlation energy per particle of an homogeneous, partially spin-polarized system with spin-up and spin-down densities n_\uparrow , n_\downarrow that define the electron density $\rho = n_\uparrow + n_\downarrow$ and the spin magnetization $m = n_\uparrow - n_\downarrow$. Notice that the latter should in principle be a vector but one can write it as a scalar since it is assumed that the electrons have a common and constant spin quantization axis, namely the z -direction. $\mathcal{E}_{xc}[\rho(\mathbf{r}), m(\mathbf{r})]$ can be further split into exchange and correlation contributions,

$$\mathcal{E}_{xc}[\rho(\mathbf{r}), m(\mathbf{r})] = \mathcal{E}_x[\rho(\mathbf{r}), m(\mathbf{r})] + \mathcal{E}_c[\rho(\mathbf{r}), m(\mathbf{r})] , \quad (1.7)$$

with its functional form depending on the dimensionality of the system under study. For the exchange contribution one has the local analytical expression based on the Thomas-Fermi-Dirac model, given by [Lip03]

$$\mathcal{E}_x [r_s, \xi] = \left\{ \begin{array}{l} -\frac{2\sqrt{2}}{3\pi r_s} \left[(1 + \xi)^{3/2} + (1 - \xi)^{3/2} \right] \quad (2D) \\ -\frac{3}{8\pi r_s} \left(\frac{9\pi}{4} \right)^{1/3} \left[(1 + \xi)^{4/3} + (1 - \xi)^{4/3} \right] \quad (3D) \end{array} \right\}, \quad (1.8)$$

which interpolates [Bar72] between the fully polarized ($\xi \equiv m/\rho=1$) and unpolarized ($\xi=0$) homogeneous electron gas and where r_s is the Wigner-Seitz radius, defined by

$$r_s = \left\{ \begin{array}{l} (1/\pi\rho)^{1/2} \quad (2D) \\ (3/4\pi\rho)^{1/3} \quad (3D) \end{array} \right\}. \quad (1.9)$$

For the correlation term there exist different proposals. We shall use the parametrization by Tanatar and Ceperley [Tan89], given by

$$\mathcal{E}_c [r_s, \xi] = a_0^i \frac{1 + a_1^i x}{1 + a_1^i x + a_2^i x^2 + a_3^i x^3} \quad (1.10)$$

with $x \equiv \sqrt{r_s}$ when considering 2D systems, and the one by Perdew and Zunger [Per81]

$$\mathcal{E}_c [r_s] = \left\{ \begin{array}{l} \gamma_i / (1 + \beta_1^i \sqrt{r_s} + \beta_2^i r_s) \quad \text{if } r_s \geq 1 \\ A_i \ln r_s + B_i + C_i r_s \ln r_s + D_i r_s \quad \text{if } r_s < 1 \end{array} \right\}, \quad (1.11)$$

for three-dimensional approaches. The different parameters appearing in both functionals are taken from the Monte Carlo calculations by Ceperley and coworkers [Cep78] for the fully polarized ($i=P$) and unpolarized ($i=U$) cases. It is worth to point out that a more accurate expression for \mathcal{E}_{xc} has recently become available [Att02]. However, whereas a very precise description of the exchange-correlation energy is needed for a quantitative description of the Wigner crystallization at low electron densities, we do not believe that the use of this new parametrization might have introduced substantial changes in the results we shall discuss here.

Once the functional form of $\mathcal{E}_{xc}[\rho(\mathbf{r}), m(\mathbf{r})]$ is obtained, its variations with respect to the electron density and spin magnetization taken at the ground state,

$$V_{xc} = \left. \frac{\partial \mathcal{E}_{xc}(\rho, m)}{\partial \rho} \right|_{gs}; \quad W^{xc} = \left. \frac{\partial \mathcal{E}_{xc}(\rho, m)}{\partial m} \right|_{gs}, \quad (1.12)$$

define the so-called exchange-correlation potentials.

Taking $z = 0$ as the plane of symmetry of the system, which we consider to be submitted to an in-plane electric field \mathcal{E} (e.g. along the x -axis) and a perpendicular magnetic field B , within the *effective mass, dielectric constant approximation* [Wen99], the Kohn-Sham equations read

$$\left\{ -\frac{\hbar^2}{2m} \mathbf{P}^2 + \frac{e}{\epsilon} \mathcal{E} x + V_{conf}(r, z) + V_H + V_{xc} + \left[W^{xc} + \frac{1}{2} g^* \mu_B B \right] \sigma_z \right\} \varphi_\alpha(\mathbf{r}) = \epsilon_\alpha \varphi_\alpha(\mathbf{r}), \quad (1.13)$$

where $\mathbf{P} = -i\hbar\nabla + e\mathbf{A}/c$ represents the canonical momentum in terms of the vector potential \mathbf{A} , $\mu_B = \hbar e / (2m_e c)$ is the Bohr magneton and σ_z is the z -component of the

	H	GaAs
m^*	1	0.067
ϵ	1	12.4
length scale ($a_0 = \frac{\hbar^2}{m_e e^2}$)	$\sim 0.05 \text{ nm}$	$a_0^* = \frac{\epsilon}{m^*} a_0 \sim 10 \text{ nm}$
energy scale ($E_0 = \frac{e^2}{a_0}$)	$\sim 27.2 \text{ eV}$	$E_0^* = \frac{m^*}{\epsilon^2} E_0 \sim 12 \text{ meV}$

Table 1.1: Parameters for the Hydrogen atom and for the GaAs.

Pauli spin-vector operator $\boldsymbol{\sigma}$. The quantities $m \equiv m^* m_e$, g^* and ϵ are, respectively, the effective electron mass, gyromagnetic factor and dielectric constant, and depend on the actual semiconductor materials containing the nanostructure. For numerical applications, throughout this thesis we have considered GaAs/Al_{0.3}Ga_{0.7}As systems, whose corresponding values are given in table 1.1, compared to those for the Hydrogen atom. Clearly, the effective quantities yield big differences in the typical length and energy scales, implying e.g. that interactions such as the Zeeman one, contrarily as usually done in atomic systems, can no longer be treated as small perturbations in semiconductor nanostructures.

The presence of an in-plane electric field breaks the cylindrical symmetry of quantum rings and the resolution of Eq. (1.13) in Cartesian coordinates is unavoidable. However, if $\mathcal{E} = 0$ the system recovers its symmetry and one can write the KS orbitals as $\varphi_{nl\sigma}(r, z, \theta, \sigma) = u_{nl\sigma}(r, z) e^{-il\theta} \chi_\sigma$, $n = 0, 1, 2, \dots$ being the energy-band index, $-l$ the projection of the orbital angular momentum on the symmetry axis with $l = 0, \pm 1, \pm 2, \dots$, and where $\sigma = \uparrow$ (\downarrow) refers to a spin-up (-down) electron. This allows one to write, using effective atomic units $\hbar = e^2/\epsilon = m = 1$ to simplify the expressions, the Kohn-Sham equations in cylindrical coordinates as [Pi98, Rei02, Wen00] :

$$\left[-\frac{1}{2} \left(\frac{\partial^2}{\partial r^2} + \frac{1}{r} \frac{\partial}{\partial r} - \frac{l^2}{r^2} + \frac{\partial^2}{\partial z^2} \right) - \frac{\omega_c}{2} l + \frac{1}{8} \omega_c^2 r^2 + V_{conf}(r, z) \right. \\ \left. + V_H + V_{xc} + \left(W^{xc} + \frac{1}{2} g^* \mu_B B \right) \eta_\sigma \right] u_{nl\sigma}(r, z) = \epsilon_{nl\sigma} u_{nl\sigma}(r, z), \quad (1.14)$$

with $\eta_\sigma = +1$ (-1) for $\sigma = \uparrow$ (\downarrow), $\omega_c = eB/c$ being the cyclotron frequency and where the vector potential has been chosen in the symmetric gauge, namely $\mathbf{A} = B(-y, x, 0)/2$.

It is worth to mention that in the presence of an applied magnetic field the exchange-correlation energy not only depends on $n_{\uparrow, \downarrow}$, but also on the paramagnetic currents within the so-called *Current Spin-Density Functional Theory* (CSDFT) [Vig88], which is better suited than LSDA for high values of B . CSDFT has been applied to study two-dimensional quantum dots and rings [Fer94, Lin01, Pi98, Rei02], and comparisons between the obtained results and those given by LSDA have been made, showing an overall agreement and

indicating that the effects caused by the inclusion of such currents are in general small –see e.g. [Anc03].

1.1.2 Time-Dependent Local Spin-Density Functional Theory

We have seen that by solving the Kohn-Sham equations one is able to find an absolute minimum of the total energy corresponding to a certain value of the electronic density $\rho_0(\mathbf{r})$. When selfconsistency is achieved, the mean field is essentially constant within consecutive numerical iterations and the system remains in this minimum of energy: the ground state. However, one can go beyond this static approach and study excited states of the system induced by the interaction of the latter with a *time-dependent* external perturbation such as, e.g., an electromagnetic field of a certain frequency ω . If this perturbation is weak, the density will start slightly oscillating around the value corresponding to the minimum energy and, since the Kohn-Sham potential depends on the density, it will oscillate as well inducing in turn variations in the density itself. The smallness of the perturbation allows one to use the *linear response theory*, generalizing the formalism of the previous section within the so-called *Time-Dependent LSDA* (TDLSDA).

In the general case the perturbation may be spin-dependent, thus affecting in a different way the n_\uparrow and n_\downarrow densities. It can then be represented by the operator

$$F(\mathbf{r}, t) = \sum_{\sigma\sigma'} f_{\sigma\sigma'}(\mathbf{r}) |\sigma\rangle\langle\sigma'| e^{-i\omega t} + h.c. \quad (1.15)$$

and, if one assumes that the external field induces excitations without involving spin-flip transitions –*longitudinal response*–, for a constant spin-magnetization direction F is diagonal in the two-component Pauli space and therefore we can write its non-temporal dependence as a vector, namely $F(\mathbf{r}) \equiv \begin{pmatrix} f(\mathbf{r})_\uparrow \\ f(\mathbf{r})_\downarrow \end{pmatrix}$.

The perturbed spin- σ density is then

$$n_\sigma(\mathbf{r}, t) = n_{0,\sigma}(\mathbf{r}) + \delta n_\sigma(\mathbf{r}, \omega) e^{-i\omega t} + h.c. , \quad (1.16)$$

$n_{0,\sigma}(\mathbf{r})$ being the corresponding ground-state value. The consequent perturbation in the spin- σ KS potential is of the form

$$\delta V_{KS}^\sigma(\mathbf{r}, t) = \delta V_{KS}^\sigma(\mathbf{r}, \omega) e^{-i\omega t} + h.c. , \quad (1.17)$$

with

$$\delta V_{KS}^\sigma(\mathbf{r}, \omega) = \sum_{\sigma'} \int d\mathbf{r}' \frac{\delta V_{KS}^{\sigma'}(\mathbf{r})}{\delta n_{\sigma'}(\mathbf{r}', \omega)} \delta n_{\sigma'}(\mathbf{r}', \omega) \quad (1.18)$$

and, thus, the *total* contribution of the external perturbation to the spin- σ mean field is

$$V_{pert}^\sigma(\mathbf{r}, t) = (f_\sigma(\mathbf{r}) + \delta V_{KS}^\sigma(\mathbf{r}, \omega)) e^{-i\omega t} + h.c. \equiv V_{pert}^\sigma(\mathbf{r}) e^{-i\omega t} + h.c. . \quad (1.19)$$

The selfconsistent spin- σ -density variation can be easily obtained from ordinary first-order perturbation theory as [Lun83, Raj78]

$$\delta n_\sigma(\mathbf{r}, \omega) = \sum_{\sigma'} \int d\mathbf{r}' \chi_{\sigma\sigma'}^{(0)}(\mathbf{r}, \mathbf{r}'; \omega) V_{pert}^{\sigma'}(\mathbf{r}'), \quad (1.20)$$

where $\chi_{\sigma\sigma'}^{(0)}(\mathbf{r}, \mathbf{r}'; \omega)$ is the so-called free-particle spin-density correlation function, representing the probability amplitude of a change of spin- σ density at \mathbf{r} induced by a change of spin- σ' density at \mathbf{r}' caused by $V_{pert}^{\sigma'}(\mathbf{r}')$. It is obtained from the knowledge of the KS orbitals as

$$\chi_{\sigma\sigma'}^{(0)}(\mathbf{r}, \mathbf{r}'; \omega) = -\delta_{\sigma\sigma'} \sum_{\alpha\beta} \varphi_\alpha^*(\mathbf{r}) \varphi_\beta(\mathbf{r}) \frac{p_\alpha - p_\beta}{\epsilon_\alpha - \epsilon_\beta + \omega + i\gamma} \varphi_\beta^*(\mathbf{r}') \varphi_\alpha(\mathbf{r}'), \quad (1.21)$$

where the label α (β) refers to a sp level with spin σ (σ'), thermal occupation p_α (p_β) and energy ϵ_α (ϵ_β), and where γ is a small imaginary quantity added in order to simplify the analysis of the results, transforming the δ -peaks coming from the denominator poles into Lorentzians. Therefore, one assumes that the electrons respond as free –noninteracting– particles to the total perturbing field, which consists of the external plus the induced one arising from the changes produced by the perturbation in the gs mean field. However, one can also consider interacting electrons responding just to $f_{\sigma'}$ –i.e. omitting the residual interaction $\delta V_{KS}^{\sigma'}/\delta n_\sigma$ in $V_{pert}^{\sigma'}$. This allows to write Eq. (1.20) as

$$\delta n_\sigma(\mathbf{r}, \omega) = \sum_{\sigma'} \int d\mathbf{r}' \chi_{\sigma\sigma'}(\mathbf{r}, \mathbf{r}'; \omega) f_{\sigma'}(\mathbf{r}'), \quad (1.22)$$

where $\chi_{\sigma\sigma'}(\mathbf{r}, \mathbf{r}'; \omega)$ is the so-called TDLSDA spin-density correlation function that is related to the free-particle one through a Dyson-type integral equation:

$$\begin{aligned} \chi_{\sigma\sigma'}(\mathbf{r}, \mathbf{r}'; \omega) &= \chi_{\sigma\sigma'}^{(0)}(\mathbf{r}, \mathbf{r}'; \omega) \\ &+ \sum_{\sigma_1\sigma_2} \int d\mathbf{r}_1 d\mathbf{r}_2 \chi_{\sigma\sigma_1}^{(0)}(\mathbf{r}, \mathbf{r}_1; \omega) K_{\sigma_1\sigma_2}(\mathbf{r}_1, \mathbf{r}_2) \chi_{\sigma_2\sigma'}(\mathbf{r}_2, \mathbf{r}'; \omega). \end{aligned} \quad (1.23)$$

The residual interaction is represented by the kernel $K_{\sigma\sigma'}(\mathbf{r}, \mathbf{r}')$, consisting of the direct Coulomb interaction plus the second-order functional derivative of \mathcal{E}_{xc} with respect to the spin-up and -down electron densities:

$$K_{\sigma\sigma'}(\mathbf{r}_1, \mathbf{r}_2) = \frac{1}{|\mathbf{r}_1 - \mathbf{r}_2|} + \left. \frac{\partial^2 \mathcal{E}_{xc}(\rho, m)}{\partial n_\sigma \partial n_{\sigma'}} \right|_{gs} \delta(\mathbf{r}_1 - \mathbf{r}_2), \quad (1.24)$$

where

$$\begin{aligned} \left. \frac{\partial^2 \mathcal{E}_{xc}}{\partial n_\sigma \partial n_{\sigma'}} \right|_{gs} &= \left. \frac{\partial^2 \mathcal{E}_{xc}}{\partial \rho^2} \right|_{gs} + (\eta_\sigma + \eta_{\sigma'}) \left. \frac{\partial^2 \mathcal{E}_{xc}}{\partial \rho \partial m} \right|_{gs} + \eta_\sigma \eta_{\sigma'} \left. \frac{\partial^2 \mathcal{E}_{xc}}{\partial m^2} \right|_{gs} \\ &\equiv \mathcal{K}(\mathbf{r}) + (\eta_\sigma + \eta_{\sigma'}) \mathcal{M}(\mathbf{r}) + \eta_\sigma \eta_{\sigma'} \mathcal{I}(\mathbf{r}). \end{aligned} \quad (1.25)$$

In this thesis we consider only the dipole responses. Then $F(\mathbf{r})$ is represented, taking e.g. the perturbing field along the x -direction, by the charge-density $D_n = \sum_{i=1}^N x_i$ and spin-density $D_m = \sum_{i=1}^N x_i \sigma_z^i$ dipole operators, which in vectorial form read

$$D_n = x \begin{pmatrix} 1 \\ 1 \end{pmatrix} \quad \text{and} \quad D_m = x \begin{pmatrix} 1 \\ -1 \end{pmatrix} . \quad (1.26)$$

Taking advantage of the circular symmetry of quantum rings they can be rewritten as

$$D_n^{(\pm)} = \frac{r}{2} e^{\mp i\theta} \begin{pmatrix} 1 \\ 1 \end{pmatrix} \quad \text{and} \quad D_m^{(\pm)} = \frac{r}{2} e^{\mp i\theta} \begin{pmatrix} 1 \\ -1 \end{pmatrix} , \quad (1.27)$$

so that $D_n = D_n^{(+)} + D_n^{(-)}$ and analogously for $D_m^{(\pm)}$. Here ‘+’ (‘-’) indicates that the corresponding excitation operator induces a $\Delta l = +1$ (-1) transition.

Equations (1.23) can *in principle* be solved –see below– as a system of matrix equations in coordinate space after performing an angular decomposition of $\chi_{\sigma\sigma'}$ and $K_{\sigma\sigma'}$ of the form

$$\begin{aligned} \chi_{\sigma\sigma'}(\mathbf{r}, \mathbf{r}'; \omega) &= \sum_l \chi_{\sigma\sigma'}^{(l)}(r, r'; \omega) e^{il(\theta - \theta')} \\ K_{\sigma\sigma'}(\mathbf{r}, \mathbf{r}') &= \sum_l K_{\sigma\sigma'}^{(l)}(r, r') e^{il(\theta - \theta')} . \end{aligned} \quad (1.28)$$

By calculating the angular integral in Eq. (1.20) one can readily see that, indeed, only modes with $l = \pm 1$ couple to the external dipole fields $D_n^{(\pm)}$ and $D_m^{(\pm)}$.

Defining the correlation functions $\chi_{AB}^{(\pm)}(r, r'; \omega)$, with $A, B = n, m$, as

$$\begin{aligned} \chi_{nn}^{(\pm)} &\equiv \chi_{\uparrow\uparrow}^{(\pm)} + \chi_{\uparrow\downarrow}^{(\pm)} + \chi_{\downarrow\uparrow}^{(\pm)} + \chi_{\downarrow\downarrow}^{(\pm)} \\ \chi_{mm}^{(\pm)} &\equiv \chi_{\uparrow\uparrow}^{(\pm)} - \chi_{\uparrow\downarrow}^{(\pm)} - \chi_{\downarrow\uparrow}^{(\pm)} + \chi_{\downarrow\downarrow}^{(\pm)} \\ \chi_{nm}^{(\pm)} &\equiv \chi_{\uparrow\uparrow}^{(\pm)} - \chi_{\uparrow\downarrow}^{(\pm)} + \chi_{\downarrow\uparrow}^{(\pm)} - \chi_{\downarrow\downarrow}^{(\pm)} \\ \chi_{mn}^{(\pm)} &\equiv \chi_{\uparrow\uparrow}^{(\pm)} + \chi_{\uparrow\downarrow}^{(\pm)} - \chi_{\downarrow\uparrow}^{(\pm)} - \chi_{\downarrow\downarrow}^{(\pm)} , \end{aligned} \quad (1.29)$$

the so-called *response functions* to the dipole fields are given by

$$\begin{aligned} \alpha_{AB}(\omega) &= \pi^2 \int dr_1 dr_2 r_1^2 r_2^2 [\chi_{AB}^{(+)}(r_1, r_2; \omega) + \chi_{AB}^{(-)}(r_1, r_2; \omega)] \\ &\equiv \alpha_{AB}^{(+)}(\omega) + \alpha_{AB}^{(-)}(\omega) , \end{aligned} \quad (1.30)$$

and, despite the excitation energies ω being always positive, formally hold the equalities

$$\begin{aligned} \text{Re} [\alpha_{AB}^{(-)}(\omega)] &= \text{Re} [\alpha_{AB}^{(+)}(-\omega)] \\ \text{Im} [\alpha_{AB}^{(-)}(\omega)] &= -\text{Im} [\alpha_{AB}^{(+)}(-\omega)] . \end{aligned} \quad (1.31)$$

These relations are of great practical interest: in actual calculations they allow to determine both components (\pm) of the response function by using only e.g. the (+) one over a frequency range such as $(-\omega_{min}, \omega_{max})$.

The excitations induced by short-duration perturbations are usually described by the so-called *strength functions* $S_{AB}(\omega)$

$$S_{AB}(\omega) = S_{BA}(\omega) \equiv \sum_i \langle 0 | D_B | i \rangle \langle i | D_A | 0 \rangle \delta(\omega - \omega_{i0}) , \quad (1.32)$$

where $|0\rangle$ is the ground state and the sum –or integral in the case of continuum spectrum– runs over all the excited states $|i\rangle$ of the N -particle Hamiltonian

$$H = H_0 + \sum_{i < j=1}^N \frac{e^2}{\epsilon |\mathbf{r}_i - \mathbf{r}_j|} , \quad (1.33)$$

H_0 being the one-body part. The functions S_{AB} present peaks at the energies of the excited modes of the system ω_{i0} and have relative intensity proportional to the strength carried by each mode. Interestingly, they are related to the imaginary parts of the response functions by $S_{AB}(\omega) = \frac{1}{\pi} \text{Im}[\alpha_{AB}(\omega)]$. Besides, some general properties of the system, as well as a check of the accuracy of the calculations, can be extracted from the so-called f -sum rules, which are related to the strength functions and finally expressed uniquely in terms of gs quantities [Lip89]:

$$\begin{aligned} m_1^{(nn)} &= \int S_{nn}(\omega) \omega d\omega = \frac{1}{2} \langle 0 | [D_n, [H, D_n]] | 0 \rangle = \frac{N}{2} \\ m_1^{(mm)} &= \int S_{mm}(\omega) \omega d\omega = \frac{1}{2} \langle 0 | [D_m, [H, D_m]] | 0 \rangle = \frac{N}{2} \\ m_1^{(mn)} &= m_1^{(nm)} = \int S_{mn}(\omega) \omega d\omega + \int S_{nm}(\omega) \omega d\omega = \langle 0 | [D_m, [H, D_n]] | 0 \rangle = 2S_z \quad . \end{aligned} \quad (1.34)$$

Even though the operators $D_n = \sum_{i=1}^N x_i$ and $D_m = \sum_{i=1}^N x_i \sigma_z^i$ are expected to excite, respectively, dipole charge-density and spin-density collective modes, it is worth to point out that the above formalism leaves room for situations in which both operators induce excitations in both the charge and the spin channels.

At first glance, it might be thought that to obtain the response functions $\alpha_{AB}(\omega)$ one has to explicitly calculate the correlation functions $\chi_{\sigma\sigma'}(\mathbf{r}, \mathbf{r}'; \omega)$. This is a very demanding numerical task for nonhomogeneous systems, involving several large-dimension complex matrix inversions *for every value of* ω . A guide to how to proceed can be found e.g. in the Appendix B of Ref. [Bar94], which can be straightforwardly generalized to the Dyson Eq. (1.23). However, if $\chi_{\sigma\sigma'}(\mathbf{r}, \mathbf{r}'; \omega)$ is not needed for any other purpose, there is an alternative way to determine the response functions circumventing the resolution of the Dyson equation. We first introduce a noninteracting induced –e.g. by D_A – density in analogy with Eq. (1.20):

$$\delta n_\sigma^{(0,A)}(\mathbf{r}, \omega) = \sum_{\sigma'} \int d\mathbf{r}' \chi_{\sigma\sigma'}^{(0)}(\mathbf{r}, \mathbf{r}'; \omega) f_{\sigma'}^A(\mathbf{r}') . \quad (1.35)$$

Substituting the Dyson equation into Eq. (1.20) and introducing a self-explanatory matrix notation, Eq. (1.20) becomes

$$\begin{pmatrix} \delta n_\uparrow^A \\ \delta n_\downarrow^A \end{pmatrix} = \begin{pmatrix} \delta n_\uparrow^{(0,A)} \\ \delta n_\downarrow^{(0,A)} \end{pmatrix} + \begin{pmatrix} \chi_{\uparrow\uparrow}^{(0)} & 0 \\ 0 & \chi_{\downarrow\downarrow}^{(0)} \end{pmatrix} \otimes \begin{pmatrix} K_{\uparrow\uparrow} & K_{\uparrow\downarrow} \\ K_{\downarrow\uparrow} & K_{\downarrow\downarrow} \end{pmatrix} \otimes \begin{pmatrix} \delta n_\uparrow^A \\ \delta n_\downarrow^A \end{pmatrix} , \quad (1.36)$$

where the symbol ‘ \otimes ’ indicates an implicit spatial integration over the common \mathbf{r} -variable of the operands. The dynamic polarizability $\alpha_{AB}(\omega)$ is then readily written as

$$\alpha_{AB}(\omega) = - \begin{pmatrix} f_{\uparrow}^{A*} & f_{\downarrow}^{A*} \end{pmatrix} \otimes \begin{pmatrix} \delta n_{\uparrow}^B \\ \delta n_{\downarrow}^B \end{pmatrix}. \quad (1.37)$$

The problem of determining the dynamic polarizability is thus reduced to solving the set of $2N_p$ complex linear equations (1.36) instead of the far more complicated task of inverting $N_p \times N_p$ complex matrices, N_p being the number of points used to solve the KS equations, which is usually higher than the one employed in the response calculation.

The simplest physical situation to which the TDLSDA can be applied corresponds to its paramagnetic limit, i.e., when the gs spin magnetization $m(\mathbf{r})$ is identically zero. In this case one has $\chi_{\uparrow\uparrow}^{(0)} = \chi_{\downarrow\downarrow}^{(0)}$, and the function $\mathcal{M}(\mathbf{r})$ entering Eq. (1.25) is identically zero. Writing the induced densities as

$$\begin{aligned} \delta n^n &\equiv \delta n_{\uparrow}^n + \delta n_{\downarrow}^n = \chi_{nn} \otimes f \\ \delta m^m &\equiv \delta n_{\uparrow}^m - \delta n_{\downarrow}^m = \chi_{mm} \otimes f \\ \delta n^m &\equiv \delta n_{\uparrow}^m + \delta n_{\downarrow}^m = \chi_{nm} \otimes f \\ \delta m^n &\equiv \delta n_{\uparrow}^n - \delta n_{\downarrow}^n = \chi_{mn} \otimes f, \end{aligned} \quad (1.38)$$

where f denotes the r -dependence in Eq. (1.27), it is easy to check that in this limit χ_{mn} and χ_{nm} are identically zero, and that χ_{nn} and χ_{mm} obey the Dyson equations

$$\begin{aligned} \chi_{nn} &= \chi^{(0)} + \chi^{(0)} \otimes K_{nn} \otimes \chi_{nn} \\ \chi_{mm} &= \chi^{(0)} + \chi^{(0)} \otimes K_{mm} \otimes \chi_{mm}, \end{aligned} \quad (1.39)$$

in which the kernels are given by $K_{nn} = 1/\mathbf{r}_{12} + \mathcal{K} \delta(\mathbf{r}_{12})$ and $K_{mm} = \mathcal{I} \delta(\mathbf{r}_{12})$, where $\mathbf{r}_{12} \equiv \mathbf{r}_1 - \mathbf{r}_2$, and with the free-particle correlation function $\chi^{(0)} = \chi_{\uparrow\uparrow}^{(0)} + \chi_{\downarrow\downarrow}^{(0)}$ being the same in both channels since $\chi_{\uparrow\uparrow}^{(0)} = \chi_{\downarrow\downarrow}^{(0)}$. Thus, in the paramagnetic limit of the longitudinal spin response one is left with uncoupled charge and spin channels, in which the residual interaction consists of the direct Coulomb plus an exchange-correlation term in one case, and only of the exchange-correlation contribution in the other. When the system is spin-polarized $\chi_{\uparrow\uparrow}^{(0)} \neq \chi_{\downarrow\downarrow}^{(0)}$, $\mathcal{M}(\mathbf{r})$ is not identically zero and the two other independent correlation functions χ_{nm} and χ_{mn} produce the charge-density response to D_m , and the spin-density response to D_n , respectively. The general formalism has been applied to the description of longitudinal modes in quantum dots and rings [Bar00, Emp99, Ser99, Ser99b].

When considering a single quantum ring under in-plane electric and perpendicular magnetic fields, we have calculated the charge-density dipole response of the system using the *real-time adiabatic* TDLSDA approach described in detail in Ref. [Pi04], which we have restricted to a simpler two-dimensional QR. The analysis of the modes has been

done following the method proposed in Ref. [Pue99]. Essentially, the procedure consists in considering the interaction with the dipole field as a small perturbation of the gs $|0\rangle$ of the N -electron ring along a certain direction $\hat{\mathbf{e}}$, i.e., $|0'_{\hat{\mathbf{e}}}\rangle \equiv e^{i\lambda\hat{\mathbf{e}}\cdot\mathbf{r}}|0\rangle$ with $\lambda \ll 1$. Up to first order in λ , this can be written as $|0'_{\hat{\mathbf{e}}}\rangle \approx (1 + i\lambda\hat{\mathbf{e}}\cdot\mathbf{r})|0\rangle$. The ground and excited states of the Hamiltonian H constitute a basis $\{|0\rangle, |j\rangle\}$ ($j \neq 0$) in which the time-evolution of the perturbed state can be expanded: $|(t)'_{\hat{\mathbf{e}}}\rangle = e^{-iHt}|0'_{\hat{\mathbf{e}}}\rangle \approx e^{-i\omega_0 t}|0\rangle + \sum_{j=1}^{\infty} a_{j,\hat{\mathbf{e}}} e^{-i\omega_j t}|j\rangle$. One can easily check that the quantity $\langle(t)'_{\hat{\mathbf{e}}}|\hat{\mathbf{e}}\cdot\mathbf{r}|(t)'_{\hat{\mathbf{e}}}\rangle - \langle 0|\hat{\mathbf{e}}\cdot\mathbf{r}|0\rangle \equiv d_{\hat{\mathbf{e}}}(t)$ is related to the dipole strength function by the expression

$$S_{\hat{\mathbf{e}}}(\omega) = \frac{1}{\pi\lambda} \int_0^{\infty} d_{\hat{\mathbf{e}}}(t) \sin \omega t dt = \sum_{j=1}^{\infty} |\langle j|\hat{\mathbf{e}}\cdot\mathbf{r}|0\rangle|^2 \delta(\omega_{j0} - \omega) . \quad (1.40)$$

Finally, to obtain the excitation energies of the system we perform a least-squares minimization of the time-discretized function $\sum_t [d_{\hat{\mathbf{e}}}(t) - D_{\hat{\mathbf{e}}}(t)]^2$, with $D_{\hat{\mathbf{e}}}(t)$ given by

$$D_{\hat{\mathbf{e}}}(t) = \sum_{j=1}^M [A_{j,\hat{\mathbf{e}}} \cos \omega_{j0} t + B_{j,\hat{\mathbf{e}}} \sin \omega_{j0} t] , \quad (1.41)$$

and where the sum extends over M frequencies, its number being large enough to provide an accurate $d_{\hat{\mathbf{e}}}(t)$ from $D_{\hat{\mathbf{e}}}(t)$ and assuring the convergence of the calculation. The set $\{\omega_{j0}\}$ is obtained from Eqs. (1.40) and (1.41) as a discrete set of Dirac delta functions that in practice are fairly narrow Lorentzians because of the finite-time numerical integration in Eq. (1.40).

1.2 Single quantum rings under electric and magnetic fields

High-quality quantum rings have been fabricated on AlGaAs/GaAs heterostructures containing a quasi-two-dimensional electron gas, both by self-assembly techniques [Lor00] and by nanolithography using an atomic force microscope [Fuh01]. This has given rise to many experimental and theoretical results involving, e.g., spin pairing [Ihn03, Lus01], Zeeman splitting [Dun00, Fol01, Han03, Lin02], spin states due to in-plane or perpendicular magnetic fields [Cio02, Rok01], spin-blockade effects [Cio02, Hut03, Ono02] and, of particular interest because of its potential relevance to quantum information processing schemes, spin transitions driven by magnetic fields [Ash93, Bur99, Bur00, Cio01, Cio03, Hu00, Kou97, Sch95, Tar00] or –even in a more efficient way [Fuh01]– by gate voltages [Fuh03, Ihn05, Kyr02, Los98]. Indeed, the possibility to externally control and induce transitions between entangled spin-singlet $|\uparrow\downarrow\rangle - |\downarrow\uparrow\rangle$ and non-entangled spin-triplet $|\uparrow\uparrow\rangle$ states is of great importance in the realization of qubits since it provides an efficient way to manipulate the entanglement of these systems. Coulomb- and spin-blockade spectroscopy experiments proved the possibility to achieve such spin control in lateral [Cio03, Kyr02] and vertical [Bur00, Kou97] quantum dots, and similar conclusions have recently been obtained from experiments with many-electron quantum rings [Fuh03, Ihn05].

We have considered two- and three-dimensional single QRs with different confining potentials and addressed their ground state properties and also the density dipole response for the 2D ones, which have been considered to be submitted to both in-plane electric and perpendicular magnetic fields. Although no structure is strictly two-dimensional, it is commonly accepted that the confinement in the perpendicular direction is so strong that 2D models catch the basic physics of the processes under study while rendering the numerical effort much more affordable.

1.2.1 Ground state

At zero applied fields, for the ‘thick’ –i.e., axially symmetric 3D– quantum rings we have taken a parabolic confining potential in the xy -plane with a repulsive core around the origin, namely

$$V_{conf}(r) = V_0 \Theta(R_0 - r) + \frac{1}{2} m \omega_0^2 (r - R_0)^2 \Theta(r - R_0) \quad , \quad (1.42)$$

where $r = \sqrt{x^2 + y^2}$, with $\Theta(x) = 1$ if $x > 0$ and zero otherwise, together with a square well of width w and depth V_0 in the z -direction. The convenience of using a hard-wall confining potential to describe the effect of the inner core in QRs is endorsed by several works in the literature [Li05]. The strictly two-dimensional rings have firstly been described by the same in-plane confinement while taking the density along the z -direction to be a Dirac delta as done in Ref. [Emp01]. For the calculations we have taken $R_0 = w = 5$ nm, $V_0 = 350$ meV, and $\omega_0 = 15$ meV, a set of parameters that fairly represents the smallest rings synthesized in Ref. [Lee04], and the potential wells have been slightly rounded off as in Ref. [Anc03].

Experimentally, the shell structure of quantum rings is usually inferred from their addition spectrum [Lor00, Tar96], which is theoretically calculated from the expression

$$\Delta_2(N) \equiv E(N + 1) - 2E(N) + E(N - 1) \quad , \quad (1.43)$$

$E(N)$ being the total energy of the N -electron quantum ring. In Fig. 1.1 we show the addition energies for two- and three-dimensional QRs. It can be seen that both models sensibly yield the same results for this observable, a well-known fact for QDs [Pi01]. For the 3D rings the value of the calculated total-spin third component, $2S_z$, is also indicated in the figure. It must be pointed out that the $N = 3$ case of the 2D model is fully spin-polarized ($2S_z = 3$) whereas that of the thick ring it is not, due to the fact that the exchange-correlation energy is overestimated by strictly two-dimensional models [Ron99b]. However, fully polarized $N = 3$ QR configurations are not an artifact of the LSDA. As a matter of fact, they have also been found by exact diagonalization methods for some ring sizes and confining potential choices [Zhu05]. For the rest of configurations displayed in the figure both models yield the same spin assignments and coincide with those of Ref. [Emp01], although the height of the peaks in $\Delta_2(N)$ clearly depends to a large

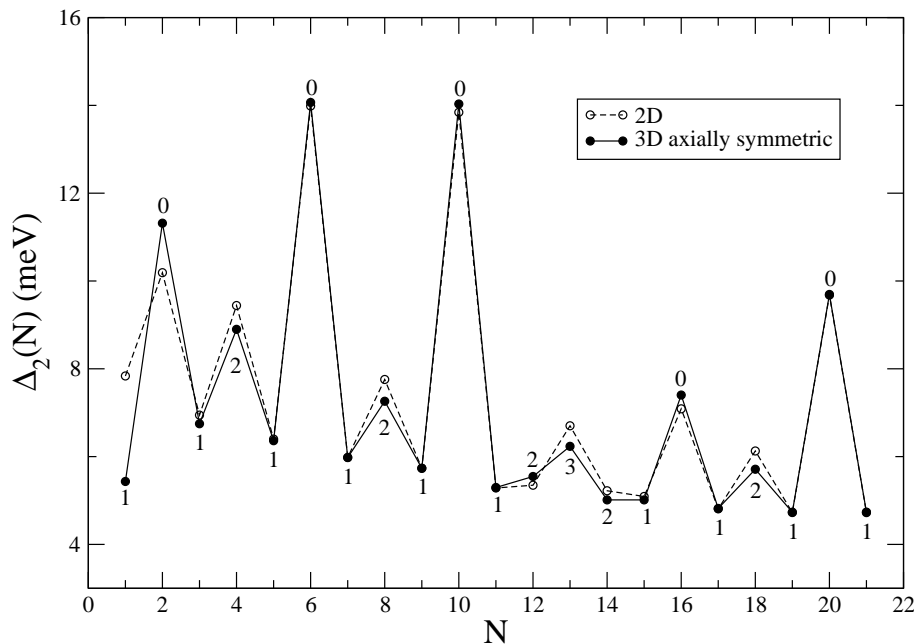


Figure 1.1: $\Delta_2(N)$ (meV) for a 3D (solid dots, solid lines) and a strictly 2D (open dots, dashed lines) quantum ring. The value of $2S_z$ obtained for the thick ring is indicated.

extent on the employed confining potential. The intensity of these peaks is proportional to the relative stability of the electronic shell closures in the ring, which for $N > 6$ are substantially different from those of QDs. For quantum rings, they are mainly governed by the fourfold degeneracy of the noninteracting sp levels with $|l| \neq 0$ and the twofold degeneracy of the noninteracting orbitals with $|l| = 0$ [Emp99]. This yields the marked shell closures at $N = 2, 6, 10, 20$ and 28 with $S_z = 0$, as well as the $S_z = 0$ gs found for $N = 24$. The $2S_z = 2$ configurations that regularly appear between the mentioned ones indicate that Hund's rule is fulfilled by single QRs.

The complex spin structure around $N = 13$, missing in other QR calculations employing a different confining potential [Lin01], can be understood by looking at the corresponding sp energies $\varepsilon_{nl\sigma}$, displayed in Fig. 1.2: for $N = 12$, the second ($0 \uparrow$) state is empty, yielding $2S_z = 2$; for $N = 13$ the exchange interaction favours the filling of this state yielding $2S_z = 3$; for $N = 14$, one of the ($\pm 3 \downarrow$) states is filled—they are degenerate—, yielding $2S_z = 2$ (actually, this many-electron configuration is nearly degenerate with the one in which the ($0 \downarrow$) state is filled instead, which also yields $2S_z = 2$). For $N = 16$, the ($0 \downarrow$) and ($\pm 3 \downarrow$) orbitals become populated, producing a fairly strong shell closure.

We have also considered a two-dimensional QR placed in both a magnetic field B perpendicular to the plane of motion of the electrons and an in-plane electric field \mathcal{E} applied along the x -direction, both fields being static and uniform. In this case, the confining potential modelling the ring has been chosen of the smooth form

$$V_{conf}(r) = V_0^{(1)} \frac{1}{1 + e^{(r-R_0+w)/\gamma_1}} + V_0^{(2)} \frac{e^{(r-R_0-w)/\gamma_2}}{1 + e^{(r-R_0-w)/\gamma_2}}. \quad (1.44)$$

We have performed the calculations taking $R_0 = 2.5$, $V_0^{(1)} = V_0^{(2)} = 5$, $\gamma_1 = \gamma_2 = 0.3$,

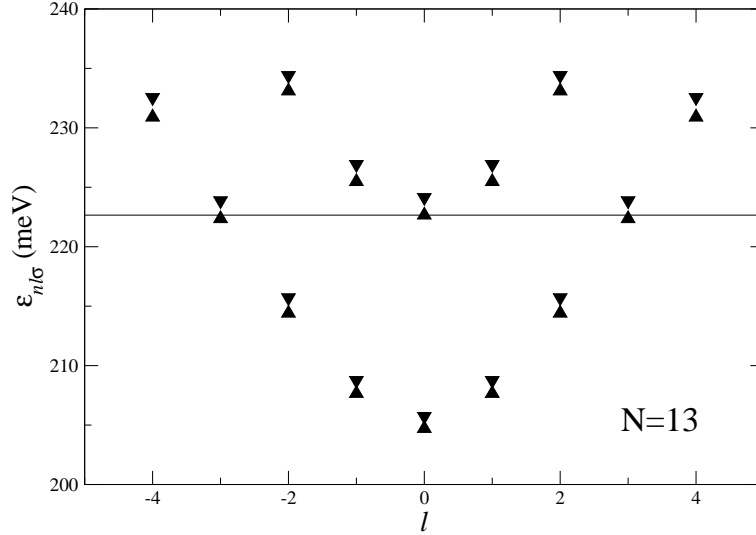


Figure 1.2: Sp energy levels (meV) as a function of l for a thick QR with $N = 13$. Upward (downward) triangles denote \uparrow (\downarrow) spin states, whereas the thin horizontal line represents the Fermi energy.

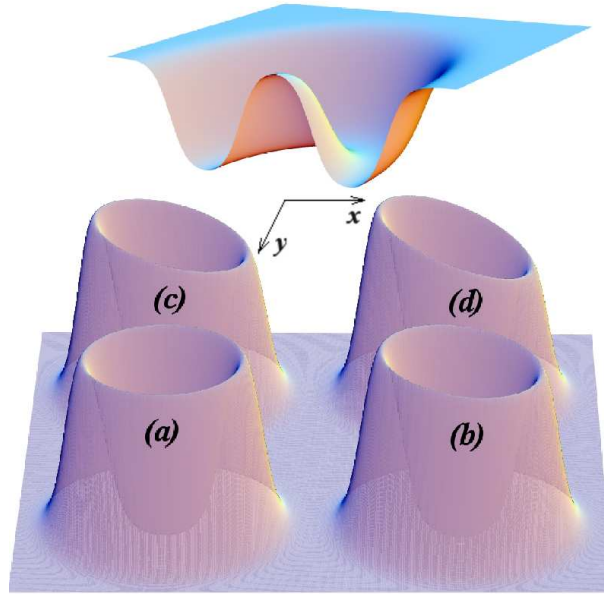


Figure 1.3: $V_{conf}(r)$ (upper) and electronic densities (lower) for the second 2D ring with $N = 10$ at $B = 0$ and $\mathcal{E} = 0, 1, 2,$ and 3 mV/nm (panels (a),(b),(c) and (d), respectively).

and $w = 1.25$ in effective atomic units, corresponding to a ring of average radius $R_0 \sim 25$ nm and width (distance between the inner and the outer edge) $2w \sim 25$ nm. A plot of $V_{conf}(r)$ is shown at the top of Fig. 1.3. In the lower panels of the same figure we plot the gs density of the $N = 10$ ring at $B = 0$ and $\mathcal{E} = 0 - 3$ mV/nm, showing how it is progressively deformed along the direction of the electric field as the intensity of the latter is increased.

In spite of this progressive deformation, all the electronic configurations we have found are always smooth, without charge-density nor spin-density waves in the azimuthal direc-

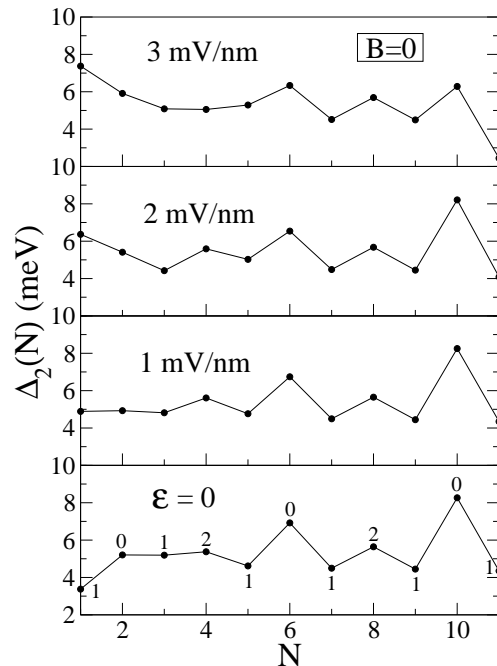


Figure 1.4: $\Delta_2(N)$ for $B = 0$ and $\mathcal{E} = 0, 1, 2$ and 3 mV/nm. The value of $2S_z$ is indicated in the $\mathcal{E} = 0$ panel.

tion. We attribute this to the external ring potential we have used, which is fairly wide in the radial direction. For more quasi-unidimensional rings and/or electronic systems more dilute than ours, the LSDA can yield solutions with azimuthally-modulated charge and spin densities [Rei02].

Figures 1.4-1.6 show the addition energies for quantum rings containing up to $N = 12$ electrons and for some selected values of the electric and the magnetic field. From the maxima in $\Delta_2(N)$ at $(\mathcal{E} = 0, B = 0)$ one can identify, as in the previous case, shell closures at $N = 6$ and 10 . As the electric field starts increasing, the deformation of the ring leads to a shell structure in which the sequence of magic numbers differs from the circular case. This can be seen, e.g., for $(\mathcal{E} = 1$ mV/nm, $B = 0)$, where a small peak arises at $N = 4$. Increasing further the electric field while switching on the magnetic field, the addition spectrum displays less structure. The peak at $N = 8$ is the sole exception, indicating a very strong shell closure for the chosen V_{conf} . It can also be seen that, for the displayed values of N , at $B = 0$ the spin is unaffected by electric fields up to $\mathcal{E} = 3$ mV/nm. $S_z(N)$ corresponding to odd- N rings turns out to be very robust even when a magnetic field is applied, and does not change for any of the values of \mathcal{E} and B that we have considered. The same occurs for the $N = 8$ case. However, at $B \neq 0$ interesting features appear for the rest of even electron numbers, namely $N = 2, 4, 6$ and 10 . Indeed, one can observe transitions between the $2S_z(N) = 0$ and $2S_z(N) = 2$ states driven by the electric field at fixed B . In the experiments [Fuh03, Ihn05], these gate-voltage-induced singlet-triplet transitions have been related to the competition between the Hartree and the exchange interactions, which favour, respectively, the formation of singlet and triplet spin states. The second spin differences, $S_2(N) \equiv S_z(N + 1) - 2S_z(N) + S_z(N - 1)$, have also been

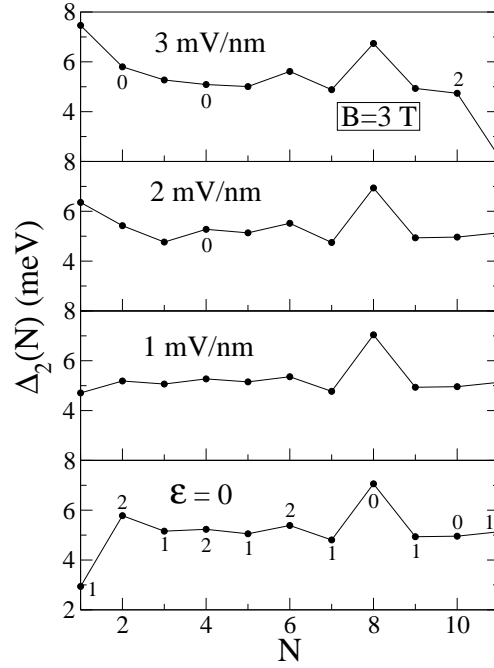


Figure 1.5: Same as Fig. 1.4 for $B = 3$ T. Upper panels display the value of $2S_z$ only when it differs from that of the $\mathcal{E} = 0$ case.

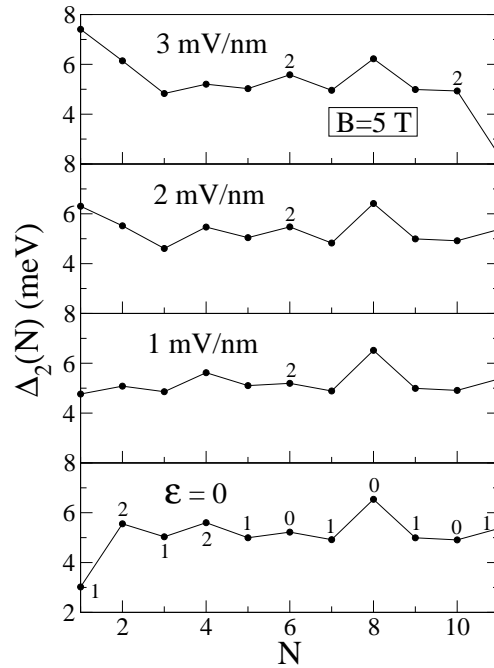


Figure 1.6: Same as Fig. 1.5 for $B = 5$ T.

measured from the slopes of the Coulomb-blockade peak spacings [Ihn05]. Our results at $\mathcal{E} = B = 0$ are shown in Fig. 1.7. It can be seen that $S_2(N)$ takes the three integer values $-1, 0$ and 1 , with one-unit jumps. The experimental N -sequence matches that of our calculation except in one case, in which it passes directly from 1 to -1 . We have found these two-unit jumps only when $B \neq 0$.

For the two-electron system we have solved the Schrödinger equation with the Hamil-

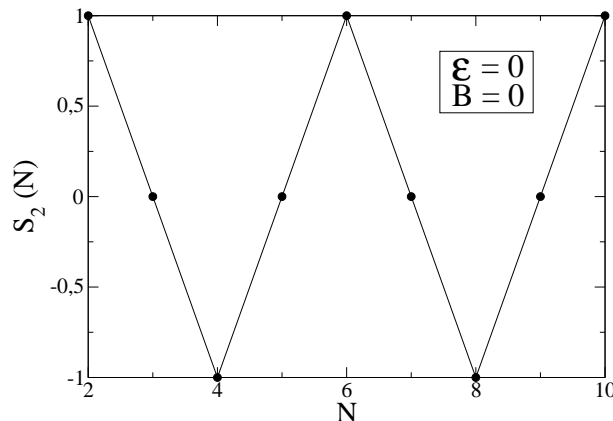
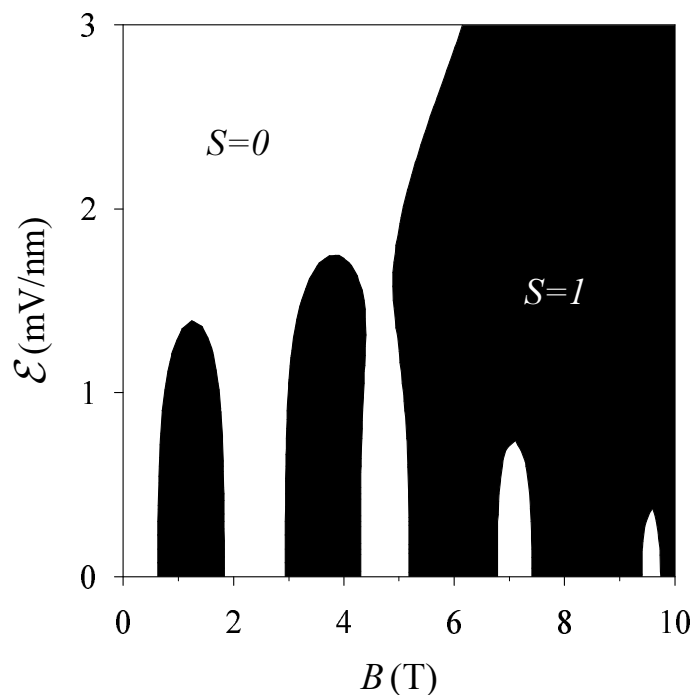
Figure 1.7: Second spin differences $S_2(N)$ for $B = 0$ T and $\mathcal{E} = 0$ mV/nm.

Figure 1.8: Spin-phase diagram for the two-electron ring in the electric-magnetic field plane. Black (white) indicates a triplet (singlet) ground state.

tonian Eq. (1.33) using the method of Ref. [Pue01], which consists in a uniform discretization of the xy -plane and in using finite differences to evaluate the Laplacian in the kinetic energy. Associating an index with the positions of the two electrons, $(\mathbf{r}_1, \mathbf{r}_2) \equiv I$, the resulting matrix equation reads $H_{IJ}\Psi_J = E\Psi_I$. The Hamiltonian matrix is very sparse since only the kinetic term yields non-diagonal contributions to H_{IJ} , the external (confinement and electric and magnetic) fields as well as the Coulomb interaction being local in $(\mathbf{r}_1, \mathbf{r}_2)$. The eigenvalue matrix equation can be solved by using iterative methods for boundary value problems [Koo90]. This way one determines E and Ψ_I by repeated action of H_{IJ} on an arbitrary initial guess for Ψ_I . For the singlet (triplet) state, the wave function $\Psi(\mathbf{r}_1, \mathbf{r}_2)$ is symmetric (antisymmetric) with respect to the exchange of \mathbf{r}_1 and \mathbf{r}_2 . This result implies that the triplet state vanishes for $I = (\mathbf{r}, \mathbf{r})$ whereas the singlet one

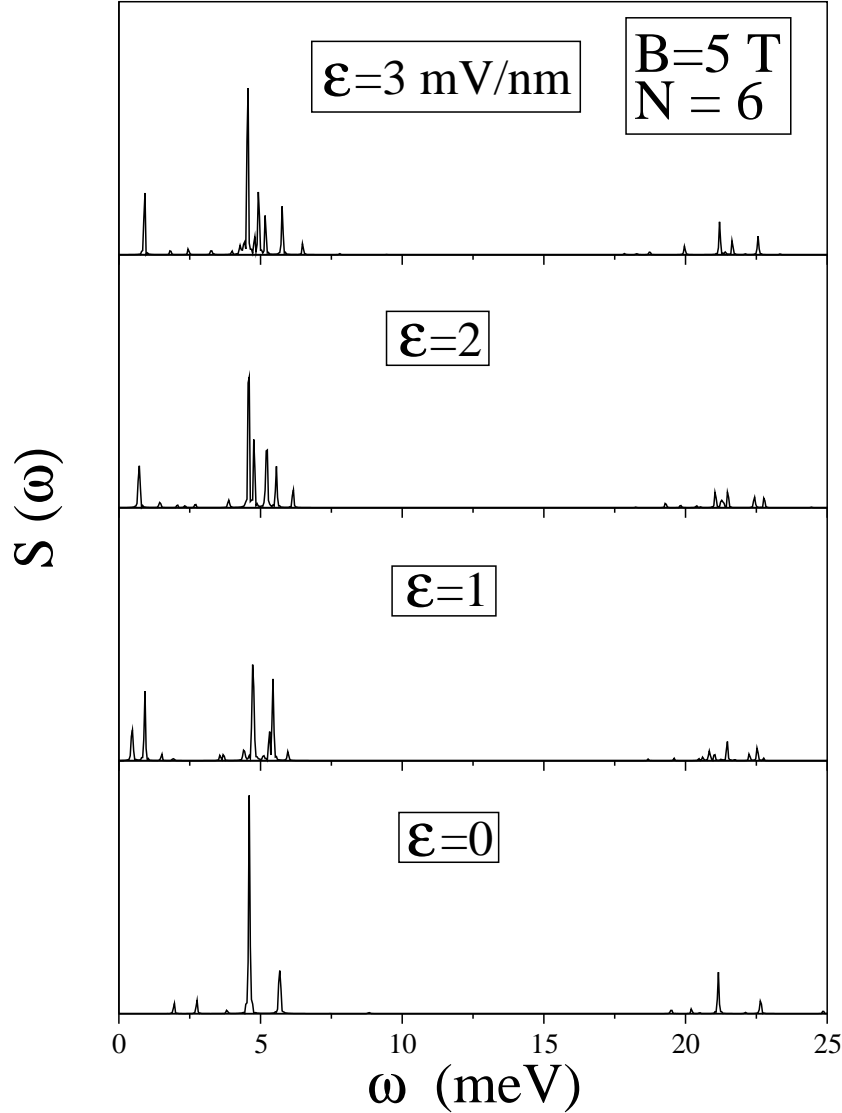


Figure 1.9: Charge-density dipole strength function $S(\omega)$ (arbitrary units) as a function of the excitation energy ω corresponding to $N = 6$, $B = 5$ T, and several values of the applied in-plane electric field \mathcal{E} .

has a cusp at these I 's that compensates the divergence in the Coulomb interaction. To avoid this singularity, we do not solve the Schrödinger equation at these specific values for I , but directly impose the null value of Ψ for the triplet state, and the cusp behavior for the singlet one. In order to extract the cusp condition, the smooth character of the chosen confining potential has allowed us to extrapolate the wave function at the closest I 's by using the analytically known behavior for parabolic confinements [Zhu96], and we have systematically checked the stability of the results by using finer grids in the calculations. A detailed exploration of the $\mathcal{E} - B$ plane is presented in Fig. 1.8 with the spin phase diagram corresponding to the ground state of the ring. The exact calculation shows the existence of spin islands at relatively low electric and magnetic fields that cause spin oscillations when, for a fixed \mathcal{E} , one increases B . LSDA calculations for the same $N = 2$ system (not shown here) also predict the possibility to induce singlet-triplet transitions

by varying the intensity of the electric field at fixed B . However, it must be pointed out that, as expected, the mean-field approach is unable to reproduce the details of the exact calculation for this low-density system, missing in particular the existence of spin islands and the associated spin oscillations.

1.2.2 Density dipole response

Fig. 1.9 shows the charge-density dipole strength function for the the $N = 6$ ring at $B = 5$ T and $\mathcal{E} = 0 - 3$ mV/nm as the sum of the contributions corresponding to the \hat{x} - and \hat{y} - directions, i.e. $S(\omega) \equiv S_{\hat{x}}(\omega) + S_{\hat{y}}(\omega)$. One can see that the more salient feature when an electric field is applied to the QR is its robustness. The $\mathcal{E} = 0$ reference spectrum (bottom panel) shows a two-peak structure around $\omega = 5$ meV due to the splitting caused by the magnetic field and some high-energy strength around $\omega = 20$ meV; the latter is discussed in detail in Ref. [Cli05] and constitutes a signature of the QR geometry that shows up in its far-infrared spectrum. The upper panels show that both structures are clearly visible as the electric field increases, with the only noticeable change being a higher fragmentation of the dipole strength, as well as the appearance of a soft mode around $\omega = 1$ meV that is absent when the system is axially symmetric (i.e. when $\mathcal{E} = 0$).

1.3 Vertically coupled quantum rings

One of the most appealing properties of quantum dots, widely regarded as ‘artificial atoms’, is their capability of forming molecules. Systems composed of two vertically coupled QDs have been investigated experimentally and theoretically at $B=0$ and also submitted to magnetic fields applied along different directions [Ama01, Asa98, Aus04, Bou00, Bur97, Hu96, Jac04, Jou00, Mar00, Mat02, May97, Pal95, Par00, Pi01, Pi05, Ron99, Sol96]. More recently, nanometer-sized complexes consisting of stacked layers of InGaAs/GaAs quantum rings have also been realized, and their optical and structural properties characterized by photoluminescence spectroscopy [Gra05].

Here we consider two vertically coupled 3D quantum rings separated by a variable distance d . The system as a whole can be viewed as a ‘diatomic’ *quantum ring molecule* (QRM) with total electron number N , and the variation of d allows one to study different ‘interatomic’ regimes. By analogy with real molecules, we consider *homonuclear* and *heteronuclear* QRMs, i.e., those constituted by identical or by different quantum rings. Indeed, for vertically coupled lithographic double QDs, it has been found unavoidable [Pi01] that a slight mismatch is unintentionally introduced in the course of their fabrication from materials with nominally identical constituent quantum wells, and the same is expected to happen for QRs.

The rings are described using the same in-plane confining potential as in the single QR case, Eq. (1.42), but now with two quantum wells separated by a distance d along the z -direction. For the heteronuclear QRM we consider two situations: one with a small

mismatch $\delta \ll V_0$ between the depth of the wells and another with the rings having slightly different radii.

1.3.1 Homonuclear quantum ring molecules

When considering two identical rings, we have calculated their gs structure for $d = 2, 4$ and 6 nm, and up to $N = 32$ electrons. It is known [Pi01] that for a given electron number, the evolution of the gs ('phase') of a QRM as a function of d may be thought of as a dissociation process. Within this scheme, each orbital is represented by four quantum labels: S_z , l , the parity, and the value of reflection symmetry about the $z = 0$ plane. Analogously as in natural molecules, symmetric/antisymmetric states $|S\rangle/|AS\rangle$ with respect to this plane are called bonding/antibonding states.

The energy difference between bonding and antibonding pairs of sp orbitals, Δ_{SAS} , can be properly estimated [Pi01] from the difference in energy of the antisymmetric and symmetric states of a single-electron QRM, namely $\Delta_{SAS} \sim E(^2\Sigma_u^-) - E(^2\Sigma_g^+)$ –see below for the notation–, and we have found it to vary from 24.9 meV at $d = 2$ nm (strong coupling), to 1.49 meV at $d = 6$ nm (weak coupling). In this range of inter-ring distances, Δ_{SAS} can be fitted as $\Delta_{SAS} = \Delta_0 e^{-d/d_0}$, with $\Delta_0 = 82$ meV and $d_0 = 1.68$ nm. The relative value of $\hbar\omega_0$ and Δ_{SAS} crucially determines the structure of the molecular phases along the dissociation path.

Figure 1.10 shows the evolution with d of the ground-state energy and molecular phase of a QRM made of $N = 3 - 7$ electrons. Each configuration is labeled using an adapted version of the ordinary spectroscopy notation [Ron99], namely $^{2S+1}L_{g,u}^\pm$, where S and L are the total $|S_z|$ and $|L_z|$, respectively. The superscript $+$ ($-$) refers to even (odd) states under reflection with respect to the $z = 0$ plane, and the subscript g (u) to positive (negative) parity states. To label the molecular sp states we have employed the standard convention of Molecular Physics, using $\sigma, \pi, \delta, \dots$ for $l = 0, \pm 1, \pm 2, \dots$, whereas upper case Greek letters refer to the total $|L_z|$. The figure shows that the energy of the molecular phases increases with d . This is due to the increasing energy of the sp bonding states as the rings become more separate [Pi01a], which dominates over the decrease in the Coulomb energy. At larger inter-ring distances (not shown here), the constituent QRs are so apart that eventually the weakness of the e-e interaction dominates and the tendency is reversed. The phase sequences are the same as for double quantum dots [Pi01] although the transition inter-ring distances are different as they obviously depend on the shape and strength of the confining potential. As happens for double quantum dots, we have found that the first phase transition of a few-electron QRM is always due to the replacement of an occupied bonding sp state by an empty antibonding one.

In Fig. 1.11 we show the addition spectra for homonuclear QRMs with up to $N = 31$ for the three selected inter-ring distances. Also shown is the spectrum of a single QR for comparison. At small distances ($d = 2$ nm, $\Delta_{SAS} \gg \hbar\omega_0$) the spectra for the QRM and for the single ring are rather similar, especially for few-electron systems, with minor changes

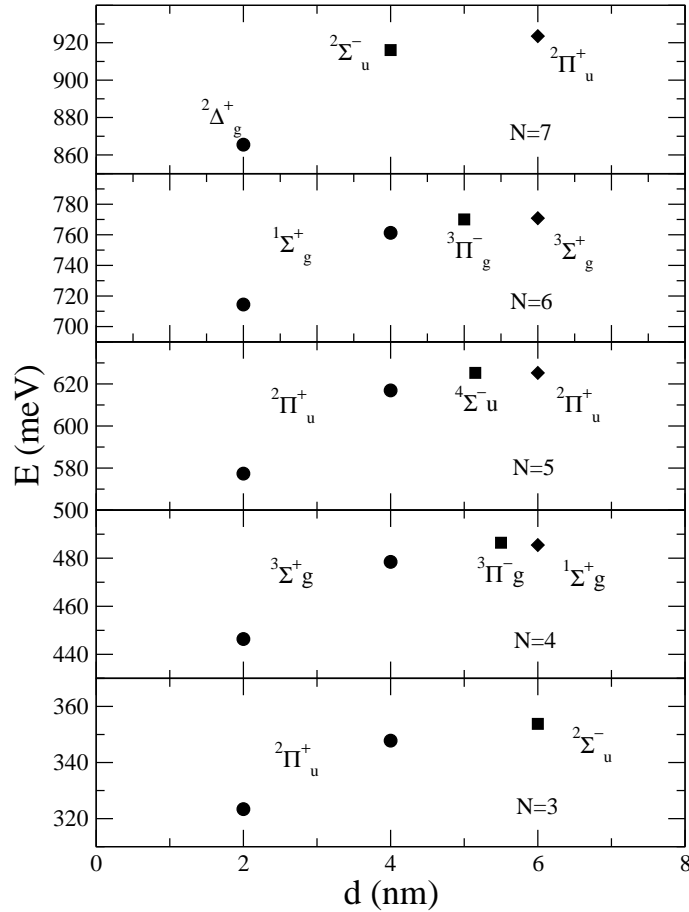


Figure 1.10: Energy (meV) and gs ‘molecular’ phases of the homonuclear QRM as a function of d for $N = 3 - 7$. Different phases are represented by different symbols.

arising in the $N \sim 12$ and ~ 24 regions that are commented below. It is thus clear that in this regime the two QRs are electrostatically and quantum-mechanically coupled and behave as a single system. At intermediate distances the spectrum pattern becomes more complex, but at larger distances (e.g. $d = 6$ nm), when the QRM molecule is about to dissociate, the physical picture that emerges is rather simple and can be interpreted using intuitive –yet approximate– arguments: At large distances ($\Delta_{SAS} \ll \hbar\omega_0$), the QRs are coupled only electrostatically, with most of the ($|S\rangle, |AS\rangle$) pairs of states being quasidegenerate. Electron localization [Wie03] in each constituent QR can be achieved by combining these states as $(|S\rangle \pm |AS\rangle)/\sqrt{2}$ and, as a consequence, the strong $S_z = 0$ peaks found at $N = 12$ and 20 are readily interpreted from the peaks appearing in the single-ring spectrum at $N = 6$ and 10 ; the process can be viewed as the symmetric dissociation of the original QRM leading to very robust closed-shell single-QR configurations. This is also the origin of the peaks with $S_z = 0$ at $N = 2$ and 4 : in the former case, the situation corresponds to one single electron being hosted in each constituent QR coupled into a singlet state, whereas in the latter case the QRM configuration can be interpreted by considering two QRs, each one occupied by two electrons filling the $1s$ shell. At this distance other dissociations display a more complicated pattern, such as the $16 \rightarrow 8 + 8$

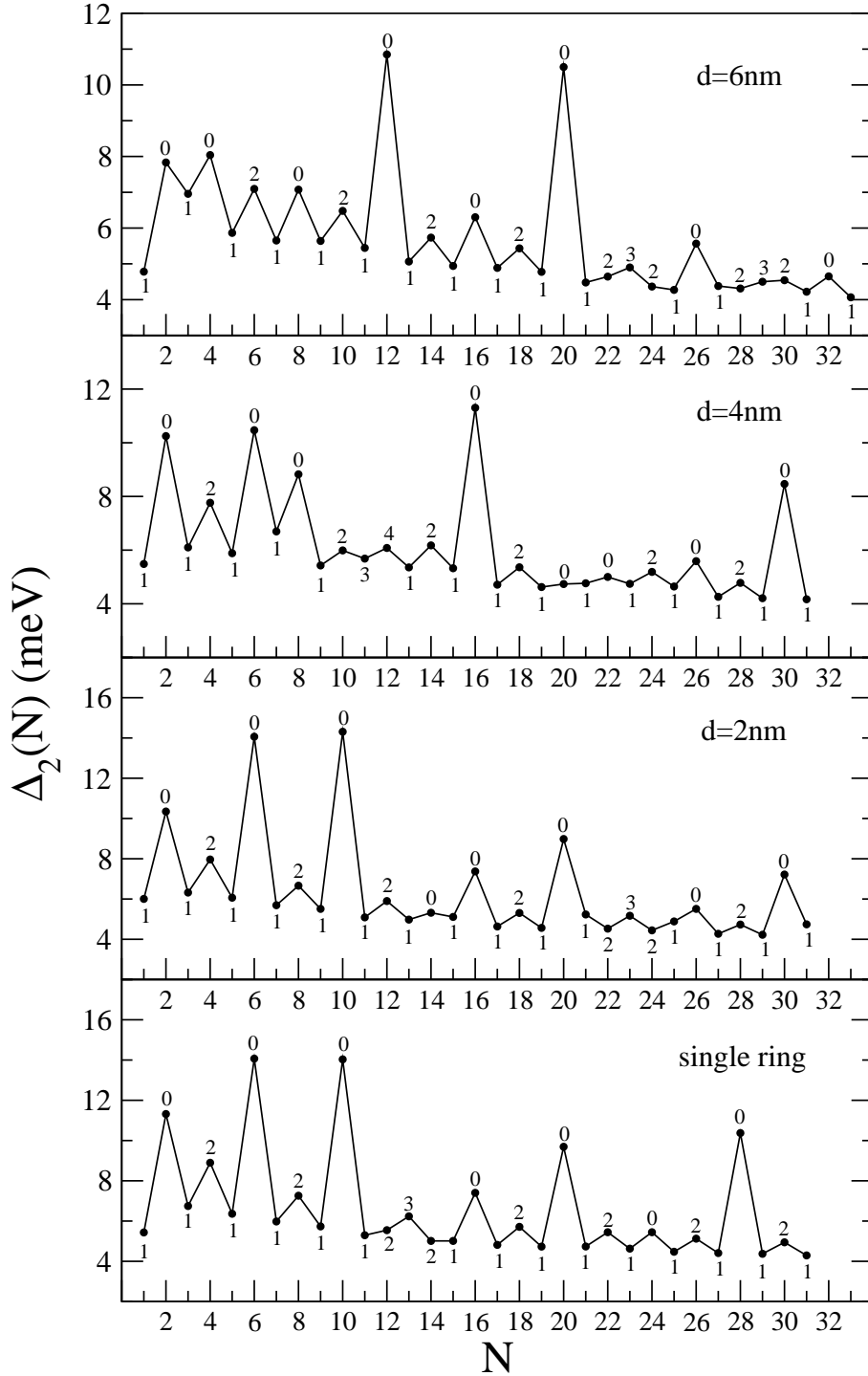


Figure 1.11: $\Delta_2(N)$ for homonuclear QRM with $d = 2, 4,$ and 6 nm, and for the single QR. The energies have been offset for clarity and the value of $2S_z$ is indicated.

or $8 \rightarrow 4 + 4$ ones, whose final products are QRs that fulfill Hund's rule whereas the actual QRM has $S_z = 0$. These could be interpreted as rather entangled QRMs, 'harder' to dissociate, for which an inter-ring distance of $d = 6$ nm is not large enough to allow for electron localization. The fact is that not only quasidegeneracy of occupied $|S\rangle$ and $|AS\rangle$ states at a given d plays a role in this intuitive analysis, but also whether their number is equal or not, so that they eventually may be combined to favour the localization. An

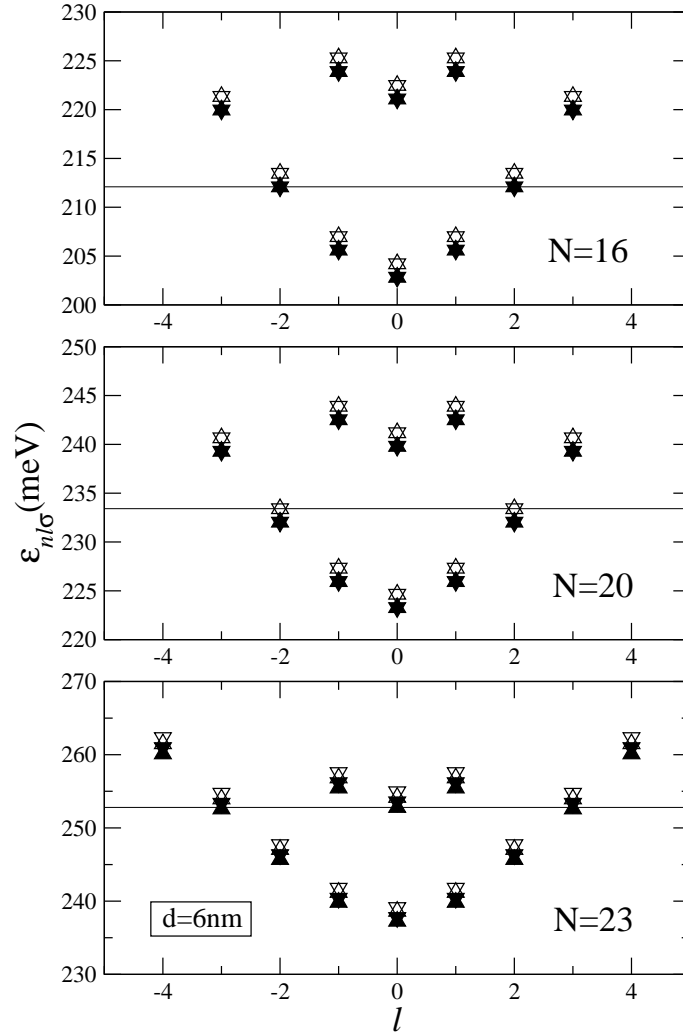


Figure 1.12: Sp energy levels (meV) as a function of l for an homonuclear QRM in the weak coupling regime. Open (solid) triangles correspond to antibonding (bonding) states.

example of these two different situations is illustrated in Fig. 1.12, where we show the sp states of the $N = 16, 20$ and 23 QRMs at $d = 6$ nm. In the first and third cases, the filled bonding states near the Fermi level have not filled antibonding partner to combine with and are delocalized over the whole volume of the QRM: as in natural molecules, some orbitals contribute to the molecular bonding, whereas some others do not.

1.3.2 Heteronuclear quantum ring molecules

We have considered two possible values for the mismatch between the quantum wells, namely $2\delta = 2$ and 4 meV (recall that $V_0 = 350$ meV). It can be easily checked that in the weak coupling limit ($\hbar\omega_0 \gg \Delta_{SAS}$), 2δ is approximately equal to the energy difference between bonding and antibonding sp states, which would be almost degenerate if $\delta = 0$. Therefore, this mismatch is expected to have important effects on the electron localization as the inter-ring coupling becomes weaker.

Fig. 1.13 displays the addition energies for heteronuclear QRMs as a function of d and

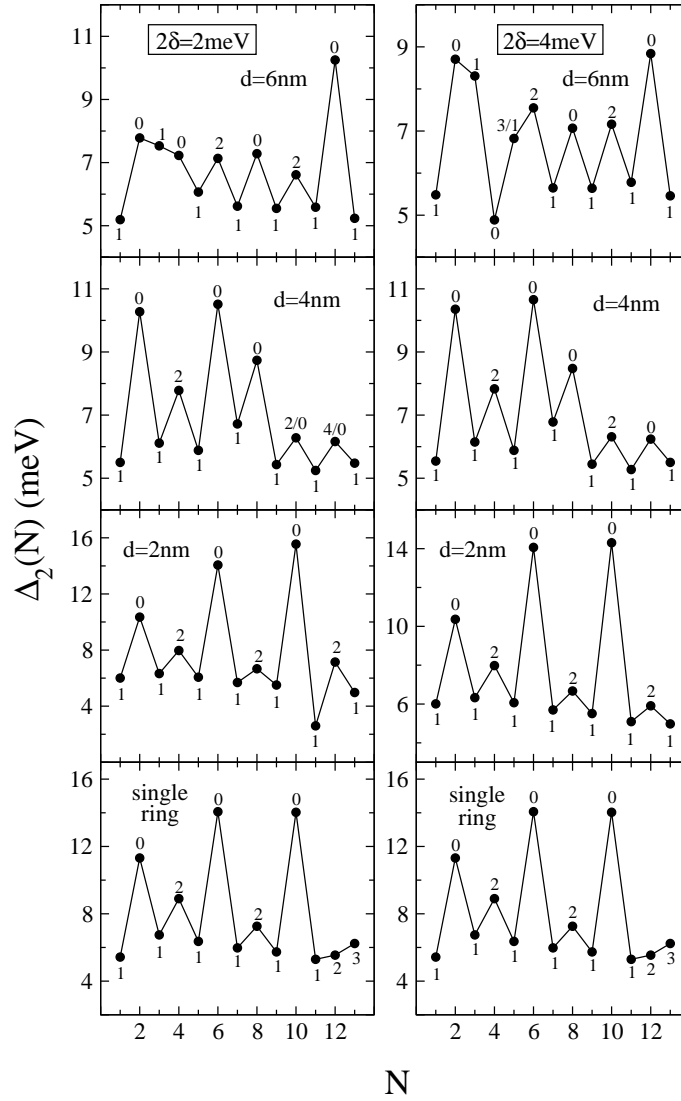


Figure 1.13: Same as Fig. 1.11 for heteronuclear QRMs with $2\delta = 2 \text{ meV}$ (left panels) and $2\delta = 4 \text{ meV}$ (right panels). Note that in some cases two different values of S_z have been assigned to the same peak, meaning that the corresponding configurations are nearly degenerate.

the electron number, as well as for the single quantum ring. It can be seen that in the strong coupling limit the effect of the mismatch on the addition energies is negligible, as expected [Pi01]. In this case, as we show below, the electrons are completely delocalized in the whole volume of the QRM, and the introduced mismatch is unable to localize them in either of the constituent rings. The situation however changes in the weak coupling limit. Indeed, for few-electron QRMs, which represent the more interesting physical situation, we have shown in the previous section that the fingerprint of the homonuclear character is the appearance of peaks in $\Delta_2(N)$ corresponding to $N = 2$ and 4, as well as their spin assignment $S_z = 0$. It can be seen from Fig. 1.13 that in the heteronuclear case, whereas in the intermediate regime ($d = 4 \text{ nm}$) the $N = 4$ peak is still present –although with $2S_z = 2-$, at larger inter-ring distances it eventually disappears, yielding an addition spectrum that, as we shall see, is characteristic of these kinds of configurations.

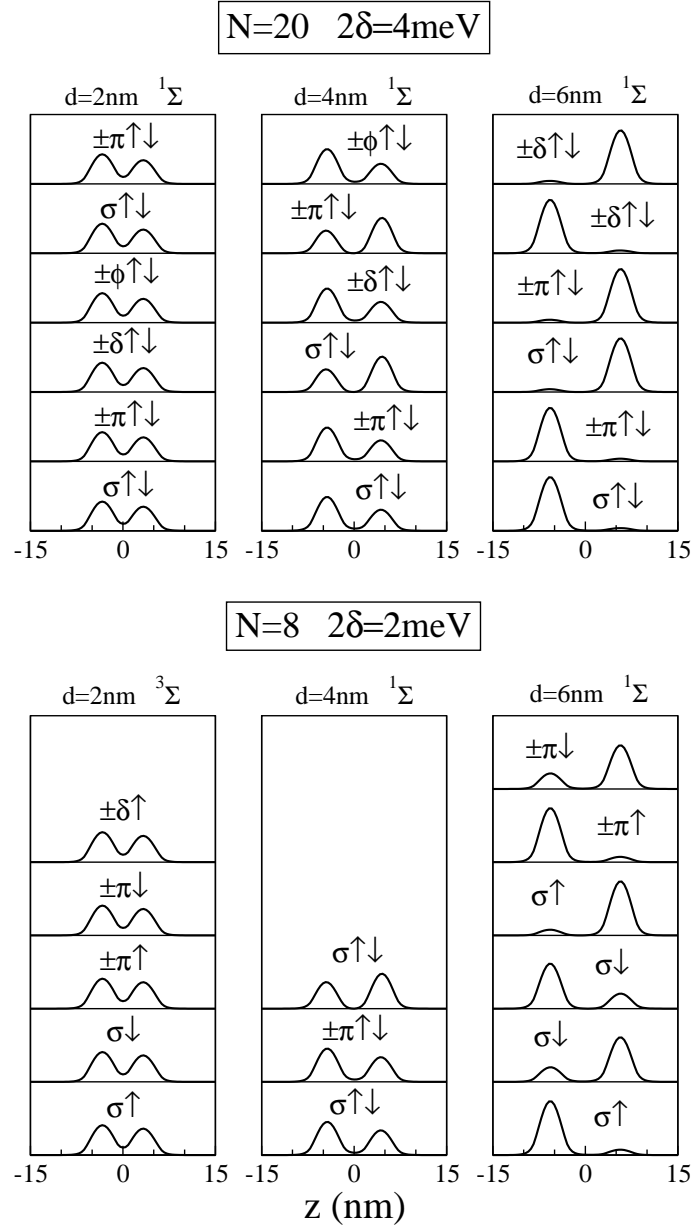


Figure 1.14: $\mathcal{P}(z)$ (arbitrary units) as a function of z for heteronuclear QRMs. The corresponding molecular configuration is also indicated.

It is useful to display the dissociation of the QRM representing the d -evolution of the sp molecular wave functions by introducing the z -probability distribution function [Pi01]

$$\mathcal{P}(z) = 2\pi \int dr r [u(r, z)]^2 . \quad (1.45)$$

Examples of these probability functions can be seen in Fig. 1.14, where we show $\mathcal{P}(z)$ for $(N = 20, 2\delta = 4 \text{ meV})$, and $(N = 8, 2\delta = 2 \text{ meV})$ (deeper well always in the $z < 0$ region), each case for the three chosen distances. The probability functions are plotted ordered from bottom to top according to increasing sp energies. For $N = 20$, the final configurations are the closed-shell ($N = 10, 2S_z = 0$) QRs, whereas for $N = 8$, the ($N = 4, 2S_z = 2$) configurations induced by Hund's rule emerge.

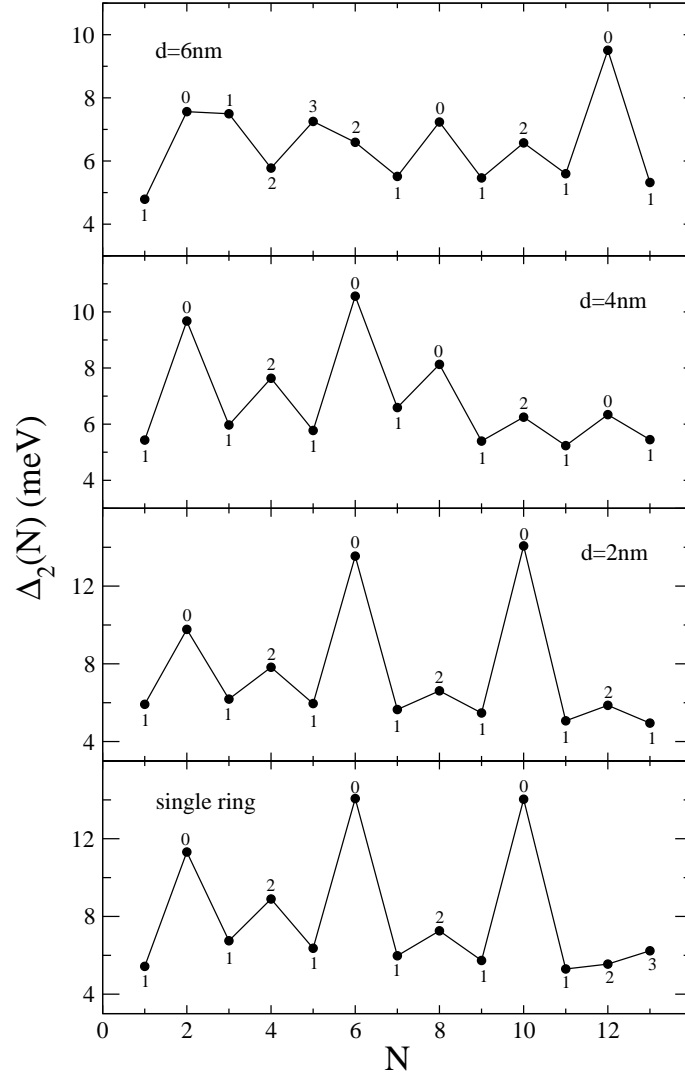


Figure 1.15: $\Delta_2(N)$ for heteronuclear QRM made of QRs with different core radii, namely $R_0 = 5$ and $R_0 = 6$ nm.

Finally, we discuss the case of two axially-symmetric vertically coupled QRs with different radii and study the effect this asymmetry has on the addition spectrum (we have discarded a possible disalignment of the QR symmetry axes, as addressing this situation would require a much more demanding full 3D calculation [Pi04]). To this end, we have taken for one ring $R_0 = 6$ nm while for the other one we have kept the same value as before, namely $R_0 = 5$ nm (the mismatch δ between both wells is set to zero in this case). Vertically coupled QDs of different radii have been described in Ref. [Bur97] to address the sensitivity of the exchange coupling to an applied in-plane electric field.

We show in Fig. 1.15 the corresponding addition energy spectra for up to $N = 14$ electrons and inter-ring distances $d = 2, 4,$ and 6 nm. It can be seen that in the strong and intermediate coupling regimes they are fairly similar to the previous heteronuclear case (and to the homonuclear case as well), indicating a fairly robust structure for the QRM in these limits. As before, the heteronuclear character clearly shows up in the weak coupling limit, with a peak structure and S_z assignments remarkably similar to those

discussed in the previous situation with $\delta \neq 0$ and that seems to be a clean fingerprint of such asymmetric systems.

This quantitative study allows one to associate realistic values to the physical magnitudes and to the effects that characterize vertically coupled quantum rings, like the shell closures as a function of the inter-ring distance, which as said above can be disclosed by the calculated addition spectra, as well as the ground-state spin assignments. Although we still lack of experimental results to compare ours with, we believe that the presented theoretical predictions can be helpful in the analysis of future experiments on these kinds of systems.

1.4 Concentric quantum rings

Progress in nanofabrication technology has recently allowed to achieve the formation of ‘artificial diatomic molecules’ made of self-assembled, strain-free, concentrically-coupled GaAs/AlGaAs double quantum rings [Man05]. This has sparked experimental and theoretical studies on the ground state and optical properties of these systems. In particular, photoluminescence spectra of concentric double quantum rings (CDQRs) have been measured and interpreted as evidence of exciton localization in either the inner or the outer ring [Kur05, Man05]; the single-electron [Fus04, Pla05] and electron-hole [Pla05] energy levels considering the application of a magnetic field perpendicular to the plane of symmetry of the rings were studied theoretically showing that, even for small inter-ring distances, self-assembled CDQRs can be approximately described as a sum of two decoupled rings. Also, the magnetic response of one- to three-electron energy levels in this type of nanostructures has been investigated [Sza05].

The singular geometry of concentric quantum rings has been found to introduce characteristic features in the addition spectrum compared to that of other coupled nanoscopic quantum structures. Indeed, unlike lateral quantum dots, CDQRs couple concentrically and thus preserve their cylindrical symmetry. Moreover, these molecules are heteronuclear, with the volume of the outer ring usually exceeding that of the inner ring [Man05], making the maximum charge density of bonding and antibonding states localize in different rings and thus showing distinct energy spacing between consecutive azimuthal levels [Pla05]. In these systems the electron localization in either ring follows from an intricate interplay between spatial confinement, centrifugal forces (favouring the occupation of the inner ring) and Coulomb interaction (which tends to favour the occupation of the more voluminous ring, as long as it is not heavily charged), with each of these factors prevailing in a given range of inter-ring distances. Interestingly, this interplay may lead to spin-dipolar configurations, where the inner-ring charge density is strongly spin-polarized whereas the outer-ring one it is not.

Analogously as done for single QRs, we have considered two- and three-dimensional concentric double quantum rings, addressing their ground state and also the dipole response in the former case. The three-dimensional system has been taken to have variable

inter-ring distance by changing the radius of the outer ring whereas for the 2D one we have considered the application of a variable perpendicular magnetic field while keeping the size of the rings fixed.

1.4.1 Variable inter-ring distance

The 3D concentric double quantum rings are described here by a confining potential in the (r, z) plane consisting of two superimposed Gaussian curves with total height given by

$$H(r) = h_{in} \exp \left[- \left(\frac{r - R_{in}}{\sigma_{in}} \right)^2 \right] + h_{out} \exp \left[- \left(\frac{r - R_{out}}{\sigma_{out}} \right)^2 \right], \quad (1.46)$$

where R_{in} and h_{in} (R_{out} and h_{out}) correspond, respectively, to the radius and maximum height of the inner (outer) ring, and $\sigma_{in/out}$ give the corresponding half-widths. The confinement is then defined by

$$V_{conf}(r, z) = \left\{ \begin{array}{ll} 0 & \text{if } 0 \leq z \leq H(r) \\ V_c & \text{otherwise,} \end{array} \right\}, \quad (1.47)$$

with V_c standing for the heterostructure band-offset –misalignment between the bottom of the AlGaAs and the GaAs conduction bands. It is worth stressing that this confinement allows one to fit accurately the DQR profile observed by atomic force microscopy in Ref. [Man05]. To this end, we have fixed the inner-ring radius at $R_{in} = 22.5$ nm while the outer one is varied from $R_{out} = 22.5$ to 50 nm. The inner- (outer-)ring half-width is 12.5 (30) nm, and both have height $h_{in/out} = 4$ nm. For GaAs/Al_{0.3}Ga_{0.7}As systems, the band-offset is $V_c = 262$ meV. Eq. (1.47) also renders a detailed description of the vertical confinement, which is essential because of the sensitivity of the energy spectrum to the depth of the valley separating the inner and outer ring [Pla05]. Moreover, within this model the evolution from a single to a double quantum ring as R_{out} increases implies a transfer of volume from the inner to the outer ring that realistically mimics the As-flux-controlled self-assembly [Man05]. On the other hand, the three-dimensional Hamiltonian –though axially symmetric– is important not to overestimate the role of the Coulomb interaction [Ron98]. Note also that, since the height of the two Gaussian curves adds up when they overlap, the area of the DQR cross-section is constant.

One expects that for small inter-ring separations a large number of electrons can be placed in the inner ring because the electronic repulsion hardly compensates for the stronger vertical confinement in the outer ring and the centrifugal stabilization. On the contrary, with increasing separation the relative volume of the outer ring grows and at some point the electrons should move into it rather swiftly. The situation however becomes less intuitive at intermediate distances, where the KS orbitals localized in the inner and outer ring are expected to be close in energy and the Coulomb interaction to become critical in the determination of the shell filling and the electron localization. Thus, we have

found it convenient to disentangle this factor investigating independent-particle effects in the first place.

Fig. 1.16 shows the single-electron orbital energy levels ε_{nl} for CDQRs with different R_{out} . Only the two lowest eigenvalues ($n = 0$ and $n = 1$) for each l are depicted because $n = 2$ states are much higher in energy. In all cases, $n = 0$ and $n = 1$ levels clearly show different spacing between consecutive values of l . This reflects the different mean radii of their charge densities, which allow one to distinguish the states as localizing in the inner or in the outer ring (represented by solid and open boxes, respectively). Such classification is justified by the above-mentioned fact that the single-electron orbitals of self-assembled CDQRs can be approximately described as the sum of states of both rings, considering each one as an isolated entity [Fus04, Pla05]. One can see that for $R_{out} = 45$ nm $n = 0$ states localize in the inner ring, whereas those with $n = 1$ localize in the outer one. As R_{out} increases the relative volume of the inner ring is reduced, and therefore the states localizing in it are destabilized. Consequently, with increasing R_{out} the lowest-lying levels of the inner ring first become quasidegenerate with those of the outer one and finally become more excited (i.e. $n = 0$ states localize in the outer ring).

The radial charge density corresponding to some N -electron ground states of Fig. 1.16 are shown in Fig. 1.17, resulting from an independent-particle filling of the energy levels. The insets show the corresponding confinement profile for each value of R_{out} . It is noted that for $R_{out} = 45$ nm, even though the outer ring is clearly formed, almost no leaking of density from the inner one to it is observed. This means that all $n = 0$ orbitals are mostly localized within the inner ring regardless of their angular momentum. A similar situation occurs for $R_{out} = 50$ nm, but in this case the $n = 0$ orbitals are mostly localized in the outer ring. Only in the intermediate region, where some $n = 1$ states are close in energy to $n = 0$ ones with $l > 0$, simultaneous charging of both rings appears. These results indicate that the tunneling between both rings is strongly suppressed by the Gaussian-like profile of the confinement cross-section [Man05]: since the vertical confinement is much stronger than the lateral one, small differences in the height of the inner and outer ring have a dramatic effect on the corresponding energy levels. For $R_{out} = 45$ nm the outer ring is clearly defined, but its height is lower than that of the inner ring (see insets of Fig. 1.17), so its energy levels are relatively very excited. On the contrary, for $R_{out} = 50$, when the height of both rings is already comparable, the outer ring has become much wider than the inner one and therefore its energy levels are more stable. It is worth stressing again that these effects cannot be found if the employed confining potential does not properly consider the variations of the vertical confinement for each radial position. Indeed, we have carried out calculations taking V_{conf} to be similar to that of previous works for laterally coupled quantum dots [Wen00] and large CDQRs [Sza05], namely a quantum well in the growth direction and two overlapping parabolae in the radial direction. The results are then qualitatively different: for all inter-ring distances the $(n = 0, l = 0)$ ($(n = 1, l = 0)$) states localize mainly in the inner (outer) ring, whereas the $|l| > 0$ states do so in the opposite one. This would suggest that the centrifugal potential and the inter-ring spatial

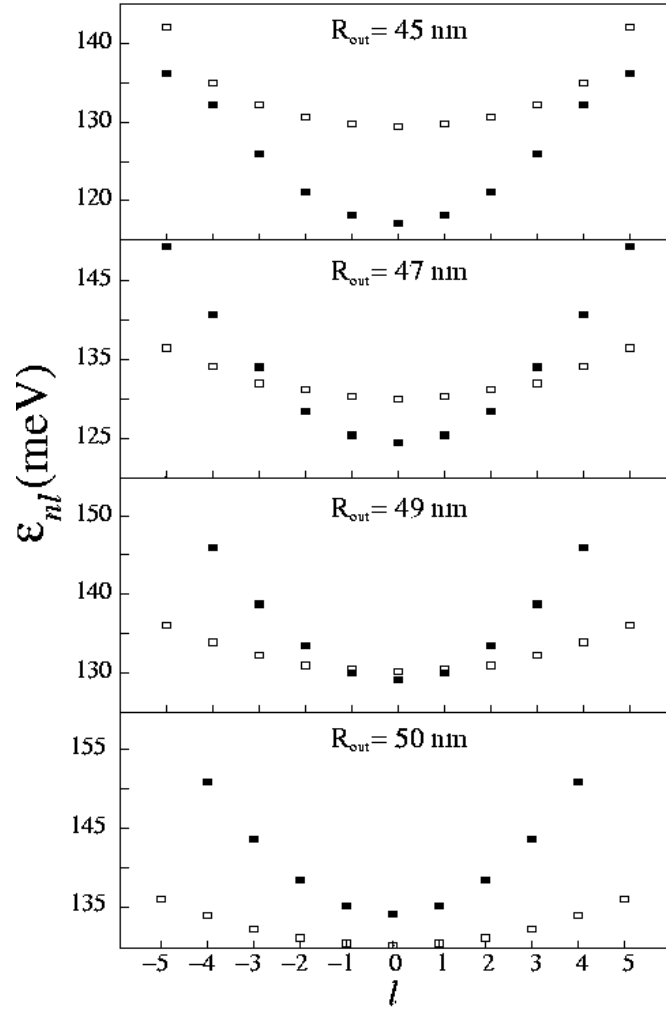


Figure 1.16: Lowest-lying orbital energy levels vs. angular momentum in CDQRs with $R_{in} = 22.5$ nm and changing R_{out} . Solid (open) boxes correspond to states localized in the inner (outer) ring.

confinement have comparable contributions in the Hamiltonian [Sza05]; it does not seem to be the case for self-assembled CDQRs [Fus04, Pla05].

In Fig. 1.18 we show the independent-particle addition energy spectra. For $R_{out} = 42.5$ nm $\Delta_2(N)$ are essentially those of a single QR, with peaks at the closed-shell configurations $N = 2, 6, 10$ and 14 . Obviously, no peaks are now observed at half-shell-filling values of N since we are neglecting the Coulomb interaction. It can be seen that the height of consecutive maxima increases with N because the larger l is, the larger the energy spacing $\Delta E(n, l \pm 1)$ becomes (see Fig. 1.16). The first irregularity is observed at $R_{out} = 45$: the peak at $N = 14$ is lower than the one at $N = 10$. This happens because once the $(n = 0, l = 3)$ shell is closed by the 14th electron –i.e. that whose filling gives rise to a CDQR with $N = 14^-$, the next energy level is not $(n = 0, l = 4)$ but $(n = 1, l = 0)$, which mostly localizes the wave function in the already voluminous external ring. As R_{out} keeps increasing, the lowest orbitals with $n = 1$ start catching up with lower- l states with $n = 0$. This is manifested in the spectra as the gradual destruction of the regular

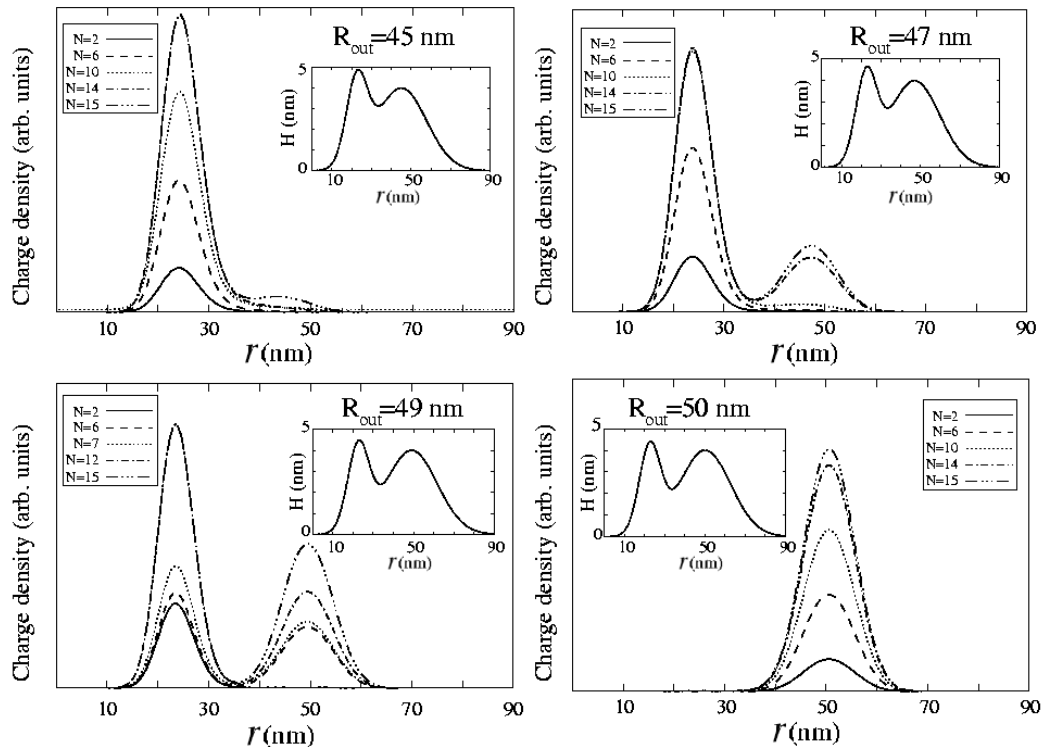


Figure 1.17: Radial charge-density distribution of N noninteracting electrons in DQRs with $R_{in} = 22.5$ nm and changing R_{out} . The insets illustrate the DQR cross-section profile.

single-QR pattern, which is replaced by lower peaks at ever smaller values of N . The reduced height of the incoming peaks is in part due to the smaller energy spacing between consecutive l 's in the outer ring. However, one should also take into account that the outer-ring levels intermix with the inner-ring ones, so that consecutive electrons may fill shells of different rings and, therefore, the height and distribution of the addition energy peaks is not simply that of the inner ring up to some value of N , plus that of the outer one for larger N 's. Instead, we generally observe a regular quantum-ring spectrum up to the filling of the last-but-one shell prior to the $(n = 1, l = 0)$ state, and afterwards the peaks become irregular in both height and position. The most complicated spectrum is found at $R_{out} = 49$ nm, when the lowest levels of the inner and outer rings are quasidegenerate. A further increase in the inter-ring separation from $R_{out} = 49$ to 50 nm already retrieves the regular spectrum of a single QR. This is because the density of states of the outer ring is much higher than that of the inner one. As a consequence, a slight stabilization of the outer-ring levels rapidly leads to a situation where many electrons can be hosted by it before reaching the first inner-ring level (see Fig. 1.16 for $R_{out} = 50$ nm).

The next step is to investigate the influence of the electron-electron interaction, which will be different in each ring since in general they have different volumes (we may say that the two rings have different 'electroaffinities' to draw again a parallel with ordinary molecules). In general, we expect that the Coulomb repulsion pushes the electrons towards the larger ring [Sza05], but this trend may be reversed when the latter contains too many

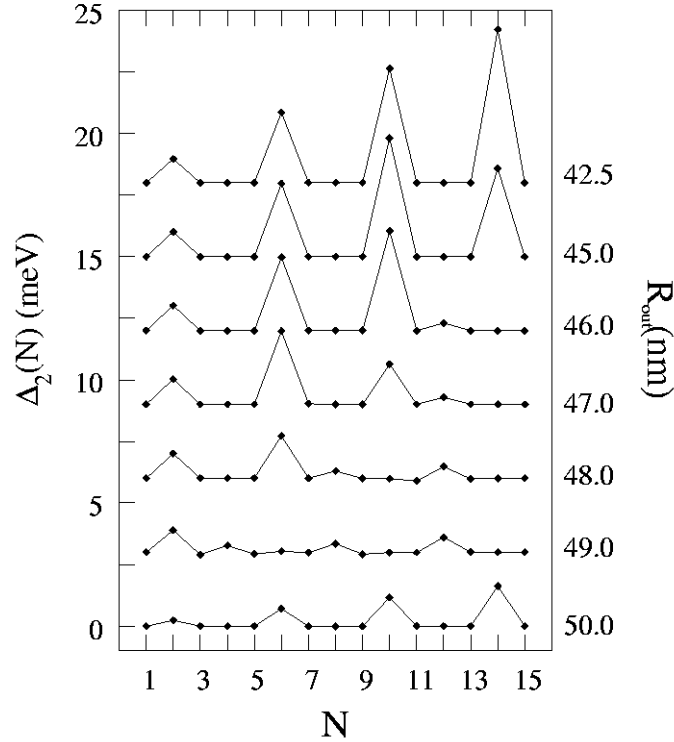


Figure 1.18: $\Delta_2(N)$ in noninteracting CDQRs with $R_{in} = 22.5$ nm and changing R_{out} .

particles. Fig. 1.19 depicts the radial charge densities of some N -electron ground states of CDQRs with increasing R_{out} , taking the direct Coulomb and the exchange-correlation contributions into account. We observe that the charging of the outer ring starts at smaller values of R_{out} than in the independent-particle case since the Coulomb interaction helps to compensate for its stronger vertical confinement. Indeed, for $R_{out} = 45$ nm, the 7th to 14th electrons already localize in the outer ring, whereas before this only happened from the $N = 15$ electron on. If we inspect the sp energy levels for $R_{out} = 45$ nm in Fig. 1.16 we notice that for the $N = 7$ electron to fill the lowest $n = 1$ state it skips as much as two empty shells of the inner ring ($(n = 0, l = 2)$ and $(n = 0, l = 3)$). This conspicuous violation of the Aufbau principle is made possible by the large difference between the Coulomb interaction strength in each ring as compared to that between the respective kinetic energies. The latter is smaller in the inner ring due to the weaker vertical confinement, but in it the electronic repulsion is stronger due to its smaller volume (see inset in Fig. 1.17). We also observe that the 15th electron localizes back again in the inner ring because of the accumulated electron charge in the outer one. Likewise, for $R_{out} = 50$ nm, despite the larger volume of the outer ring, the Coulomb interaction induces the localization of high- N states in the inner one. Nonetheless, the most complicated frame is found at $R_{out} \sim 47.5$ nm, where the Coulomb-energy stabilization provided by the electron localization in the outer ring is of the same order as the confinement-energy stabilization ensuing from localization in the inner one. As a result, the charge-density localization is extremely sensitive to the number of confined electrons. Hence, the $N = 1 - 2$ electrons

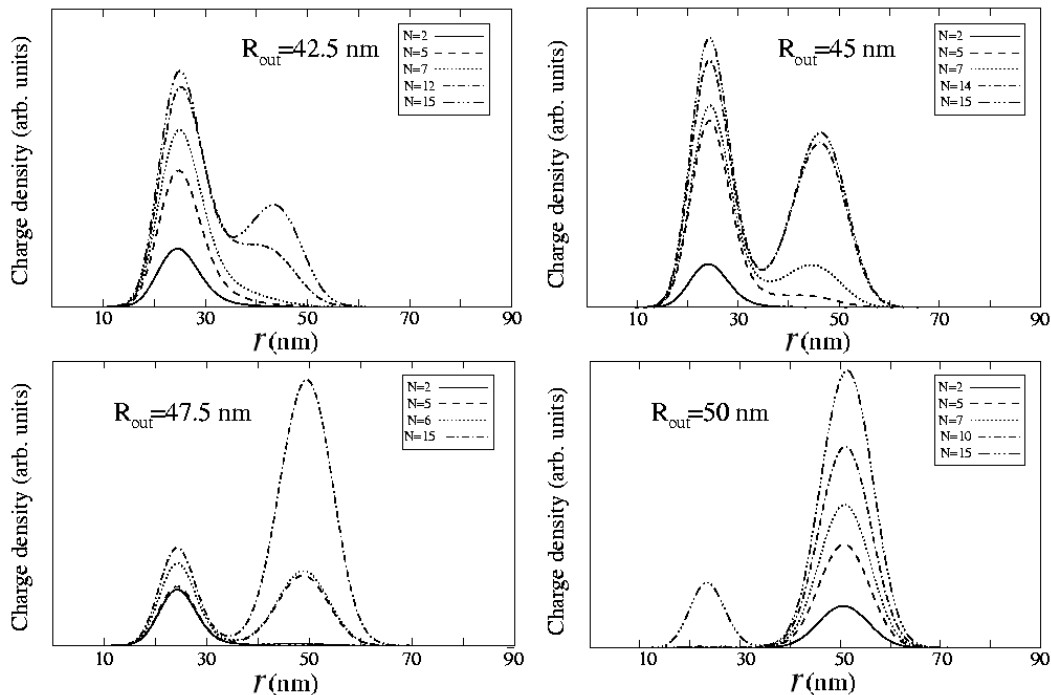


Figure 1.19: Same as Fig. 1.17 for the interacting CDQRs.

localize in the inner ring, the $N = 3 - 5$ do so in the outer ring, the $N = 6$ electron is inside again . . . In other words, around this inter-ring distance the Kohn-Sham orbitals localized in the inner and outer ring are very close in energy, hence yielding a strongly correlated system where the Coulomb-mediated inter-ring tunneling becomes very efficient. It is worth stressing that the entanglement in this structure arises from ‘molecular orbitals’ with similar energies but very different spatial distributions. Even though, as it has been shown in the previous section, a similar situation may appear in vertically coupled heteronuclear quantum rings, in the latter case it would be difficult to (experimentally) tune the appropriate barrier thickness for the dimensions of the constituent rings. In contrast, for CDQRs this situation follows naturally from the As-flux-controlled synthesis described in Ref. [Man05].

A striking feature of the entangled CDQR systems is the possibility of forming spin-dipolar ground states. This is illustrated in Fig. 1.20(a), where we show the $N = 12$ spin-up and spin-down charge densities for the CDQR with $R_{out} = 47.5$ nm. Interestingly, the charge density in the inner ring is completely spin-polarized, whereas in the outer one it is not. To understand this phenomenon, in Fig. 1.20(b) we show the corresponding Kohn-Sham sp energies. Solid and open triangles represent spin-orbitals localized in the inner and outer ring, respectively, with upward (downward)-pointing triangles accounting for spin-up (-down) states as usual. By comparison with the independent-particle energies of Fig. 1.16, it is clear that the electron-electron interaction is now playing a major role. In particular, the energy splitting between spin-up and spin-down levels in the inner ring is much larger than that in the outer one. Again, this is due to the stronger Coulomb

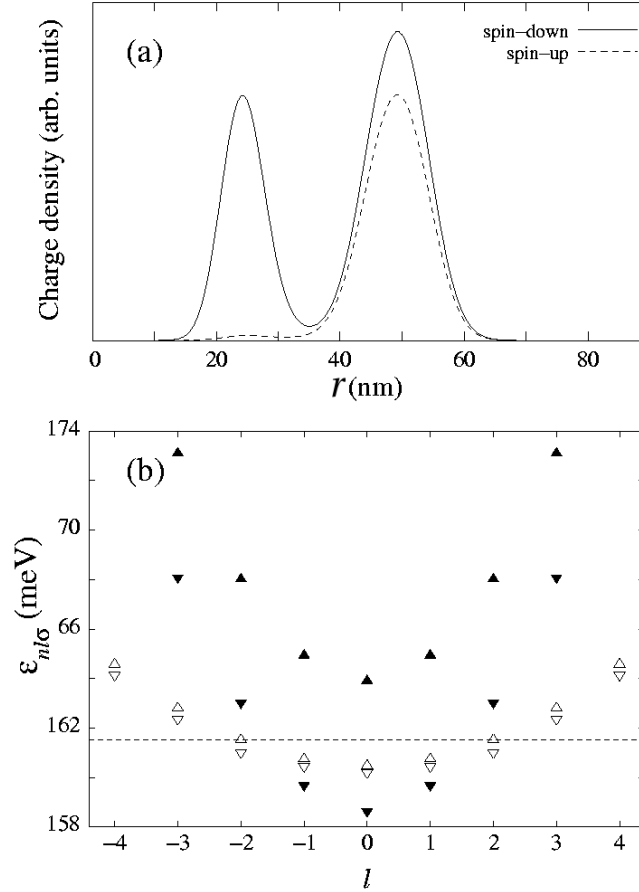


Figure 1.20: (a) Radial charge-density distribution and (b) KS orbital energies of the $N = 12$ ground state in a CDQR with $R_{in} = 22.5$ nm and $R_{out} = 47.5$ nm. In panel (b), solid (open) triangles represent orbitals localized in the inner (outer) ring.

interaction in the smaller ring, which gives rise to larger exchange-correlation energies thus favouring the appearance of locally strongly spin-polarized configurations.

Finally, in Fig. 1.21 we show the addition energy spectra and spin values of CDQRs with interacting electrons, as well as those of single QRs with radii $R = 22.5$ and 50 nm (dashed lines). The spectrum of the smallest single ring is regular, with maxima at closed-shell values of N (6, 10 and 14) and secondary maxima, arising from the exchange energy, at half-shell filling values ($N = 4, 8, 12$). One can realize that the peak at $N = 2$, corresponding to the filling of the $(n = 0, l = 0)$ shell, is missing. This is because the $(n = 0, l = 0)$ orbitals lie very close in energy to the $(n = 0, l = \pm 1)$ ones, due to the large radius of the ring. The spin sequence is well defined by Hund's rule. For $R_{out} = 30$ nm the confining potential is still that of a single QR, but the effective mean radius is slightly increased by the exiting outer ring. As a result, irregularities are introduced around $N = 3$, where now a local maximum shows up. This is due to the formation of an exchange-favoured $S_z = 3/2$ three-electron ground state, characteristic of QRs with large mean radius [Zhu05]. Since it could be argued that the LSDA provides a less accurate description of small- N systems, we have carried out calculations using the configuration interaction (CI) procedure of Ref. [Pla05], which confirm the spin-polarized gs for $N = 3$.

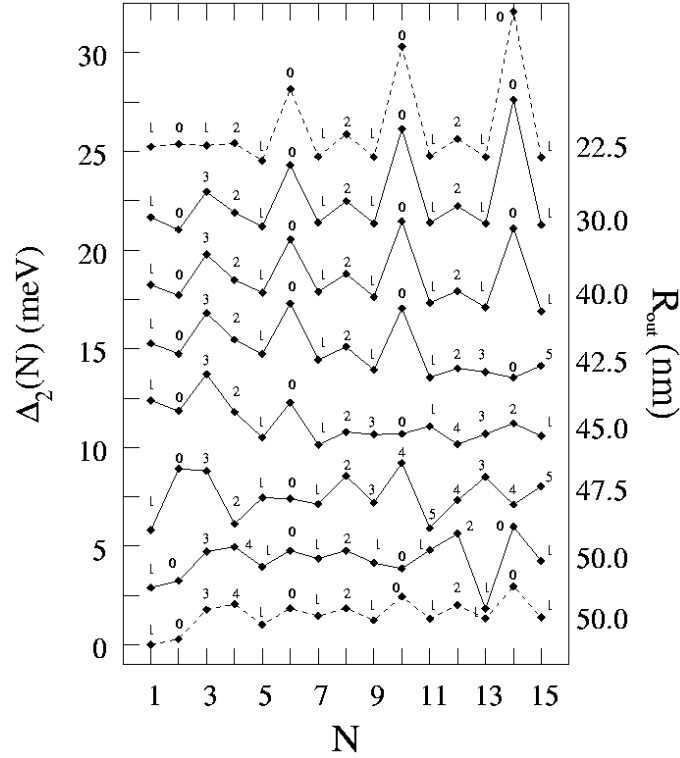


Figure 1.21: $\Delta_2(N)$ versus the number of confined interacting electrons in CDQRs with $R_{in} = 22.5$ nm and changing R_{out} (full lines). Single $R = 22.5$ and 50 nm quantum ring spectra are also shown for comparison (dashed lines). The values of $2S_z$ are also indicated.

Up to $R_{out} = 40$ nm, the spectrum remains almost constant, except for the increasing size of the $N = 3$ peak as the mean radius of the CDQR becomes larger (this is essentially a single-ring effect). For $R_{out} = 42.5$ and $R_{out} = 45$ nm, the flattening of the addition energy spectrum for decreasing values of N reflects the localization of electronic states in the outer ring. It can be observed that, once the first level of the outer ring is occupied, the spectrum no longer displays any regular pattern, which suggests that the system is then ruled by the Coulomb interaction. For $R_{out} \sim 47.5$ nm, when electronic correlations play the most important role, the entire spectrum is irregular. Finally, for $R_{out} = 50$ nm the spectrum resembles that of the single quantum ring with $R = 50$ nm up to $N = 9$ electrons, which means that the outer-ring low-lying energy levels are already more stable than the inner-ring ones (notice that the single QR with $R = 50$ nm has an irregular spectrum as well since it is dominated by the electron-electron interaction, owing to its large radius).

It must be pointed out that we have explored CDQRs with different sizes to determine the range of applicability of the shown results. On the one hand, for smaller CDQRs the physical behavior is similar, though the stronger kinetic energy reduces the range of inter-ring distances at which the electron-electron interaction is critical. On the other hand, for larger CDQRs the system soon enters the low-density regime and the Coulomb term leads to Wigner crystallization transitions [Ped02] for most inter-ring distances.

1.4.2 Variable perpendicular magnetic field

Once the effects of a variable inter-ring distance on the ground state of the CDQRs have been addressed, it is natural to investigate whether and how electron localization shows up as a function of other parameters of the system such as, e.g., a perpendicularly applied magnetic field, as well as the corresponding effects on another key observable like the longitudinal dipole response. The latter has been addressed for single quantum rings [Emp01], for which a wealth of experimental [Bay03, Fuh01, Fuh03, Ihn05, Lor00, War00] and theoretical [Aic06, Cha94, Cli03, Emp00, Hal96, Kos01, Lin01, Pro92, Pue01, Wen96, Zar96, Zhu05] work is available.

We consider now a strictly two-dimensional CDQR system in the interesting few-electron case, represented by a confining potential composed of two overlapping parabolae centered at different positions, which slightly generalizes that of Ref. [Sza05]:

$$V_{conf}(r) = \min \left\{ \frac{1}{2} \omega_1^2 (r - R_1)^2, \frac{1}{2} \omega_2^2 (r - R_2)^2 \right\} . \quad (1.48)$$

We have set the radii to the experimental values of Ref. [Kur05], namely $R_1 = 20$ nm and $R_2 = 40$ nm, whereas for the frequencies we have taken $\omega_1 = 30$ meV and $\omega_2 = 40$ meV, arbitrary though quite large values in order to mimic the strong confinement felt by the electrons in CDQRs. The election $\omega_2 > \omega_1$ somewhat compensates the fact that, since $R_2 \gg R_1$, the ‘surface’ of the outer ring might have been overestimated if we had taken both frequencies to be equal.

In Fig. 1.22 we show the squared wave functions $|u(r)|^2$ corresponding to the occupied KS orbitals for different electron numbers and intensities of the magnetic field. For $(N = 6, B = 0)$ the total spin of the CDQR is zero, and the spin-up and -down states corresponding to the same $(n, |l|)$ values are degenerate. As a consequence, there are only two different radial wave functions: one for s ($l = 0$) and another for p ($l = \pm 1$) orbitals. It can be seen that in this case the electrons are fairly delocalized within the CDQR; for the chosen confining potential, localized configurations would only appear at larger inter-ring distances, as we can expect from the results obtained in the previous section. However, the situation changes when switching on the magnetic field: for, e.g., $(N = 6, B = 5$ T) and $(N = 5, B = 4.5$ T), we can see that high- (low-) l orbitals are mostly localized in the outer (inner) ring, in spite of having solved the KS equations implicitly assuming a full coherence regime in which the electrons are allowed to occupy the whole CDQR surface. This can be intuitively understood from the knowledge of parabolical quantum dots, where, if only nodeless radial states are occupied, the sp orbitals are proportional to $x^{|l|} e^{-x^2/4}$, where $x \equiv r/a$ with $a \equiv \sqrt{\hbar/(2m\Omega)}$ and $\Omega \equiv \sqrt{\omega_0^2 + \omega_c^2/4}$. Of course, this is so only for a harmonic confining potential with frequency ω_0 , but some of that structure is expected to remain for ring confinements. Since these wave functions are peaked at $r_{max} \sim \sqrt{2|l|} a$, as B is increased the values of $|l|$ corresponding to occupied levels must increase as well so that r_{max} sensibly lies within the range of values of r spanned by the ring morphology. The same effect has been found for single QRs submitted to perpendic-

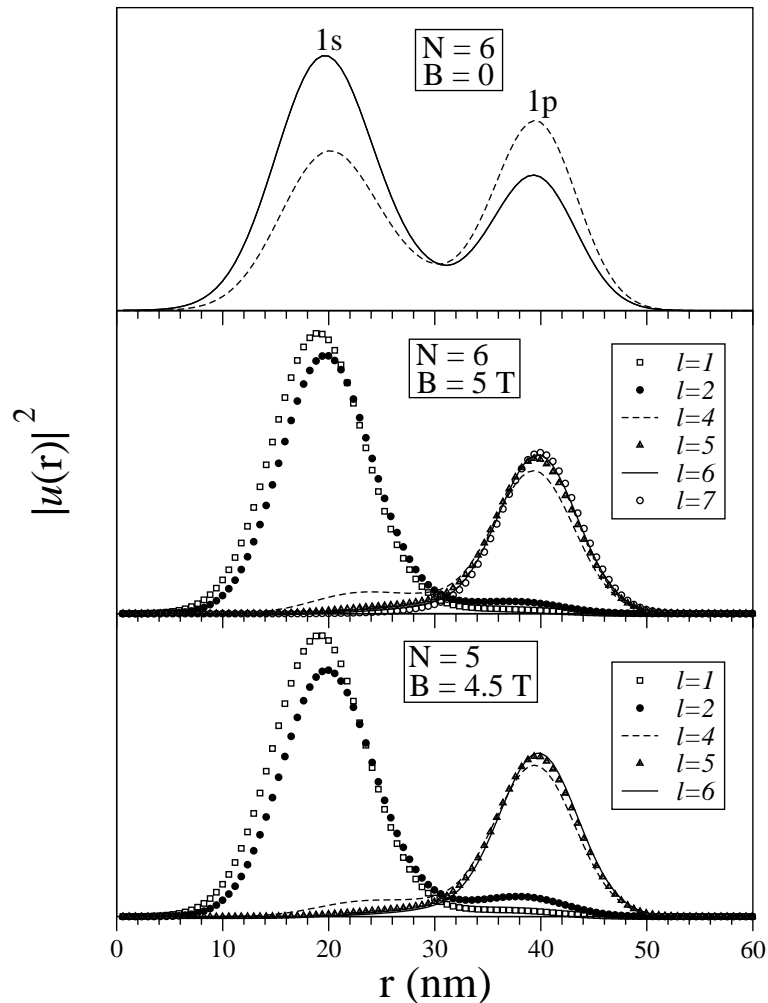


Figure 1.22: Top panel: Squared wave functions (arbitrary units) as a function of r (nm) of the occupied KS orbitals corresponding to $(N = 6, B = 0 \text{ T})$. Solid line, $1s$ state; dashed line, $1p$ state. Middle panel: same as top panel for $(N = 6, B = 5 \text{ T})$; all orbitals are spin-polarized. Notice that the $l = 3$ state is not occupied. Bottom panel: same as middle panel for $(N = 5, B = 4.5 \text{ T})$.

ular magnetic fields, where sp states with small values of l become progressively empty as B is increased [Emp99].

Fig. 1.23 displays the sp energy levels as a function of l for $N = 5$ and several values of the magnetic field. It can be seen that in most cases spin-up and -down orbitals corresponding to the same values of (n, l) are not degenerate due to the spin-magnetization-dependence of the exchange-correlation energy functional –notice that N is odd. Yet, some orbitals still present this degeneracy and, among them, some are occupied, like the $[(0, 1) \uparrow, \downarrow]$ ones at $B = 1 \text{ T}$ or the $[(0, 2) \uparrow, \downarrow]$ ones at $B = 2 \text{ T}$. This can be explained from the different spatial localization of these orbitals in the CDQR and the spin-magnetization distribution $m(r)$, which is shown in Fig. 1.24: at $B = 2 \text{ T}$, the $l = \pm 2$ sp orbitals are mostly localized in the outer ring, where the local magnetization is fairly small, with the same happening for the inner ring and the $l = \pm 1$ sp orbitals at $B = 3 \text{ T}$. Two facts

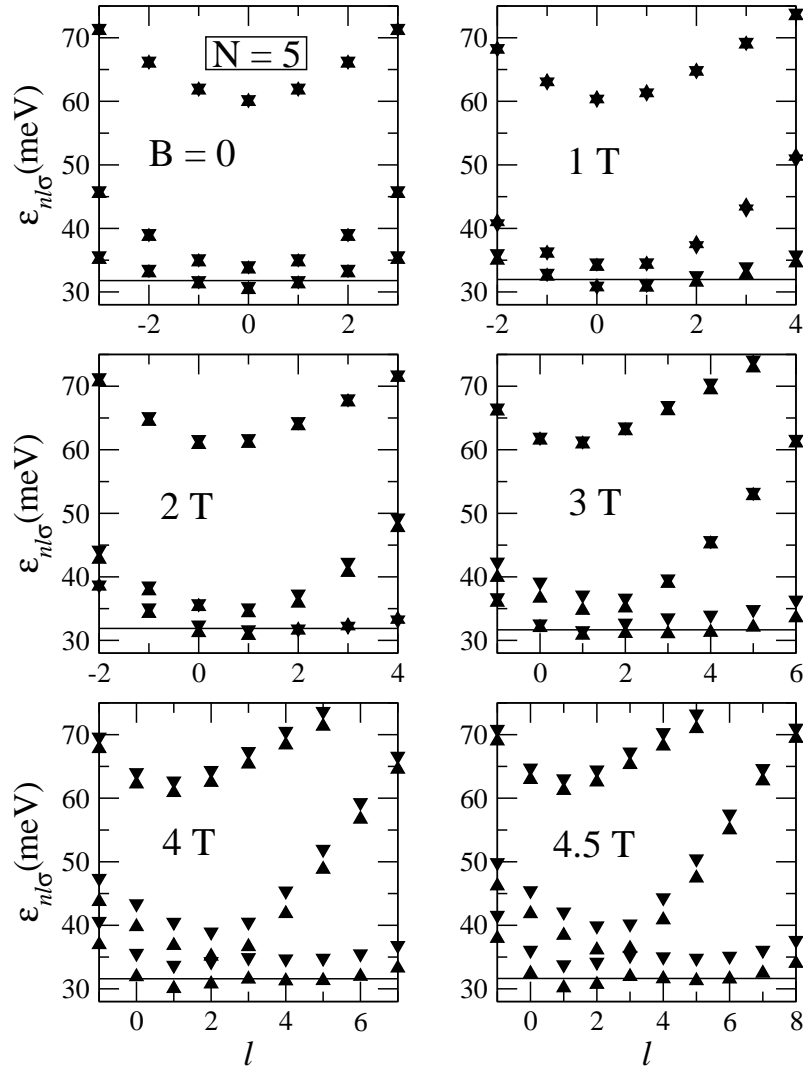


Figure 1.23: Sp energies (meV) for $N = 5$ and several values of B .

are worth to be pointed out when increasing B : on the one hand, the number of spin-up orbitals eventually becomes so large that the \uparrow, \downarrow degeneracy is fully broken (for $B > 3$ in the displayed cases). On the other hand, for some configurations one can find empty KS states having occupied l -neighbours. This is due to the double-well structure of the employed confining potential, which inhibits the filling of the orbitals whose ‘radius’ is close to that of the maximum of the inter-ring barrier. In the present case, this happens for $l = 3$ and, as we shall see, it is relevant for the understanding of the dipole response spectra.

From Fig. 1.23 one can also see that at low B ’s the delocalization regime yields a very regular sp energy pattern, with the electrons feeling simultaneously the confining potential of both rings. However, at higher values of the magnetic field the two lowest parabolic-like bands tend to cross between $l = 2$ and 3. Roughly speaking, each band arises from one of the constituent rings. This crossing is quantum-mechanically prevented (level repulsion), and also appears for the one-electron CDQR, as shown in Fig. 1.25 for $N = 1$ and $B = 4$ T. In this case, the spin-up and -down orbitals are nearly degenerate

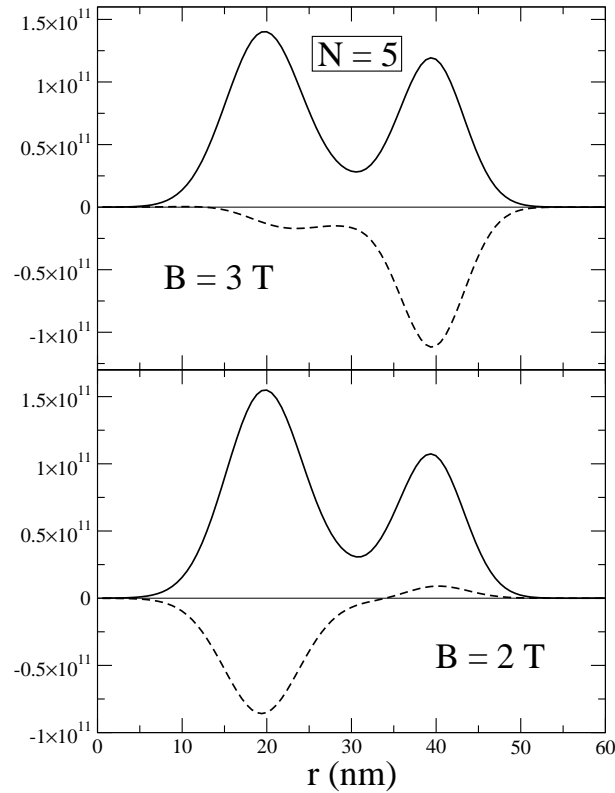


Figure 1.24: Electron density $n(r)$ (solid line) and spin magnetization $m(r)$ (dashed line) in cm^{-2} for $N = 5$ and $B = 2$ and 3 T.

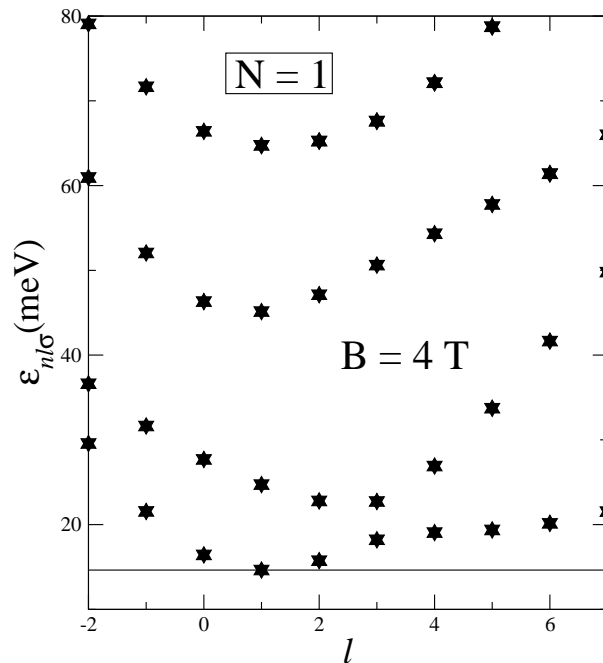


Figure 1.25: Single-electron energies (meV) of the $N = 1$ CDQR for $B = 4$ T.

due to the smallness of the Zeeman energy.

Once the gs has been determined, the dipole response can be worked out using the formalism described in section 1.1.2. It is experimentally known [Dah93, Lor00] that for

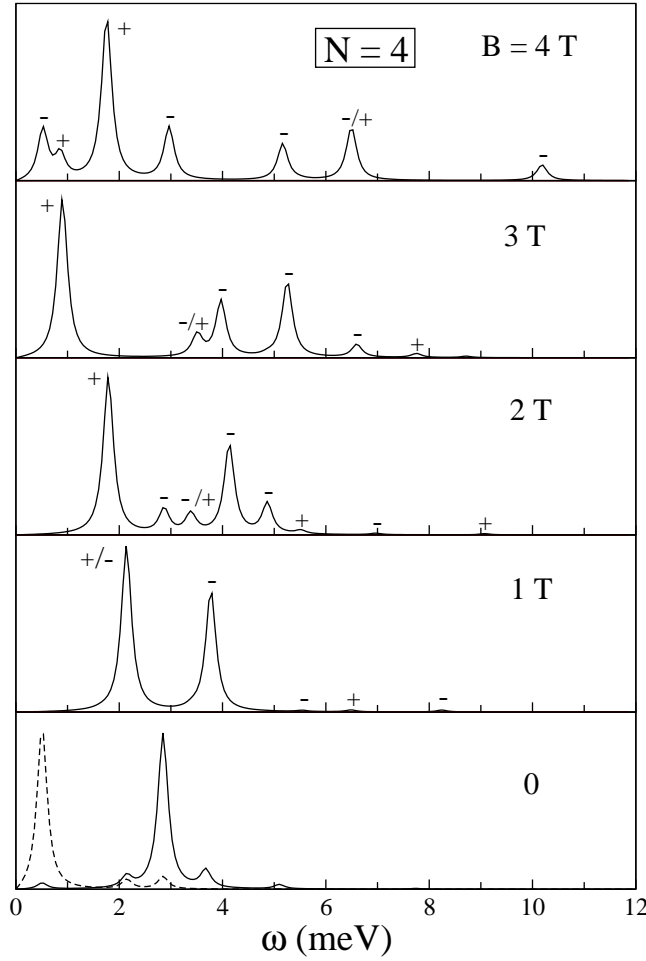
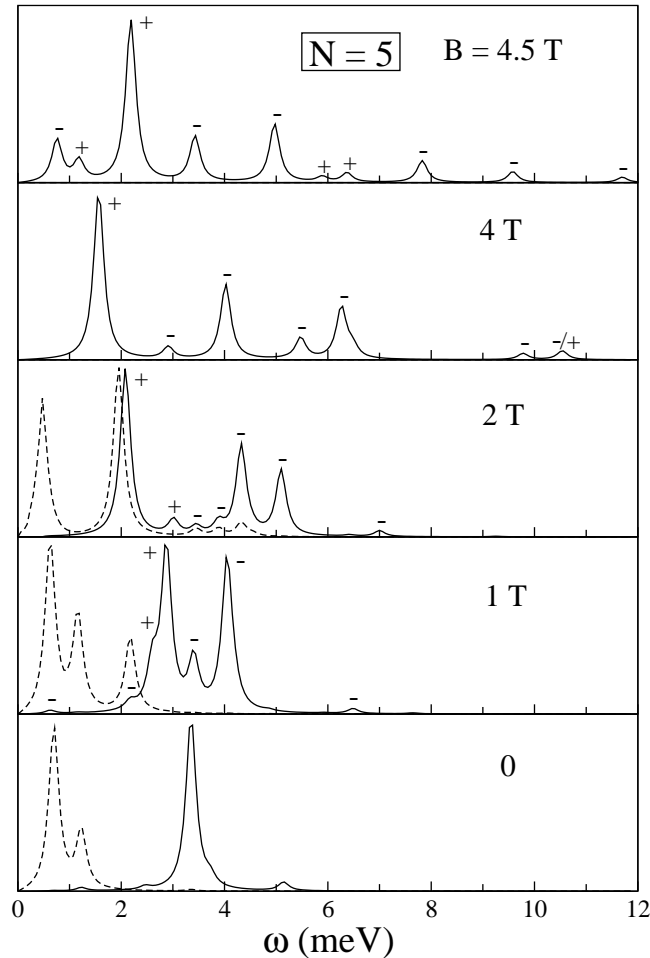


Figure 1.26: Charge-dipole (solid lines) and spin-dipole (dashed lines) strengths (arbitrary units) for the $N = 4$ CDQR as a function of the excitation energy (meV) and several values of B . The $(-)$ or $(+)$ symbol close to the more intense charge-density peaks denotes the character of the circular polarization. Some structures are superposition of peaks with different polarization, which is represented by a $'/'$ symbol with the polarization of the more intense peak indicated to the left of the slash. The intensities are fixed in such a way that, for a given B , the more intense peaks in both channels roughly have the same height.

a single QR the dipole spectrum as a function of an applied perpendicular magnetic field consists of several high- and low-frequency branches.

Figs. 1.26–1.28 show the charge- and spin-dipole strength functions for CDQRs with $N = 4–6$. In the delocalized regime, i.e. at low B 's, the physical pictures for a single ring and for a CDQR turn out to be similar: the magneto-excitations can be classified into bulk (high-energy) and edge (low-energy) modes, with the delocalization yielding only two effective edges: the inner and outer one of the smaller and larger ring, respectively. This can be easily understood from, e.g., the $B = 1$ and 2 T panels in Fig. 1.23. Bulk, high-energy peaks arise from non-spin-flip electronic excitations mostly involving $(\Delta n = 1, \Delta l = \pm 1)$ transitions (inter-‘Landau level’ excitations), whereas edge low-energy peaks come from non-spin-flip electronic excitations involving $(\Delta n = 0, \Delta l = \pm 1)$ transitions (intra-‘Landau level’ excitations). One thus expects that the B -dispersion of the bulk

Figure 1.27: Same as Fig. 1.26 for $N = 5$.

and edge modes split into two branches each, one corresponding to $\Delta l = +1$ and another to $\Delta l = -1$ (recall that the (\pm) excitations are induced by the dipole operators $D_A^{(\pm)}$). The $(-)$ edge modes are intra-‘Landau level’ excitations of the innermost boundary of the double ring system, whereas the $(+)$ edge modes are intra-‘Landau level’ excitations of the outermost boundary. This is in contrast with the quantum dot case [Ser99], since the $(-)$ edge mode is obviously absent for the dot geometry. The high-energy modes are bulk modes mostly of $(-)$ character, similarly to the cyclotron mode in quantum dots and wells, and carry much less strength, i.e., the corresponding peaks are less intense. Notice that at $B = 0$ the (\pm) excitations are degenerate and also that some modes present a fine structure (fragmentation) despite the tendency given by the effective interaction $K_{\sigma\sigma'}(\mathbf{r}, \mathbf{r}')$ to correlate the otherwise free-electron excitations, grouping them coherently into few excitation peaks. Also, even though the figures only show the low-energy (up to 12 meV) part of the dipole spectrum, some strength exists also in the form of low-intensity higher-energy modes arising from $\Delta n = 2$ electronic excitations, which can be easily identifiable in Fig. 1.23.

As a general rule, charge modes are at higher energies than spin modes because $K_{\sigma\sigma'}(\mathbf{r}, \mathbf{r}')$ is repulsive in the density channel, as it is essentially determined by the direct

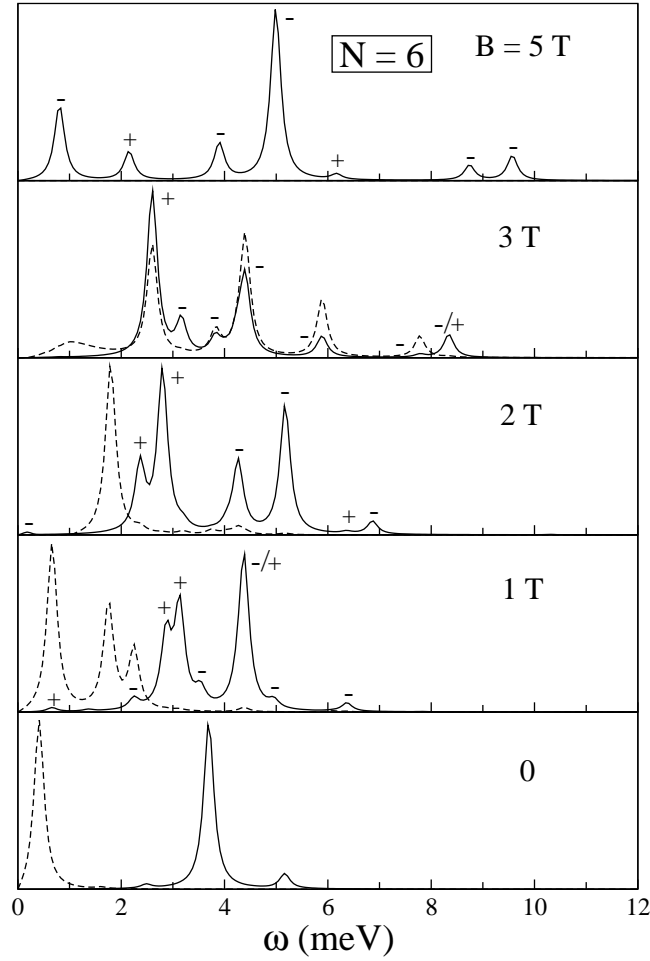


Figure 1.28: Same as Fig. 1.26 for $N = 6$.

Coulomb interaction, whereas it is attractive in the spin channel, related to the exchange-correlation contribution. However, one can see that in some situations the spin and the charge strengths are coupled, i.e., spin (charge) modes can be ‘seen’ in the charge (spin) channel. As discussed in Ref. [Ser99], the coupling between spin and charge modes may appear when the gs configuration has a non-zero total spin. Obviously, when the system is fully polarized both responses coincide and we have plotted only one of them.

Finally, we discuss the interesting localized regime, exemplified here by the configurations ($N = 4, B = 4$ T), ($N = 5, B = 4.5$ T) and ($N = 6, B = 5$ T) (Figs. 1.26, 1.27 and 1.28, respectively). In this case, the response of the CDQRs deviates from that of single rings. The above-mentioned fact that for these configurations the $l = 3$ KS orbital is empty makes it possible to generate additional low-energy modes at the inner and outer boundaries of *both* rings. This yields the appearance of a richer dipole response, with two series of $(-)$ and $(+)$ polarization edge modes instead of just one.

Chapter 2

Spin-orbit effects in quantum nanostructures

The fabrication process of quantum nanostructures begins with the creation of a quasi-two-dimensional electron gas (Q2DEG) –or quantum well– originated from the superposition of semiconductor layers with different bandgaps. A simplified vision of the procedure consists in thinking of the quantum well as an ‘infinite sheet of paper’ from which quantum dots, rings or wires are ‘cut out’ by using as ‘scissors’ different kinds of nanolithographic techniques. Of course, the actual realization of these systems is much more intricate and, due to the complexity of manipulating Matter at the nanoscale, the unintentional introduction of asymmetries becomes unavoidable. As a matter of fact, the initial quantum well is not symmetric itself [And82], as can be intuitively inferred from the schematic picture shown in Fig. 2.1. Moreover, the usually employed semiconductor compounds in nanostructure fabrication, such as e.g. GaAs, have Zinc Blende structure –shown in Fig. 2.2–, which lacks of inversion symmetry, i.e., it is not invariant under the transformation $\mathbf{r} \rightarrow -\mathbf{r}$ for the position of each atom in the Bravais lattice.

Such asymmetries can give rise to the presence of macroscopic electric fields in the nanostructures that, as a consequence of Special Relativity, transform in the reference frame of the confined conduction electrons into effective magnetic fields, coupling to the electronic spins and giving rise to the so-called *spin-orbit* (SO) *interaction*. Two are the most commonly considered contributions to the SO coupling in confined electron gases: the one arising from the *bulk inversion asymmetry* (BIA) of the crystal lattice structure of the substrate material, which is described by the Hamiltonian [Dre55]

$$H_D = \frac{\lambda_D}{\hbar} \sum_{j=1}^N [P_x \sigma_x - P_y \sigma_y]_j \quad (2.1)$$

and known as the Dresselhaus SO contribution, and the one due to the non-perfectly-square shape of the initial quantum well confining the Q2DEG and so-called *structure inversion asymmetry* (SIA), given by [Byc84]

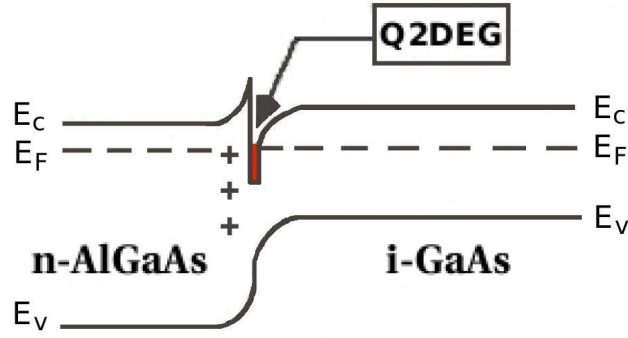


Figure 2.1: Schematic picture representing the formation of a GaAs quantum well.

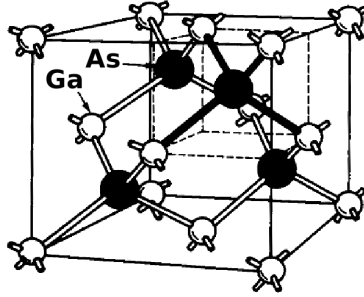


Figure 2.2: Zinc blende lattice structure of GaAs.

$$H_R = \frac{\lambda_R}{\hbar} \sum_{j=1}^N [P_y \sigma_x - P_x \sigma_y]_j, \quad (2.2)$$

which is referred to as the Bychkov-Rashba –usually just ‘Rashba’ for short– term. One could also consider possible asymmetries in the lateral confinements [Mor99] introduced when creating e.g. a quantum wire, but we do not have taken them into account here.

The parameters λ_D and λ_R give the intensity of the respective couplings and can be experimentally determined [Kna96]. While the one corresponding to the Dresselhaus term is fixed for a given semiconductor layer –in particular it is inversely proportional to the width of the latter–, the Rashba parameter has been proven to be externally tunable by the application of gate voltages [Nit97]. This can be of great potential technological interest since, as said above, to each source of SO interaction it can be associated an effective magnetic field, about which the spins will precess. Therefore, tailoring the spin-orbit coupling might translate into a control over the electron spin. This is the goal of an emerging field called *Spintronics* that aims to exploit this intrinsic property of the electrons for multiple practical applications, such as e.g. quantum information, and promises remarkable new devices, faster, smaller and more powerful than those currently existing, which are based on the electron charge.

As a consequence, an intense activity in the study of spin-orbit effects in semiconductor nanostructures has been prompted [And99, Cal05, Can99, Fol01b, Hal01, Kon05, Mal00, Mor99, Per04, Rac97, Ric99, Sch03, Ser05, Val02b, Vos01]. In this second chapter we

address the spin-orbit effects on quantum wells and wires with Rashba and Dresselhaus couplings and submitted to external magnetic fields.

2.1 Quantum wells submitted to perpendicular magnetic fields

The extraction from measurements of the coupling constant of both the Rashba and Dresselhaus interactions is not a simple matter, since the SO corrections to the electron energy spectrum in a magnetic field are vanishingly small as they correspond to second-order effects in perturbation theory. Thus, few physical observables are sensitive enough to this interaction and allow for a quantitative estimate of the coupling parameters. One such observable is the splitting of the cyclotron resonance (CR), which has been determined in far-infrared transmission experiments [Man01] and is due to the coupling between charge-density and spin-density excitations [Ton04]. A less clear example is the change in the Larmor frequency –spin splitting–, which has been observed in electron-spin resonance (ESR) [Dob88, Ste82] and in inelastic light scattering (ILS) experiments [Dav97, Kan00].

Here we consider a two-dimensional GaAs quantum well with both Rashba and Dresselhaus SO couplings submitted to a perpendicular magnetic field. By using an approximate –yet very accurate– analytical approach to the problem we are able to study the SO corrections to the Landau levels in a simple way, as well as the transitions induced by an external electromagnetic field acting upon the system.

2.1.1 Single-particle states

The quantum well is described by the Hamiltonian $H = H_0 + \frac{e^2}{\epsilon} \sum_{i<j=1}^N \frac{1}{|\mathbf{r}_i - \mathbf{r}_j|}$, where H_0 is the one-body part

$$H_0 \equiv \sum_{j=1}^N [h_0]_j = \sum_{j=1}^N \left[\frac{P^+ P^- + P^- P^+}{4m} + \frac{1}{2} g^* \mu_B B \sigma_z + \frac{\lambda_R}{2i\hbar} (P^+ \sigma_- - P^- \sigma_+) + \frac{\lambda_D}{2\hbar} (P^+ \sigma_+ + P^- \sigma_-) \right]_j, \quad (2.3)$$

consisting of the kinetic, Zeeman, Rashba and Dresselhaus contributions, written in terms of $P^\pm \equiv P_x \pm iP_y$ and $\sigma_\pm \equiv \sigma_x \pm i\sigma_y$. The potential vector has been chosen in the Landau gauge, namely $\mathbf{A} = B(0, x, 0)$ yielding $\mathbf{B} = \nabla \times \mathbf{A} = B\hat{z}$. Introducing the operators

$$a^\pm = \frac{1}{\sqrt{2\omega_c}} P^\pm, \quad (2.4)$$

which satisfy the relation $[a^-, a^+] = 1$, the sp Hamiltonian h_0 can be rewritten as

$$h_0/\omega_c = \frac{1}{2}(a^+ a^- + a^- a^+) - \frac{1}{2} \frac{\omega_L}{\omega_c} \sigma_z - \frac{1}{2} i\tilde{\lambda}_R (a^+ \sigma_- - a^- \sigma_+) + \frac{1}{2} \tilde{\lambda}_D (a^+ \sigma_+ + a^- \sigma_-) \quad , \quad (2.5)$$

where $\omega_L = |g^* \mu_B B|$ is the Larmor frequency and $\tilde{\lambda}_{R,D} \equiv \lambda_{R,D} \sqrt{\frac{2}{\omega_c}}$. Clearly, from the hamiltonians Eqs. (2.1) and (2.2) one can see that in the presence of spin-orbit coupling the states of the system are given by two-component spinors $|\varphi\rangle \equiv \begin{pmatrix} \varphi_1 \\ \varphi_2 \end{pmatrix}$. The Schrödinger equation $h_0|\varphi\rangle = \varepsilon|\varphi\rangle$ thus reads

$$\begin{bmatrix} \frac{1}{2}(a^+a^- + a^-a^+) - \omega_L/(2\omega_c) - \varepsilon & i\tilde{\lambda}_R a^- + \tilde{\lambda}_D a^+ \\ -i\tilde{\lambda}_R a^+ + \tilde{\lambda}_D a^- & \frac{1}{2}(a^+a^- + a^-a^+) + \omega_L/(2\omega_c) - \varepsilon \end{bmatrix} \begin{pmatrix} \varphi_1 \\ \varphi_2 \end{pmatrix} = 0 \quad , \quad (2.6)$$

where it has been used the label ‘1’ (‘2’) for the top (bottom) component of the spinors. One can expand φ_1 and φ_2 into oscillator states $|n\rangle$ as $\varphi_1 = \sum_{n=0}^{\infty} a_n |n\rangle$, $\varphi_2 = \sum_{n=0}^{\infty} b_n |n\rangle$, on which a^+ and a^- act in the usual way, i.e., $\frac{1}{2}(a^+a^- + a^-a^+)|n\rangle = (n + \frac{1}{2})|n\rangle$, $a^+|n\rangle = \sqrt{n+1}|n+1\rangle$, $a^-|n\rangle = \sqrt{n}|n-1\rangle$, and $a^-|0\rangle = 0$. This yields the infinite system of equations

$$\begin{aligned} (n + \alpha - \varepsilon)b_n - i\tilde{\lambda}_R \sqrt{n} a_{n-1} + \tilde{\lambda}_D \sqrt{n+1} a_{n+1} &= 0 \\ (n + \beta - \varepsilon)a_n + i\tilde{\lambda}_R \sqrt{n+1} b_{n+1} + \tilde{\lambda}_D \sqrt{n} b_{n-1} &= 0 \end{aligned} \quad (2.7)$$

for $n \geq 0$, with $a_{-1} = 0$, $b_{-1} = 0$, and $\alpha \equiv (1 + \omega_L/\omega_c)/2$, $\beta \equiv (1 - \omega_L/\omega_c)/2$.

It has already been shown [Das90, Fal93, Ras60, Sch03] that when only either the Rashba or the Dresselhaus term is considered, Eqs. (2.7) can be exactly solved. Indeed, in the e.g. $\lambda_D = 0$ case, by combining both equations one obtains

$$\begin{aligned} [(n + \alpha - \varepsilon)(n - 1 + \beta - \varepsilon) - n \tilde{\lambda}_R^2] b_n &= 0 \\ [(n + \alpha - \varepsilon)(n - 1 + \beta - \varepsilon) - n \tilde{\lambda}_R^2] a_{n-1} &= 0 \quad , \end{aligned} \quad (2.8)$$

yielding the energies (in ω_c units)

$$\varepsilon_n^\pm \equiv n \pm \sqrt{\frac{1}{4} \left(1 + \frac{\omega_L}{\omega_c}\right)^2 + \frac{2}{\omega_c} \lambda_R^2 n} \quad (2.9)$$

and also the relations

$$(n - 1 + \beta - \varepsilon_n^\pm) a_{n-1}^\pm = -i\tilde{\lambda}_R \sqrt{n} b_n^\pm \quad , \quad (2.10)$$

where a_{n-1}^\pm and b_n^\pm represent, respectively, the $(n-1)$ th and n th coefficient of the basis expansion for the components $|\varphi_1\rangle$ and $|\varphi_2\rangle$ of the spinor $|\varphi\rangle$ with energy ε_n^\pm . Since $\beta \leq \alpha$ and by analogy with the situation without spin-orbit interaction, from Eqs. (2.9) and (2.10) we can see that the ‘-’ and ‘+’ solutions correspond to ‘up’ and ‘down’ eigenstates respectively, which we shall therefore denote as $|n_u\rangle$ and $|n_d\rangle$. In addition, from Eqs. (2.8) one can see that only one of the coefficients $-a_i$ or b_i appears in the corresponding series expansion of the spinor components, which read

$$|n_d\rangle = \begin{pmatrix} a_{n-1}^+ |n-1\rangle \\ b_n^+ |n\rangle \end{pmatrix} ; \quad |n_u\rangle = \begin{pmatrix} a_n^- |n\rangle \\ b_{n+1}^- |n+1\rangle \end{pmatrix} \quad , \quad (2.11)$$

and yield, respectively, the normalization conditions $|a_{n-1}^{\varepsilon_n^+}|^2 + |b_n^{\varepsilon_n^+}|^2 = 1$ and $|a_n^{\varepsilon_n^-}|^2 + |b_{n+1}^{\varepsilon_n^-}|^2 = 1$ (for $n = 0$, $a_{-1}^{\varepsilon_0^+} = b_1^{\varepsilon_0^-} = 0$, $a_0^{\varepsilon_0^-} = b_0^{\varepsilon_0^+} = 1$, and $\varepsilon_0^\pm = \frac{1}{2}(1 \pm \omega_L/\omega_c)$).

The $\lambda_R = 0$ case can be worked out similarly. In this case one obtains the secular equation

$$(n + \beta - \varepsilon)(n - 1 + \alpha - \varepsilon) - n \tilde{\lambda}_D^2 = 0, \quad (2.12)$$

yielding

$$\varepsilon_n^\pm \equiv n \pm \sqrt{\frac{1}{4} \left(1 - \frac{\omega_L}{\omega_c}\right)^2 + \frac{2}{\omega_c} \lambda_D^2 n} \quad (2.13)$$

and the relations

$$(n - 1 + \alpha - \varepsilon_n^\pm) b_{n-1}^{\varepsilon_n^\pm} = -\tilde{\lambda}_D \sqrt{n} a_n^{\varepsilon_n^\pm}. \quad (2.14)$$

One has now

$$|n_d\rangle = \begin{pmatrix} a_{n+1}^{\varepsilon_n^-} |n+1\rangle \\ b_n^{\varepsilon_n^-} |n\rangle \end{pmatrix}; \quad |n_u\rangle = \begin{pmatrix} a_n^{\varepsilon_n^+} |n\rangle \\ b_{n-1}^{\varepsilon_n^+} |n-1\rangle \end{pmatrix}, \quad (2.15)$$

and the normalization conditions $|a_{n+1}^{\varepsilon_n^-}|^2 + |b_n^{\varepsilon_n^-}|^2 = 1$ and $|a_n^{\varepsilon_n^+}|^2 + |b_{n-1}^{\varepsilon_n^+}|^2 = 1$ (for $n = 0$, $a_1^{\varepsilon_0^-} = b_{-1}^{\varepsilon_0^+} = 0$, $a_0^{\varepsilon_0^+} = b_0^{\varepsilon_0^-} = 1$, and $\varepsilon_0^\pm = \frac{1}{2}(1 \mp \omega_L/\omega_c)$). The coefficients a_i and b_i can be easily exactly calculated. Expressions valid up to order $\lambda_{R,D}^2$ are obtained below showing that, in the limit of zero spin-orbit coupling, the spinors $|n_u\rangle$ and $|n_d\rangle$ become, respectively, $|n\rangle \begin{pmatrix} 0 \\ 1 \end{pmatrix}$ and $|n\rangle \begin{pmatrix} 1 \\ 0 \end{pmatrix}$. Therefore, in the following we shall refer to them as to the quasi-spin-down ($|n_d\rangle$) and quasi-spin-up ($|n_u\rangle$) spinors (qdown and qup for short).

When both SO terms are simultaneously considered, from Eq. (2.7) one can see that this interaction couples the states of all Landau levels (the series expansions have now an infinite number of terms) and an exact analytical solution is unknown, and likely does not exist. Nevertheless, it is possible to find an approximate solution that, as we shall see, in the $\lambda_{R,D}^2/\omega_c \ll 1$ limit coincides with the results of second-order perturbation theory –i.e. it is valid up to order $\tilde{\lambda}_{R,D}^2$ – and that it is quite accurate as compared with numerically obtained exact results. This limit is justified by the fact that the known values of the SO parameters $\lambda_{R,D}^2$ for the GaAs are of the order of 10 μeV whereas ω_c is of the order of the meV even at small B (~ 1 T). In this general case, the combination of Eqs. (2.7) yields

$$\begin{aligned} & \left[n + \alpha - \varepsilon - \tilde{\lambda}_R^2 \frac{n}{n-1+\beta-\varepsilon} - \tilde{\lambda}_D^2 \frac{n+1}{n+1+\beta-\varepsilon} \right] b_n = \\ & -i \tilde{\lambda}_R \tilde{\lambda}_D \left[\frac{\sqrt{n(n-1)}}{n-1+\beta-\varepsilon} b_{n-2} - \frac{\sqrt{(n+1)(n+2)}}{n+1+\beta-\varepsilon} b_{n+2} \right] \end{aligned} \quad (2.16)$$

and

$$\begin{aligned} & \left[n + \beta - \varepsilon - \tilde{\lambda}_R^2 \frac{n+1}{n+1+\alpha-\varepsilon} - \tilde{\lambda}_D^2 \frac{n}{n-1+\alpha-\varepsilon} \right] a_n = \\ & -i \tilde{\lambda}_R \tilde{\lambda}_D \left[\frac{\sqrt{n(n-1)}}{n-1+\alpha-\varepsilon} a_{n-2} - \frac{\sqrt{(n+1)(n+2)}}{n+1+\alpha-\varepsilon} a_{n+2} \right]. \end{aligned} \quad (2.17)$$

The approximation consists in taking $a_{n-2} = a_{n+2} = b_{n-2} = b_{n+2} = 0$ in the above equations, implying that each level $|n\rangle$ is coupled only to the $|n-1\rangle$ and $|n+1\rangle$ states. The solution is therefore obtained by solving the secular, cubic equations

$$(n+\alpha-\varepsilon)(n-1+\beta-\varepsilon)(n+1+\beta-\varepsilon) = \tilde{\lambda}_R^2 n(n+1+\beta-\varepsilon) + \tilde{\lambda}_D^2 (n+1)(n-1+\beta-\varepsilon) \quad (2.18)$$

and

$$(n+\beta-\varepsilon)(n-1+\alpha-\varepsilon)(n+1+\alpha-\varepsilon) = \tilde{\lambda}_R^2 (n+1)(n-1+\alpha-\varepsilon) + \tilde{\lambda}_D^2 n(n+1+\alpha-\varepsilon) \quad (2.19)$$

Together with the relations extracted from Eqs. (2.16) and (2.17),

$$\begin{aligned} (n-1+\beta-\varepsilon)a_{n-1} &= -i\tilde{\lambda}_R\sqrt{n}b_n \\ (n+1+\beta-\varepsilon)a_{n+1} &= -\tilde{\lambda}_D\sqrt{n+1}b_n \\ |a_{n-1}^{\varepsilon_n^d}|^2 + |a_{n+1}^{\varepsilon_n^d}|^2 + |b_n^{\varepsilon_n^d}|^2 &= 1 \end{aligned} \quad (2.20)$$

and

$$\begin{aligned} (n-1+\alpha-\varepsilon)b_{n-1} &= -\tilde{\lambda}_D\sqrt{n}a_n \\ (n+1+\alpha-\varepsilon)b_{n+1} &= i\tilde{\lambda}_R\sqrt{n+1}a_n \\ |a_n^{\varepsilon_n^u}|^2 + |b_{n-1}^{\varepsilon_n^u}|^2 + |b_{n+1}^{\varepsilon_n^u}|^2 &= 1, \end{aligned} \quad (2.21)$$

they determine, respectively, the quasi-spin-down and quasi-spin-up solutions:

$$|n_d\rangle = \begin{pmatrix} a_{n-1}^{\varepsilon_n^d} |n-1\rangle + a_{n+1}^{\varepsilon_n^d} |n+1\rangle \\ b_n^{\varepsilon_n^d} |n\rangle \end{pmatrix} \quad (2.22)$$

for the qdown one, with

$$\varepsilon_n^d = n + \alpha + 2n \frac{\lambda_R^2}{\omega_c + \omega_L} - 2(n+1) \frac{\lambda_D^2}{\omega_c - \omega_L}, \quad (2.23)$$

$$\begin{aligned} a_{n-1}^{\varepsilon_n^d} &= i\tilde{\lambda}_R\sqrt{n} \frac{\omega_c}{\omega_c + \omega_L} \\ a_{n+1}^{\varepsilon_n^d} &= -\tilde{\lambda}_D\sqrt{n+1} \frac{\omega_c}{\omega_c - \omega_L} \\ b_n^{\varepsilon_n^d} &= 1 - \frac{1}{2}\tilde{\lambda}_R^2 n \left(\frac{\omega_c}{\omega_c + \omega_L} \right)^2 - \frac{1}{2}\tilde{\lambda}_D^2 (n+1) \left(\frac{\omega_c}{\omega_c - \omega_L} \right)^2, \end{aligned} \quad (2.24)$$

and

$$|n_u\rangle = \begin{pmatrix} a_n^{\varepsilon_n^u} |n\rangle \\ b_{n-1}^{\varepsilon_n^u} |n-1\rangle + b_{n+1}^{\varepsilon_n^u} |n+1\rangle \end{pmatrix} \quad (2.25)$$

for the qup one, with

$$\varepsilon_n^u = n + \beta - 2(n+1) \frac{\lambda_R^2}{\omega_c + \omega_L} + 2n \frac{\lambda_D^2}{\omega_c - \omega_L}, \quad (2.26)$$

$$\begin{aligned}
b_{n-1}^{\varepsilon_n^u} &= \tilde{\lambda}_D \sqrt{n} \frac{\omega_c}{\omega_c - \omega_L} \\
b_{n+1}^{\varepsilon_n^u} &= i \tilde{\lambda}_R \sqrt{n+1} \frac{\omega_c}{\omega_c + \omega_L} \\
a_n^{\varepsilon_n^u} &= 1 - \frac{1}{2} \tilde{\lambda}_R^2 (n+1) \left(\frac{\omega_c}{\omega_c + \omega_L} \right)^2 - \frac{1}{2} \tilde{\lambda}_D^2 n \left(\frac{\omega_c}{\omega_c - \omega_L} \right)^2 .
\end{aligned} \tag{2.27}$$

It is easy to check that when either λ_R or λ_D is zero Eqs. (2.22) and (2.25) reduce, respectively, to the exact results (2.11) and (2.15) whereas the corresponding a_i and b_i coefficients, valid up to order $\lambda_{R,D}^2$, can be extracted from Eqs. (2.24) and (2.27). One can see that the pairs (a_n, b_n) , $(a_{n\pm 1}, b_{n\pm 1})$ and $(a_{n\pm 2}, b_{n\pm 2})$ are, respectively, of order $O(1)$, $O(\lambda_{R,D})$ and $O(\lambda_{R,D}^2)$. Therefore, the neglected terms in Eqs. (2.16) and (2.17) are of order $O(\lambda_{R,D}^4)$.

From Eqs. (2.23) and (2.26) one obtains, in the $\lambda_{R,D}^2/\omega_c \ll 1$ limit, the spin-orbit-corrected Landau levels:

$$\begin{aligned}
E_n^d &= \left(n + \frac{1}{2}\right)\omega_c + \frac{\omega_L}{2} + 2n\lambda_R^2 \frac{\omega_c}{\omega_c + \omega_L} - 2(n+1)\lambda_D^2 \frac{\omega_c}{\omega_c - \omega_L} \\
E_n^u &= \left(n + \frac{1}{2}\right)\omega_c - \frac{\omega_L}{2} - 2(n+1)\lambda_R^2 \frac{\omega_c}{\omega_c + \omega_L} + 2n\lambda_D^2 \frac{\omega_c}{\omega_c - \omega_L} .
\end{aligned} \tag{2.28}$$

It can be checked that they coincide with those derived from second-order perturbation theory using the standard expression

$$E_n^{(2)} = \frac{1}{4} \sum_{m \neq n} \frac{|\langle m | -i\tilde{\lambda}_R \omega_c (a^+ \sigma_- - a^- \sigma_+) + \tilde{\lambda}_D \omega_c (a^+ \sigma_+ + a^- \sigma_-) | n \rangle|^2}{E_n^{(0)} - E_m^{(0)}} , \tag{2.29}$$

where $|n\rangle = |n, \uparrow\rangle$, $|n, \downarrow\rangle$ are the spin-up and spin-down eigenstates of the sp Hamiltonian $\frac{1}{2}(a^+ a^- + a^- a^+) \omega_c - \frac{1}{2} \omega_L \sigma_z$ with eigenvalues $E_n^{(0)}(\uparrow) = (n + \frac{1}{2})\omega_c - \frac{1}{2}\omega_L$ and $E_n^{(0)}(\downarrow) = (n + \frac{1}{2})\omega_c + \frac{1}{2}\omega_L$, respectively.

The approximate energies Eq. (2.28) are very accurate in the high- B limit (see below), but they also carry interesting information in the opposite limit of vanishing magnetic field. In this regime ($\omega_L, \omega_c \ll \lambda_{R,D}^2$), Eqs. (2.18) and (2.19) yield the solutions

$$\begin{aligned}
E_n^d &= \sqrt{2\omega_c [n\lambda_R^2 + (n+1)\lambda_D^2]} \\
E_n^u &= \sqrt{2\omega_c [(n+1)\lambda_R^2 + n\lambda_D^2]} ,
\end{aligned} \tag{2.30}$$

showing that, at $B \simeq 0$ and up to order $\lambda_{R,D}^2$, the Landau levels are not split due to the SO interaction as one might have naively inferred from Eqs. (2.28). Another merit of the approximate solution is that it displays in a transparent way the interplay between the three spin-dependent interactions, namely the Zeeman, Rashba and Dresselhaus ones. Such interplay has also been discussed in relation with the violation of Larmor's theorem due to the SO coupling [Mal06] and by using the unitarily transformed Hamiltonian technique [Val06]. Note also that in GaAs quantum wells, due to the negative sign of g^* , the lowest energy level is the qup one at energy $E_0^u = \frac{1}{2}\omega_c - \frac{1}{2}\omega_L - 2\lambda_R^2 \omega_c / (\omega_c + \omega_L)$

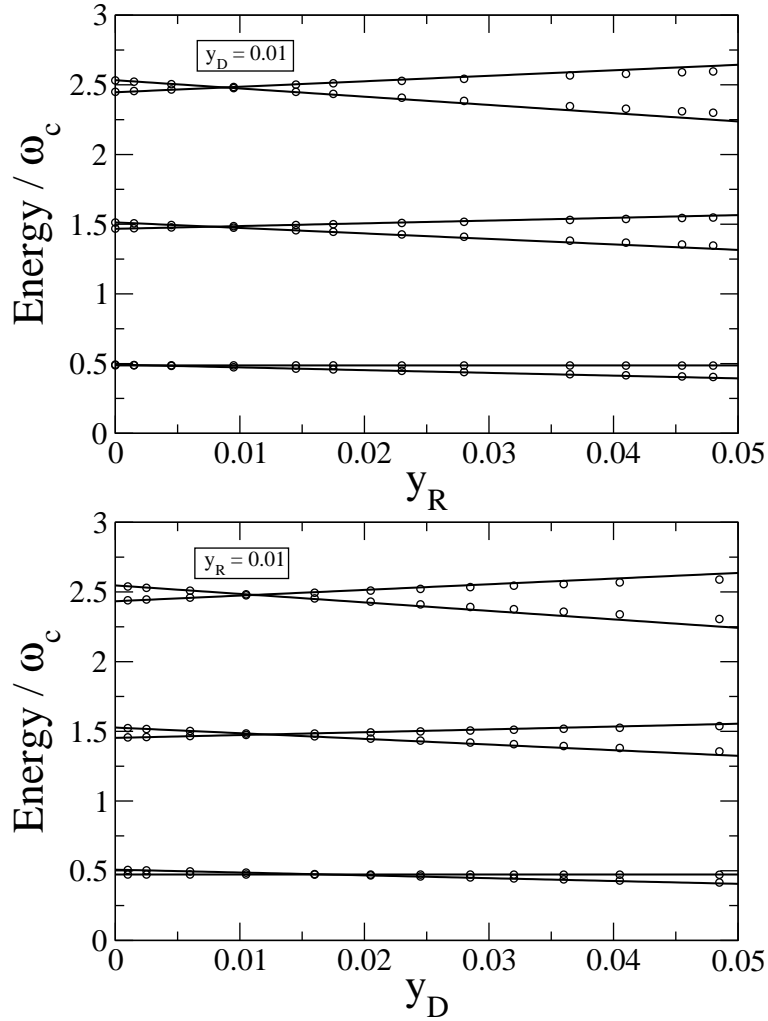


Figure 2.3: Top (bottom) panel: lowest energy levels for a GaAs well as a function of the Rashba (Dresselhaus) intensity $y_R = \lambda_R^2/\omega_c$ ($y_D = \lambda_D^2/\omega_c$) for a fixed Dresselhaus (Rashba) intensity y_D (y_R)=0.01. Solid lines represent the analytical result, Eq. (2.28), while symbols correspond to the exact diagonalization, Eq. (2.31).

containing only the Rashba contribution, whereas the following one corresponds to the qdown state at energy $E_0^d = \frac{1}{2}\omega_c + \frac{1}{2}\omega_L - 2\lambda_D^2\omega_c/(\omega_c - \omega_L)$ involving only the Dresselhaus term. For all the other levels both SO couplings contribute to the energies.

We have assessed the accuracy of Eqs. (2.28) by comparing them with exact numerical results for some particular cases. Indeed, the exact solution to Eqs. (2.7) can be obtained in the truncated space spanned by the lowest \mathcal{N} oscillator levels. Mathematically, this is expressed by the linear eigenvalue problem

$$\mathbf{M} \begin{pmatrix} \mathbf{a} \\ \mathbf{b} \end{pmatrix} = \varepsilon \begin{pmatrix} \mathbf{a} \\ \mathbf{b} \end{pmatrix}, \quad (2.31)$$

where \mathbf{M} is a $2\mathcal{N} \times 2\mathcal{N}$ matrix whereas \mathbf{a} and \mathbf{b} are column vectors made up of the sets of coefficients $\{a_n, n = 0, \dots, \mathcal{N} - 1\}$ and $\{b_n, n = 0, \dots, \mathcal{N} - 1\}$, respectively. We have diagonalized \mathbf{M} using a large enough \mathcal{N} to ensure good convergence in the lowest eigenvalues. Fig. 2.3 displays the comparison between the analytical and the numerical

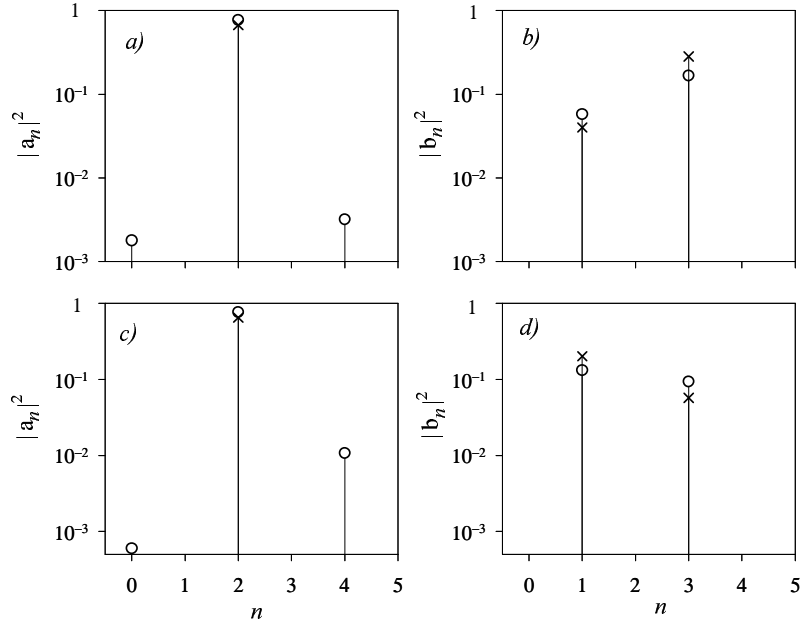


Figure 2.4: Histograms with the amplitudes of a_n and b_n for the rightmost qup state of the third Landau level of Fig. 2.3. Panels a) and b) are for $(y_R = 0.05, y_D = 0.01)$, whereas c) and d) correspond to $(y_R = 0.01, y_D = 0.05)$. Circles (crosses) represent the numerical (analytical) results.

energies as a function of one of the SO strengths while the other is kept fixed at a given value in units of ω_c , namely $y_R \equiv \lambda_R^2/\omega_c$ and $y_D \equiv \lambda_D^2/\omega_c$. The chosen values for y_D and y_R are within the expected range for a GaAs quantum well. For instance, taking $\lambda_{R,D}^2/\hbar^2 \sim 10\mu\text{eV}$ and $B \sim 1\text{T}$, one has $(m\lambda_{R,D}^2/\hbar^2)/(\hbar\omega_c) \sim 10^{-2}$ (we have set $y_{R,D}=0.01$). One can see that there is an excellent agreement between the analytical and the numerical results, with differences starting to be visible only for strong SO intensities and high Landau levels. Actually, the largest value of $y_{R,D} = \lambda_{R,D}^2/\omega_c$ is 0.05, small enough to validate the analytical expression. Notice, however, that for larger $y_{R,D}$ values –not shown in the figure– Eqs. (2.28) no longer reproduce the numerical results. For GaAs this turns out to happen at $B < 0.1\text{ T}$. It can also be seen that for each Landau level both panels show a crossing between the $|n_u\rangle$ state –which is at lower energy for $y_{R,D} \ll 0.01$ because $g^* < 0$ – and the $|n_d\rangle$ state, which eventually lies lower in energy. This crossing is due to the interplay between both spin-orbit couplings.

Fig. 2.4 compares the amplitudes of the qup coefficients a_n and b_n obtained from the numerical diagonalization with those of the analytical result Eq. (2.27). For this purpose, we have chosen the rightmost qup states of the third Landau band in both panels of Fig. 2.3, which are those with the largest SO intensity. Notice that even for these strong spin-orbit couplings the analytical prediction is still excellent since the numerical and analytical amplitudes of a_2 are very close, with only small numerical corrections to a_0 and a_4 . For the b_n coefficients the comparison is also quite good and there are no relevant numerical corrections for n 's different from 1 and 3 –corresponding to b_0 and b_4 . Similar results are found for the qdown states.

2.1.2 Electromagnetic-wave excitations

The preceding results can be used to study the single-particle transitions induced in the system by its interaction with a left-circularly polarized electromagnetic wave propagating along the z -direction, i.e., perpendicular to the plane of motion of the electrons. The vector potential is given by $\mathbf{A}(t) = 2A(\cos\theta\hat{i} + \sin\theta\hat{j})$, with $\theta = \omega t - qz$, and the sp interaction Hamiltonian $h_{int} = \mathbf{J} \cdot \mathbf{A}/c + g^*\mu_B \mathbf{s} \cdot (\nabla \times \mathbf{A})$, with $\mathbf{J} = e\mathbf{v}/\sqrt{\epsilon}$, reads

$$h_{int} = \frac{e}{c\sqrt{\epsilon}}A(v_-e^{i\theta} + v_+e^{-i\theta}) + \frac{1}{2}g^*\mu_BqA(\sigma_-e^{i\theta} + \sigma_+e^{-i\theta}) \quad , \quad (2.32)$$

where the velocity operator is given by $v_{\pm} = -i[x \pm iy, H] = P^{\pm} \pm i\lambda_R\sigma_{\pm} + \lambda_D\sigma_{\mp}$. Defining the operators

$$\alpha^+ \equiv \begin{bmatrix} a^+ & i\tilde{\lambda}_R \\ \tilde{\lambda}_D & a^+ \end{bmatrix} \quad , \quad \alpha^- \equiv \begin{bmatrix} a^- & \tilde{\lambda}_D \\ -i\tilde{\lambda}_R & a^- \end{bmatrix} \quad , \quad (2.33)$$

the Hamiltonian can be rewritten as

$$h_{int} = \frac{e}{c\sqrt{\epsilon}}A\sqrt{2\omega_c}(\alpha^-e^{i\theta} + \alpha^+e^{-i\theta}) + \frac{1}{2}g^*\mu_BqA(\sigma_-e^{i\theta} + \sigma_+e^{-i\theta}) \quad . \quad (2.34)$$

We consider next, within the dipole approximation ($q \approx 0$) and in the absence of Coulomb interaction, several useful examples of single-particle transition matrix elements involving the operators α^+ (proportional to v_+), σ_- , and the qup and qdown states represented by Eqs. (2.22) and (2.25).

For the operator α^+ one can write in general

$$\langle\psi|\alpha^+|\phi\rangle = \psi_1^*a^+\phi_1 + i\tilde{\lambda}_R\psi_1^*\phi_2 + \tilde{\lambda}_D\psi_2^*\phi_1 + \psi_2^*a^+\phi_2 \quad , \quad (2.35)$$

with the possibility to have qup-qup, qdown-qdown, qup-qdown and qdown-qup transitions. The two first ones are related to the usual *cyclotron resonance* and, up to order $\lambda_{R,D}^2$, they are dominated by the transition $n \rightarrow n+1$ at energies $E_{n+1}^d - E_n^d$ and $E_{n+1}^u - E_n^u$ with strengths given by the matrix elements $|\langle(n+1)_u|\alpha^+|n_u\rangle| = |\langle(n+1)_d|\alpha^+|n_d\rangle| = \sqrt{n+1}$. Explicitly,

$$\begin{aligned} E_{CR}^d &= E_{n+1}^d - E_n^d = \omega_c + 2\lambda_R^2\frac{\omega_c}{\omega_c + \omega_L} - 2\lambda_D^2\frac{\omega_c}{\omega_c - \omega_L} \\ E_{CR}^u &= E_{n+1}^u - E_n^u = \omega_c - 2\lambda_R^2\frac{\omega_c}{\omega_c + \omega_L} + 2\lambda_D^2\frac{\omega_c}{\omega_c - \omega_L} . \end{aligned} \quad (2.36)$$

Thus, provided the level with energy E_n^d is occupied, from these expressions one expects a *cyclotron splitting* given by

$$\Delta E_{CR} = |E_{CR}^d - E_{CR}^u| = \left| 4\lambda_R^2\frac{\omega_c}{\omega_c + \omega_L} - 4\lambda_D^2\frac{\omega_c}{\omega_c - \omega_L} \right| \quad . \quad (2.37)$$

The *spin-flip* qdown-qup and qup-qdown transitions are also induced by α^+ , found at energies $E_n^u - E_n^d$ and $E_n^d - E_n^u$ respectively, with strengths $|\langle n_u|\alpha^+|n_d\rangle| = \tilde{\lambda}_R\omega_L/(\omega_c + \omega_L)$

and $|\langle n_d | \alpha^+ | n_u \rangle| = \tilde{\lambda}_D \omega_L / (\omega_c - \omega_L)$. The latter is of particular interest since when $n = 0$ it gives the spin-orbit correction to the *Larmor resonance* [Mal06]:

$$E_L = \omega_L + 2 \left(\lambda_R^2 \frac{\omega_c}{\omega_c + \omega_L} - \lambda_D^2 \frac{\omega_c}{\omega_c - \omega_L} \right) . \quad (2.38)$$

It is worth to note that, since the corresponding transition matrix element is linear in $\tilde{\lambda}_D$, in the presence of Rashba interaction alone the Larmor mode is not excited by α^+ .

For the operator σ_- one gets $\langle \psi | \sigma_- | \phi \rangle = 2\psi_2^* \phi_1$. The dominant transition in this case is the spin-flip one at energy $E_n^d - E_n^u$ with strength $|\langle n_d | \sigma_- | n_u \rangle| = 2$. The qup-qup and qdown-qdown cyclotron resonances are also excited, with strengths $|\langle (n+1)_u | \sigma_- | n_u \rangle| = |\langle (n+1)_d | \sigma_- | n_d \rangle| = 2\tilde{\lambda}_D \sqrt{n+1} \omega_c / (\omega_c - \omega_L)$.

Other excitations that deserve some attention are those induced by the spin-density (or spin-dipole)-type operators $\alpha^+ \sigma_\pm$ and $\alpha^+ \sigma_z$, which can be detected in inelastic light experiments like spin-dipole resonances [Eri99]. The operator $\alpha^+ \sigma_z$ turns out to excite the same cyclotron states as α^+ , i.e., those at energies $E_{n+1}^d - E_n^d$ and $E_{n+1}^u - E_n^u$, with the same transition matrix element $\sqrt{n+1}$. In contrast, the operators $\alpha^+ \sigma_+$ and $\alpha^+ \sigma_-$ mainly induce, respectively, the qdown-qup and qup-qdown excitations with energies $E_{n+1}^u - E_n^d$ and $E_{n+1}^d - E_n^u$, and matrix elements $|\langle (n+1)_u | \alpha^+ \sigma_+ | n_d \rangle| = |\langle (n+1)_d | \alpha^+ \sigma_- | n_u \rangle| = 2\sqrt{n+1}$.

So far, the electron-electron interaction has not been taken into account. Therefore it is natural to ask for the role played by it in the physical processes in which the spin-orbit effects can be important and, thus, have a chance to be experimentally detected. Since we have obtained a spinor basis that includes the SO coupling, namely Eqs. (2.22) and (2.25), one might use it to diagonalize the e-e interaction. This has been done, for example, in Ref. [Cal05], where the spinors Eq. (2.11) are used to study the influence of the Rashba coupling on the incompressible Laughlin state. One could also use this basis to solve the random-phase-approximation equations [Kal84] or to study spin-orbit effects on the collective states of quantum wells within the adiabatic time-dependent local spin-current-density approximation [Mal06, Ser99]. Here we have chosen a different way to incorporate the Coulomb contribution and investigate whether its combination with the SO coupling alters the above-discussed results for the Larmor and cyclotron frequencies. It is the so-called sum-rule approach and, while being more approximate, it is accurate enough and allows one to obtain simple analytical expressions to study the interplay between both interactions in some relevant excitation processes.

We firstly recall that, in the absence of spin-orbit coupling, two important theorems hold involving the full Hamiltonian $H = H_0 + V$, $V = V(\mathbf{r}_{ij})$ being the Coulomb term, and the so-called cyclotron and Larmor operators, given by $\sum_j^N P_j^+$ and $S_- = 1/2 \sum_j^N \sigma_-^j$, respectively. On the one hand, Kohn's theorem

$$[H, \sum_j^N P_j^+] = \omega_c \sum_j^N P_j^+ , \quad (2.39)$$

which tells us that in photoabsorption experiments on quantum wells a narrow peak must appear at the cyclotron energy $\omega = \omega_c$ excited by $\sum_j P_j^+$. This follows from the fact that the electron-electron interaction is invariant under translations and thus commutes with the cyclotron operator:

$$\left[\sum_{i<j}^N V(\mathbf{r}_{ij}), \sum_k^N P_k^+ \right] = 0. \quad (2.40)$$

On the other hand, Larmor's theorem

$$[H, S_-] = \omega_L S_- , \quad (2.41)$$

stating that in ILS experiments at small transferred momentum, or in ESR experiments, a narrow collective state must be excited by S_- at the Larmor frequency $\omega = \omega_L$.

Nevertheless, things radically change when the spin-orbit effects are taken into account. Indeed, one then has

$$[H, \sum_j^N P_j^+] = \omega_c \sum_j^N (P^+ + i\lambda_R \sigma_+ + \lambda_D \sigma_-)_j \quad (2.42)$$

and

$$[H, S_-] = \omega_L S_- + \sum_j^N (2i\lambda_R P^- \sigma_z + 2\lambda_D P^+ \sigma_z)_j . \quad (2.43)$$

It can be clearly seen that the SO interaction couples the charge-density ($\sum_j P_j^+$) and spin-density ($\sum_j P_j^\pm \sigma_z^j$) modes with the spin ($\sigma_{z,\pm}$) ones, thus violating both Kohn's and Larmor's theorems.

We start the approach by introducing the so-called mixed sum rules [Boh79]

$$\begin{aligned} m_k^\pm &= \frac{1}{2} \sum_n \omega_{n0}^k \left(\langle 0|F|\phi_n\rangle \langle \phi_n|G^\dagger|0\rangle \pm \langle 0|G^\dagger|\phi_n\rangle \langle \phi_n|F|0\rangle \right) \\ &= \frac{1}{2} \left(\langle 0|F(H - E_0)^k G^\dagger|0\rangle \pm \langle 0|G^\dagger(H - E_0)^k F|0\rangle \right) , \end{aligned} \quad (2.44)$$

where $|0\rangle$ and $|\phi_n\rangle$ are the ground and n th excited state of H , respectively, and E_0 and ω_{n0} the corresponding energies. Of particular interest [Lip03] are m_0^- , m_1^+ , m_2^- and m_3^+ , which can be expressed in terms of commutators between the operators F , G^\dagger and the Hamiltonian as

$$\begin{aligned} m_0^- &= \frac{1}{2} \langle 0|[F, G^\dagger]|0\rangle \\ m_1^+ &= \frac{1}{2} \langle 0|[F, [H, G^\dagger]]|0\rangle \\ m_2^- &= \frac{1}{2} \langle 0|[[F, H], [H, G^\dagger]]|0\rangle \\ m_3^+ &= \frac{1}{2} \langle 0|[[F, H], [H, [H, G^\dagger]]]|0\rangle . \end{aligned} \quad (2.45)$$

We first consider the case in which the ground state is fully spin-polarized, i.e. $\langle 0|\sum_i \sigma_z^i|0\rangle = N$, and take $F = G = \sum_i P_i^-$ (G^\dagger is therefore the cyclotron operator). The evaluation of

the above commutators then yields, up to order $\lambda_{R,D}^2$:

$$\begin{aligned}
m_0^- &= 2N\omega_c \\
m_1^+ &= 2N\omega_c^2 \\
m_2^- &= 2N\omega_c^3 \left[1 - \frac{2}{\omega_c}(\lambda_R^2 - \lambda_D^2) \right] \\
m_3^+ &= 2N\omega_c^4 \left[1 - \frac{4}{\omega_c}(\lambda_R^2 - \lambda_D^2) + \frac{2\omega_L}{\omega_c^2}(\lambda_R^2 + \lambda_D^2) \right] \quad , \quad (2.46)
\end{aligned}$$

where it has been used Kohn's theorem Eq. (2.39), as well as the commutation relations $[P^-, P^+] = 2\omega_c$, $[\sigma_+, \sigma_-] = 4\sigma_z$ and $[\sigma_z, \sigma_\pm] = \pm 2\sigma_\pm$. It can be easily checked that the first right-hand side of Eq. (2.44), recalling that $\sum_i P_i^- |0\rangle = 0$, reads

$$m_k^\pm = \frac{1}{2} \sum_n \omega_{n0}^k |\langle \phi_n | \sum_i P_i^\pm |0\rangle|^2 \equiv \frac{1}{2} \sum_n \omega_{n0}^k \pi_n . \quad (2.47)$$

Hence, by combining Eqs. 2.46 and 2.47 one can obtain a (nonlinear) system of equations with four unknowns, namely the first two excitation energies ω_{10} , ω_{20} and the respective strengths π_1 , π_2 . In the $\lambda_{R,D}^2/\omega_c \ll 1$ limit, and considering only one of the spin-orbit contributions, the solution is straightforwardly obtained. Indeed, if e.g. $\lambda_R = 0$, one has

$$\begin{aligned}
\omega_{10} &= \omega_c + \frac{2\omega_c}{\omega_c - \omega_L} \lambda_D^2 \\
\omega_{20} &= \omega_L - \frac{2\omega_c}{\omega_c - \omega_L} \lambda_D^2 \\
\pi_1 &= 2N\omega_c \left[1 - \frac{2\omega_c}{(\omega_c - \omega_L)^2} \lambda_D^2 \right] \\
\pi_2 &= 2N \frac{2\omega_c^2}{(\omega_c - \omega_L)^2} \lambda_D^2 \quad . \quad (2.48)
\end{aligned}$$

Clearly, ω_{10} and ω_{20} coincide with Eqs. (2.36) and (2.38), corresponding to the cyclotron and Larmor modes. The $\lambda_D = 0$ case can be worked out in the same way, yielding again total coincidence with the results found without considering the e-e interaction. Alternatively, the above calculations can be carried out using for G^\dagger the Larmor operator, namely $F = G = \sum_i \sigma_+^i$, obtaining the same result.

Of course, the more sum rules are known, the better knowledge of the Hamiltonian spectrum is available. By using also, e.g., m_4^- and m_5^+ one might obtain information on other excited states. We have checked that their consideration yields the same conclusion: neither the cyclotron nor the Larmor modes are affected, up to order $\lambda_{R,D}^2$ and provided that the system is fully spin-polarized, by the Coulomb interaction.

However, when the latter condition is not satisfied, i.e., if the ground-state spin is such that $\langle 0 | \sum_i \sigma_z^i |0\rangle \neq N$, the interplay between the spin-orbit and the electron-electron interactions can introduce new features in the dipole spectrum. The reason is that in this case, even in the absence of SO coupling, the spin-density operator $\sum_i P_i^+ \sigma_z^i$, which does not commute with the Coulomb term $V(\mathbf{r}_{ij})$, excites a mode at energy different

to ω_c . Indeed, an additional peak is expected [Ton04] to be found in experiments at $\omega = \omega_c(1 + \mathcal{K})$, where \mathcal{K} is the correction due to the Coulomb interaction given by

$$\mathcal{K} = \frac{1}{2N\omega_c^2} \langle 0 | \sum_{i < j} \nabla_{\mathbf{r}_{ij}}^2 V(\mathbf{r}_{ij}) (\sigma_z^i - \sigma_z^j)^2 | 0 \rangle . \quad (2.49)$$

Including the spin-orbit coupling, one can consider the mixed m_1^+ sum rule for the operators $F = \sum_i P_i^- \sigma_z^i$ and $G = \sum_i P_i^-$:

$$\begin{aligned} m_1^+ &= \sum_n \omega_{n0} \langle 0 | \sum_i P_i^- \sigma_z^i | \phi_n \rangle \langle \phi_n | \sum_j P_j^+ | 0 \rangle \\ &= \frac{1}{2} \langle 0 | [\sum_i P_i^- \sigma_z^i, [H, \sum_j P_j^+]] | 0 \rangle = \omega_c^2 \langle 0 | \sum_i \sigma_z^i | 0 \rangle . \end{aligned} \quad (2.50)$$

This expression allows one to study the interplay between dipole and spin-dipole modes by splitting it into a sum over spin-density states $|\phi_m\rangle$ and another over charge-density states $|\phi_\rho\rangle$, namely

$$\begin{aligned} m_1^+ &= \sum_\rho \omega_{\rho 0} \langle 0 | \sum_i P_i^- \sigma_z^i | \phi_\rho \rangle \langle \phi_\rho | \sum_j P_j^+ | 0 \rangle \\ &+ \sum_m \omega_{m 0} \langle 0 | \sum_i P_i^- \sigma_z^i | \phi_m \rangle \langle \phi_m | \sum_j P_j^+ | 0 \rangle . \end{aligned} \quad (2.51)$$

As we have seen, due to the SO interaction Kohn's theorem is violated and the cyclotron operator can excite both charge- and spin-density modes. Thus, in general $\langle \phi_m | \sum_i P_i^+ | 0 \rangle \neq 0$ and both contributions in m_1^+ are different from zero. This fact can be inferred from photoabsorption experiments in GaAs quantum wells using unpolarized far-infrared radiation [Man01] where, indeed, a splitting in the cyclotron resonance is found for some configurations of the system, indicating that two modes at different energies are excited. In particular, a well-resolved splitting is observed at the odd filling factors $\nu=3, 5,$ and 7 –recall that $\nu = 2\pi\rho/\omega_c$ with $\nu=0$ for zero-spin systems and satisfying the relation $2S_z/N = 1/\nu$ otherwise–, whereas it turns out to vanish for $\nu = 1$ and for even values of this parameter. Such ν -dependence of the splitting is not predicted by Eq. (2.37); a good explanation for this feature requires the simultaneous consideration of both the Coulomb and the SO interactions.

Within our sum-rule approach, assuming e.g. that only one charge-density state $|\phi_\rho\rangle$ and only one spin-density state $|\phi_m\rangle$ contribute to the respective sums in Eq. (2.51), one can define the mixed strengths

$$\begin{aligned} \tilde{\pi}_1 &= \langle 0 | \sum_i P_i^- \sigma_z^i | \phi_\rho \rangle \langle \phi_\rho | \sum_j P_j^+ | 0 \rangle \\ \tilde{\pi}_2 &= \langle 0 | \sum_i P_i^- \sigma_z^i | \phi_m \rangle \langle \phi_m | \sum_j P_j^+ | 0 \rangle . \end{aligned} \quad (2.52)$$

Evaluating the sum rules m_0^- and m_1^+ for the operators $G = \sum_i P_i^-$ and $F = \sum_i P_i^- \sigma_z^i$, one easily obtains in this case

$$\tilde{\pi}_1 = \omega_c \langle 0 | \sum_i \sigma_z^i | 0 \rangle \frac{E_2 - \omega_c}{E_2 - E_1} = \omega_c \langle 0 | \sum_i \sigma_z^i | 0 \rangle \left(1 - \frac{O(\lambda_{R,D}^2)}{|\omega_c \mathcal{K}|} \right)$$

$$\tilde{\pi}_2 = \omega_c \langle 0 | \sum_i \sigma_z^i | 0 \rangle \frac{\omega_c - E_1}{E_2 - E_1} = \omega_c \langle 0 | \sum_i \sigma_z^i | 0 \rangle \frac{O(\lambda_{R,D}^2)}{|\omega_c \mathcal{K}|} , \quad (2.53)$$

E_1 and E_2 being, respectively, the energies of the states $|\phi_\rho\rangle$ and $|\phi_m\rangle$, and $O(\lambda_{R,D}^2)$ representing the corresponding SO corrections, proportional to $\lambda_{R,D}^2$. From the expression for $\tilde{\pi}_2$ one concludes that, in the presence of spin-orbit coupling and if the system has spin $\langle 0 | \sum_i \sigma_z^i | 0 \rangle$ different from zero –i.e. ν is not even (and neither equal to 1 since we are assuming a non-fully polarized ground state)–, the spin-density state is excited by $\sum_i P_i^+$. In this case the predicted splitting for the cyclotron resonance is given by

$$\Delta E_{CR} = \left| \frac{2S_z}{N} 4 \left(\lambda_R^2 \frac{\omega_c}{\omega_c + \omega_L} - \lambda_D^2 \frac{\omega_c}{\omega_c - \omega_L} \right) + \mathcal{K} \omega_c \right| . \quad (2.54)$$

This is in complete agreement with the above-mentioned experiment and seems to be a clear evidence of crucial spin-orbit effects on a physical observable, as the absence of the latter interaction would imply the vanishment of the described phenomena.

Nevertheless, despite this example a confrontation between theoretical and experimental results on spin-orbit effects is not in general an easy task due to the smallness of the SO interaction and one usually has to satisfy himself with semi-quantitative analysis. To finish this section, we consider a situation that might enhance such effects and that consists in tilting the applied magnetic field, considering e.g. $\mathbf{B} = (B_x, 0, B_z)$. To this end, we have generalized the Landau level energies Eq. (2.28), with the corresponding expressions given in the Appendix A.

For the cyclotron resonance one obtains now

$$\Delta E_{CR} = 4 \left[(C_R \mathcal{V} + C_D \mathcal{Z}) \frac{1}{1 + |g^*| m^* \mathcal{S} / 2} - (C_R \mathcal{Z} + C_D \mathcal{V}) \frac{1}{1 - |g^*| m^* \mathcal{S} / 2} \right] , \quad (2.55)$$

where $C_{R,D} \equiv m \lambda_{R,D}^2 / \hbar^2$ and with the tilting angle θ entering the quantities \mathcal{V} , \mathcal{Z} , and \mathcal{S} , defined in the Appendix. Clearly, tilting effects might arise because of the $1 - |g^*| m^* \mathcal{S} / 2$ denominator in the above equation, but sizeable effects on ΔE_{CR} should only be expected for materials in which $|g^*| m^* / 2$ has a large value. This is not the case for GaAs but it is, e.g., for other semiconductors such as InAs and InSb for which, respectively, $|g^*| m^* / 2 = 0.169$ and 0.355 . For the latter case the dependence of ΔE_{CR} on the in-plane component B_x at fixed B_z is shown in Fig. 2.5. Notice that ΔE_{CR} is sharply increased when B_x exceeds a given value (1T for the chosen parameters), which proves the strong enhancement of the SO effects introduced by the in-plane component of the magnetic field. Also shown in the figure are the exact diagonalization results –see the Appendix. One can see that the analytical expression is very accurate up to rather large tilting angles and for different relative weights of the Rashba and the Dresselhaus terms. As a matter of fact, this analytical result does not depend on B_z although, for the sake of comparison with the exact diagonalization, we have used $B_z = 1$ T. The evolution with B_x is not always monotonous, especially for $C_R > C_D$, where we find an initial decrease of ΔE_{CR} with increasing B_x , vanishing at $B_x \sim 0.8$ T, and eventually increasing again.

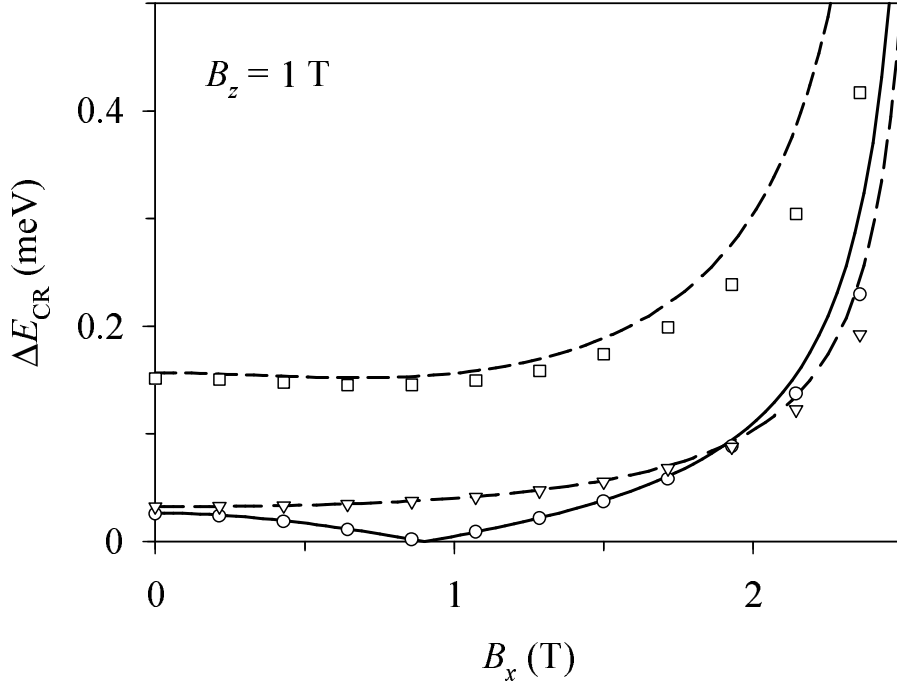


Figure 2.5: Splitting of the cyclotron resonance for an InSb quantum well ($|g^*|m^*/2 = 0.355$) as a function of the in-plane component B_x at fixed $B_z = 1$ T. Lines (symbols) represent the analytical (numerical) results. The shown results are for $(C_R = 30 \mu\text{eV}, C_D = 10 \mu\text{eV})$ (solid line and circles), $(C_R = 10 \mu\text{eV}, C_D = 10 \mu\text{eV})$ (long-dashed line and triangles) and $(C_R = 10 \mu\text{eV}, C_D = 30 \mu\text{eV})$ (short-dashed line and squares).

2.2 Exchange-correlation effects in quantum wires submitted to in-plane magnetic fields

Among semiconductor nanostructures, quantum wires (QWs) are especially well-suited for the potential development of spintronic devices. On the one hand, their transverse length can be externally controlled, making the system more or less quasi-one-dimensional and hence changing the ratio of the SO strength to the confinement. On the other hand, the electron motion can be rendered almost collisionless because of the high purity of the starting quasi-two-dimensional electron gas.

The energy subband structure and conductance (G) of quantum wires including spin-orbit effects have been addressed by several authors, mostly considering only the Rashba coupling [Gov02, Mir01, Mor99] because of its possibility to be externally tuned. Also, the effects of applied magnetic fields, either in or perpendicular to the plane containing the QW have been considered in combination with only the Rashba [Deb05, Kno05, Ser05] or both [Zha06] SO interactions. Interesting features of the energy subbands and G have been disclosed, especially for strong spin-orbit couplings and with magnetic fields applied to the QW. Among them, the presence of anticrossings, asymmetries, local extrema and energy gaps in the subband spectra, or the so-called ‘anomalous plateaus’ in the conductance are some of the most interesting. By the latter are meant those plateaus –or steps–

appearing in the conductance that do not follow the increasing sequence in units of the fundamental unit $G_0 \equiv 2e^2/h$, pertaining to the Landauer formula. The importance of including the Rashba intersubband coupling term, neglected in some works, has also been pointed out [Ser05].

Nevertheless, in the above-mentioned works the electron-electron interaction has not been taken into account. It is thus worth to elucidate to which extent the above-mentioned results change when it is considered, at least in a workable and sound mean-field approximation. We study here the exchange-correlation effects –omitting the Hartree term as explained below– on the energy subband structure and on the conductance of quantum wires submitted to an in-plane magnetic field and with both Rashba and Dresselhaus couplings. The first step is to introduce a generalization of the Local Spin-Density Approximation –which as shown below is not valid when the SO interaction is taken into account– to address the problem.

2.2.1 Noncollinear LSDA

As we have seen when addressing quantum wells, in the presence of spin-orbit coupling the states of the system are described by two-component spinors

$$\Psi_i(\mathbf{r}) \equiv |\Psi_i\rangle \equiv \begin{pmatrix} \varphi_i(\mathbf{r}, \uparrow) \\ \varphi_i(\mathbf{r}, \downarrow) \end{pmatrix}, \quad (2.56)$$

where i represents the set of quantum labels and \uparrow, \downarrow refers to the up and down components. The spin orientation at a given point can be calculated from the spin magnetization vector, which is given by

$$m_a(\mathbf{r}) = \sum_i \langle \Psi_i | \delta(\mathbf{r}_j - \mathbf{r}) \sigma_a | \Psi_i \rangle_{\mathbf{r}_j} f_\mu(\varepsilon_i), \quad (2.57)$$

with $a=x, y$ and z , and where $f_\mu(\varepsilon_i) = (1 + e^{(\varepsilon_i - \mu)/k_B T})^{-1}$ is the Fermi-Dirac distribution function giving the occupation of the i th state at a given temperature T and chemical potential μ . This yields

$$\begin{aligned} m_x(\mathbf{r}) &= \sum_i 2\text{Re} [\varphi_i(\mathbf{r}, \uparrow)^* \varphi_i(\mathbf{r}, \downarrow)] f_\mu(\varepsilon_i) \\ m_y(\mathbf{r}) &= \sum_i 2\text{Im} [\varphi_i(\mathbf{r}, \uparrow)^* \varphi_i(\mathbf{r}, \downarrow)] f_\mu(\varepsilon_i) \\ m_z(\mathbf{r}) &= \sum_i [|\varphi_i(\mathbf{r}, \uparrow)|^2 - |\varphi_i(\mathbf{r}, \downarrow)|^2] f_\mu(\varepsilon_i). \end{aligned} \quad (2.58)$$

One thus can see that, in general, the spin orientation is different from one point of the system to another and depends as well on the quantum numbers representing the spinors. In this situation, the spins are said to be noncollinear and one is not able to employ the LSDA relations introduced in section 1.1.1, where it was assumed from the beginning a uniformly spin-polarized system taking as common magnetization direction

the z -axis. Fortunately, there exists a generalization of the theory valid for such scenarios: the so-called *Noncollinear Local Spin-Density Approximation*.

The underlying idea of this approach is that the LSDA is extended to *locally* treat the spin orientation exactly as in the uniformly-magnetized system. In the noncollinear case one has to deal with the general non-diagonal density matrix

$$\rho_{\eta\eta'}(\mathbf{r}) = \sum_i \varphi_i^*(\mathbf{r}, \eta) \varphi_i(\mathbf{r}, \eta') f_\mu(\varepsilon_i) \Rightarrow \begin{pmatrix} \rho_{\uparrow\uparrow} & \rho_{\uparrow\downarrow} \\ \rho_{\downarrow\uparrow} & \rho_{\downarrow\downarrow} \end{pmatrix}, \quad (2.59)$$

where $\eta, \eta' = \uparrow, \downarrow$, and which can be rewritten as

$$\begin{pmatrix} \rho_{\uparrow\uparrow} & \rho_{\uparrow\downarrow} \\ \rho_{\downarrow\uparrow} & \rho_{\downarrow\downarrow} \end{pmatrix} = \frac{1}{2} \begin{pmatrix} \rho + m_z & m_x + im_y \\ m_x - im_y & \rho - m_z \end{pmatrix}, \quad (2.60)$$

ρ being the usual electron density, given by

$$\begin{aligned} \rho(\mathbf{r}) &= \sum_i \langle \Psi_i | \delta(\mathbf{r}_j - \mathbf{r}) | \Psi_i \rangle_{\mathbf{r}_j} f_\mu(\varepsilon_i) \\ &= \sum_i [|\varphi_i(\mathbf{r}, \uparrow)|^2 + |\varphi_i(\mathbf{r}, \downarrow)|^2] f_\mu(\varepsilon_i). \end{aligned} \quad (2.61)$$

This gives rise to the non-diagonal exchange-correlation matrix

$$V_{xc}^{\eta\eta'}(\mathbf{r}) \equiv \frac{\delta E_{xc}[\rho_{\eta\eta'}(\mathbf{r})]}{\delta \rho_{\eta\eta'}(\mathbf{r})}. \quad (2.62)$$

In this case, this expression cannot be directly evaluated since the explicit form for E_{xc} is unknown. However, one can define [Hei99], at each point, a diagonal density matrix by means of a local unitary transformation U

$$U \rho U^+ = n \equiv \begin{pmatrix} n_\uparrow & 0 \\ 0 & n_\downarrow \end{pmatrix}, \quad (2.63)$$

where the local rotation is given by

$$U = \begin{pmatrix} e^{i\phi(\mathbf{r})/2} \cos \frac{\theta(\mathbf{r})}{2} & e^{-i\phi(\mathbf{r})/2} \sin \frac{\theta(\mathbf{r})}{2} \\ -e^{i\phi(\mathbf{r})/2} \sin \frac{\theta(\mathbf{r})}{2} & e^{-i\phi(\mathbf{r})/2} \cos \frac{\theta(\mathbf{r})}{2} \end{pmatrix}, \quad (2.64)$$

and where the angles θ and ϕ give the spin orientation at the considered point and are determined from the relations

$$\begin{aligned} \tan \phi(\mathbf{r}) &= -\frac{m_y(\mathbf{r})}{m_x(\mathbf{r})} \\ \tan \theta(\mathbf{r}) &= \frac{\sqrt{m_x^2(\mathbf{r}) + m_y^2(\mathbf{r})}}{m_z(\mathbf{r})}. \end{aligned} \quad (2.65)$$

Omitting the arguments, the diagonal local densities read

$$\begin{aligned} n_\uparrow &= \frac{1}{2}(\rho + m_z \cos \theta) + \text{Re} \{ \rho_{\uparrow\downarrow} e^{i\phi} \sin \theta \} \\ n_\downarrow &= \frac{1}{2}(\rho - m_z \cos \theta) - \text{Re} \{ \rho_{\uparrow\downarrow} e^{i\phi} \sin \theta \}. \end{aligned} \quad (2.66)$$

Hence, knowing n_\uparrow and n_\downarrow at a point \mathbf{r} , we can use the familiar relations of the LSDA to compute the exchange-correlation potentials

$$v(\mathbf{r}) \equiv \begin{pmatrix} v_\uparrow & 0 \\ 0 & v_\downarrow \end{pmatrix} \equiv \begin{pmatrix} \delta E_{xc}^{LSDA}[n_\uparrow, n_\downarrow]/\delta n_\uparrow & 0 \\ 0 & \delta E_{xc}^{LSDA}[n_\uparrow, n_\downarrow]/\delta n_\downarrow \end{pmatrix}. \quad (2.67)$$

Finally, one just needs to undo the rotation and the resulting expression for the exchange-correlation potential reads

$$V_{xc}^{\eta\eta'}(\mathbf{r}) \equiv \begin{pmatrix} v_0 + \Delta v \cos \theta & \Delta v e^{-i\phi} \sin \theta \\ \Delta v e^{i\phi} \sin \theta & v_0 - \Delta v \cos \theta \end{pmatrix}, \quad (2.68)$$

where we have defined $v_0 \equiv (v_\uparrow + v_\downarrow)/2$ and $\Delta v \equiv (v_\uparrow - v_\downarrow)/2$. This scheme fully determines the 2×2 potential matrix V_{xc} in terms of the spinor orbitals and the LSDA energy functional.

2.2.2 Subband structure

We consider a two-dimensional quantum wire of length L described by a parabolic confinement in the y -direction, namely $V_{conf}(y) = \frac{1}{2}\omega_0^2 y^2$. Since the electrons move freely along the x -axis, the Kohn-Sham two-component spinors Eq. (2.56) can be written as

$$\Psi_{nk}(\mathbf{r}) \equiv |\Psi_{nk}\rangle \equiv \frac{1}{\sqrt{L}} \begin{pmatrix} \varphi_{nk}(y, \uparrow) \\ \varphi_{nk}(y, \downarrow) \end{pmatrix} e^{ikx}, \quad (2.69)$$

where k is a continuous wave number due to the translational invariance along the longitudinal axis of the wire and the index $n = 1, 2, 3, \dots$ labels the different energy subbands as usual. Therefore, the quantum numbers are n and k , and the Kohn-Sham equations read in the spinorial form

$$h_{KS}[\rho, \mathbf{m}]|\Psi_{nk}\rangle = \varepsilon_{nk}|\Psi_{nk}\rangle. \quad (2.70)$$

We have solved them for each n and k , keeping the lowest n_{\max} eigenvalues and eigenvectors $\{\varepsilon_{nk}, \Psi_{nk}(\mathbf{r})\}$. To do so, we have introduced a y -discretization from $-y_{max}$ to $+y_{max}$. This defines N_y points and, since the two spinor components are coupled, the resulting matrix is $2N_y \times 2N_y$. For N_y 's of the order of 100, the diagonalization is extremely fast and, although it is repeated $N_k \times n_{max}$ times per iteration, the calculation is quite efficient. The KS Hamiltonian has been split into three different pieces, namely $h_{KS} = h_0 + h_{SO} + h_Z$, consisting of the kinetic plus confining plus exchange-correlation term, the Rashba plus Dresselhaus SO contribution, and the Zeeman one arising from the in-plane magnetic field

$$\mathbf{B} = B(\cos \phi_B \mathbf{u}_x + \sin \phi_B \mathbf{u}_y), \quad (2.71)$$

ϕ_B being the azimuthal angle. The extension to include a vertical magnetic field can be easily done but it is not addressed here. Explicitly, one has

$$h_0 = \frac{p_x^2 + p_y^2}{2m} + \frac{1}{2}m\omega_0^2 y^2 + V_{xc}^{\eta\eta'}(y)$$

$$\begin{aligned} h_{SO} &= h_R + h_D \\ h_Z &= \mathcal{E}_z(\sigma_x \cos \phi_B + \sigma_y \sin \phi_B) . \end{aligned} \quad (2.72)$$

where $\mathcal{E}_Z = g^* \mu_B B$ is the Zeeman energy. Note that, since \mathbf{B} is in-plane, p_x and p_y are the actual components of the linear momentum of the electron, and not those of the generalized momentum involving the vector potential. To simplify the calculations, we have introduced a complex SO coupling parameter, namely $\gamma \equiv \lambda_D + i\lambda_R$, that allows one to write the SO Hamiltonian as

$$h_R + h_D = \begin{pmatrix} 0 & \gamma k + \gamma^* \frac{d}{dy} \\ \gamma^* k - \gamma \frac{d}{dy} & 0 \end{pmatrix} . \quad (2.73)$$

Notice that in the above expressions the direct Coulomb interaction has been omitted. In principle one should also include a Hartree term [Gud95, Mal05] but we have considered it to be exactly cancelled out by some neutralizing background contribution –within the so-called *full-screening approximation* [Rei99]. The inclusion of this term would introduce some uncertainties in the model, as its actual expression would depend on the way the positive charges are distributed to cancel out the divergence in the Hartree potential. To be definite, the screened transverse potential has been assumed to be parabolic though other potentials such as a square well would have yielded a qualitatively similar behavior.

The QW is characterized [Mal05] by the one-dimensional electronic density ρ_{1D} , defined as

$$\rho_{1D} \equiv \int dy \rho(y) . \quad (2.74)$$

As a matter of fact, the translational invariance along the wire implies that not only the density but all the physical variables of the system depend only on y .

To carry out the k -integrations we have discretized the integrals in a $[k_{min}, k_{max}]$ interval, and have computed Ψ_{nk} for the chosen states on a k -grid with N_k points, for all the n 's up to a chosen n_{max} . Next, we have performed the integrations using a high-precision method –a Bode rule– in the k -domain [Abr72]. Moreover, to avoid the cumbersome evaluation of the band occupations at zero temperature, we have used a finite- T formalism though it can be viewed just as a numerical trick since we have chosen a temperature small enough so that ours are in practice $T = 0$ results. Thermal effects might be introduced increasing the value of T in the relevant expressions, but we have not considered this possibility here. It must also be pointed out that, contrarily to the noninteracting situation, in which for a given set of parameters defining the QW its energy subbands are determined once for all and can be filled with electrons until reaching a prefixed value for ρ_{1D} or μ , in the present case the subband structure is selfconsistently determined and therefore it generally changes from a value of the linear density to another.

At given ρ_{1D} , the total energy per unit length

$$E_{total} = E_{kin} + E_{conf} + E_{SO} + E_{xc} + E_Z = \int dy \sum_n \frac{L}{2\pi} \int dk \langle \Psi_{nk} | h_{ks} | \Psi_{nk} \rangle \quad (2.75)$$

is calculated piece by piece. Defining $\varphi_{nk\eta} \equiv \varphi_{nk}(y, \eta)$, for the kinetic and confining terms one has

$$E_{kin} = \frac{1}{4\pi} \int dy \sum_n \int dk \left\{ |\varphi'_{nk\uparrow}|^2 + |\varphi'_{nk\downarrow}|^2 + k^2 (|\varphi_{nk\uparrow}|^2 + |\varphi_{nk\downarrow}|^2) \right\} f_\mu(\varepsilon_{nk}) \quad (2.76)$$

$$E_{conf} = \frac{\omega_0^2}{4\pi} \int dy \sum_n \int dk y^2 (|\varphi_{nk\uparrow}|^2 + |\varphi_{nk\downarrow}|^2) f_\mu(\varepsilon_{nk}), \quad (2.77)$$

with $\varphi'_{nk\eta} \equiv d\varphi_{nk\eta}/dy$. For the SO contribution, using Eq. (2.73) one obtains

$$E_{SO} = \int dy \sum_n \frac{1}{2\pi} \int dk \begin{pmatrix} \varphi_{nk\uparrow}^* & \varphi_{nk\downarrow}^* \end{pmatrix} \begin{pmatrix} 0 & \gamma k + \gamma^* \frac{d}{dy} \\ \gamma^* k - \gamma \frac{d}{dy} & 0 \end{pmatrix} \begin{pmatrix} \varphi_{nk\uparrow} \\ \varphi_{nk\downarrow} \end{pmatrix} f_\mu(\varepsilon_{nk}). \quad (2.78)$$

Performing the matrix multiplications one gets an expression that is apparently real

$$E_{SO} = \int dy \sum_n \frac{1}{2\pi} \int dk \left\{ 2k \operatorname{Re} [\gamma^* \varphi_{nk\downarrow}^* \varphi_{nk\uparrow}] + \operatorname{Re} [\gamma (\varphi_{nk\downarrow}'^* \varphi_{nk\uparrow} - \varphi_{nk\downarrow}^* \varphi_{nk\uparrow}')] \right\} f_\mu(\varepsilon_{nk}), \quad (2.79)$$

where it has been used that

$$\int dy \varphi_{nk\uparrow}^* \varphi_{nk\downarrow}' = \frac{1}{2} \int dy (\varphi_{nk\uparrow}^* \varphi_{nk\downarrow}' - \varphi_{nk\uparrow}'^* \varphi_{nk\downarrow}). \quad (2.80)$$

Finally, one has the Zeeman and exchange-correlation contributions, respectively given by

$$E_Z = \mathcal{E}_Z \int dy \sum_n \frac{1}{2\pi} \int dk 2 \left\{ \cos \phi_B \operatorname{Re} [\varphi_{nk\downarrow}^* \varphi_{nk\uparrow}] - \sin \phi_B \operatorname{Im} [\varphi_{nk\downarrow}^* \varphi_{nk\uparrow}] \right\} f_\mu(\varepsilon_{nk}), \quad (2.81)$$

and

$$E_{xc} = \int dy \varepsilon_{xc}(y) \rho(y). \quad (2.82)$$

The spin-orbit regime is represented by the ratio of the SO to the confining energy, namely

$$\Delta_{R,D} = \frac{m\lambda_{R,D}^2}{2\hbar^3\omega_0}, \quad (2.83)$$

and we have used the values ($\Delta_R = 0.0037$, $\Delta_D = 0.015$) and ($\Delta_R = 0.093$, $\Delta_D = 0.37$) to characterize, respectively, typical weak and strong SO coupling regimes [Zha06]. The results we discuss in the following have been obtained using these values, except when others are explicitly given.

The intensity of the magnetic field, when different from zero, has been set to $B = 20$ T, and only two orientation angles have been considered, namely $\phi_B = 0$ and $\pi/2$. To present the results, we have used the harmonic oscillator length $l_0 = \sqrt{\hbar/m\omega_0}$ to express both the linear density ρ_{1D} and the wave number k in units of l_0^{-1} . For a typical energy value $\hbar\omega_0 = 4$ meV, a unit linear density $\rho_{1D} = l_0^{-1}$ is about 5.9×10^5 cm $^{-1}$ and the interaction-to-confinement ratio $e^2/(\epsilon l_0 \hbar\omega_0)$ is 1.72 for a GaAs quantum wire.

Fig. 2.6 shows the energy per electron E/N at $B = 0$ as a function of ρ_{1D} in the weak and strong SO coupling regimes. Due to the exchange-correlation interaction E/N

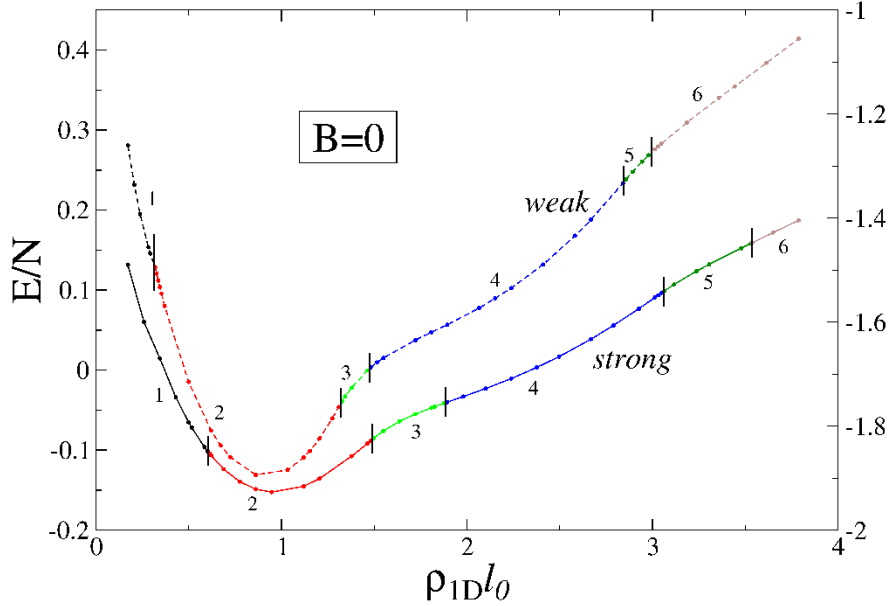


Figure 2.6: Energy per electron (in $\hbar\omega_0$ units) as a function of ρ_{1D} at $B = 0$. The regions separated by vertical lines are characterized by the indicated number of *distinct* subbands crossed by the electron chemical potential μ , i.e., partially occupied subbands. The vertical left (right) scale corresponds to the weak (strong) SO regime.

is not a monotonous function of the linear density [Mal05], and neither is the chemical potential.

We have studied the effects of V_{xc} in several situations involving in-plane magnetic fields and different strengths of the spin-orbit interaction, having found it difficult to be systematized since it depends on the actual value of the system parameters, namely ρ_{1D} , the orientation of the applied field \mathbf{B} , and also on the intensity of the SO coupling. In general, though, the exchange-correlation interaction seems to have a tendency to enhance or modify the effects of the magnetic field, especially at low densities. Indeed, we have found that, for some low-density configurations, the subband structure at $\mathbf{B} = 0$ when V_{xc} is taken into account turns out to be qualitatively the same as when a certain magnetic field is applied and V_{xc} is set to zero. The spontaneous symmetry breaking leading to the appearance of a magnetization is made possible by the exchange-correlation energy, which in some cases attains its minimal value when the system is spin-polarized even at $\mathbf{B} = 0$. Therefore, one can physically ascribe this resulting magnetization to an *exchange-correlation-induced magnetic field*, ‘ $\mathbf{B}_{V_{xc}}$ ’. Analogously, when $\mathbf{B} \neq 0$ V_{xc} may give rise to an effective field $\mathbf{B}_{effective} = \mathbf{B} + \mathbf{B}_{V_{xc}}$ with an orientation equal or different from that of \mathbf{B} .

Since in many previous works only the Rashba SO interaction has been taken into account, it is pertinent to begin with the discussion of the effects of V_{xc} in the $\Delta_D = 0$ situation. Fig. 2.7 shows the results corresponding to a low-density QW for $B = 20$ T and $\phi_B = 0$ in a strong SO regime, namely $\Delta_R = 0.37$. One may see that when $V_{xc} = 0$ the first subband presents the characteristic symmetric double-minimum shape of this case

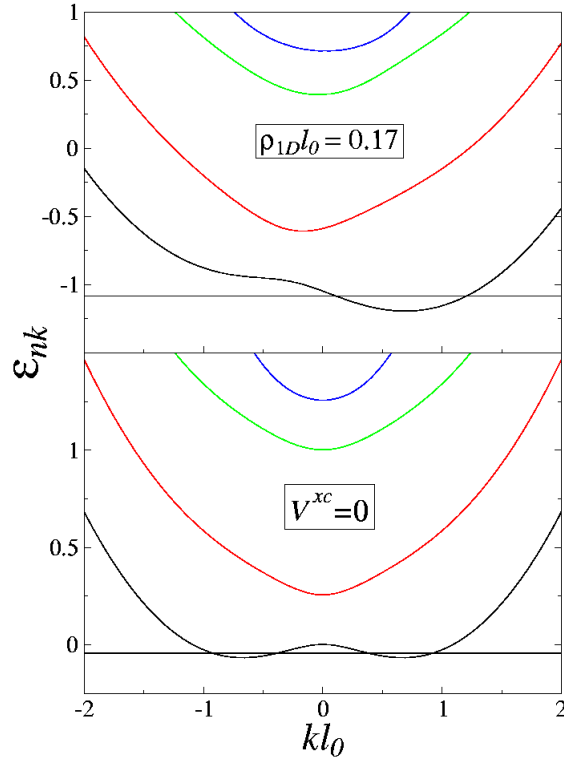


Figure 2.7: Sp energies (in $\hbar\omega_0$ units) for $\rho_{1D}l_0 = 0.17$ and $B = 20$ T, $\phi_B = 0$ and $\Delta_R = 0.37$, $\Delta_D = 0$ (strong SO regime) as a function of kl_0 . The thin horizontal line represents the chemical potential.

[Per04, Ser05]. The effect of V_{xc} at such low density is to induce an asymmetry in the lowest subbands, transforming this symmetric double-minimum structure into another one rather similar to that corresponding to the situation in which $V_{xc} = 0$ and $\phi_B = \pi/4$ [Per04], i.e., the exchange-correlation interaction modifies the direction of the applied field. It must be pointed out that, for small Δ_R values, the double minimum is not found even when $V_{xc} = 0$, whereas in a very strong regime, e.g. $\Delta_R = 0.83$, such structure is also present for odd- $n > 1$ values. In this case, the changes induced by V_{xc} are qualitatively similar to those displayed in the figure.

Likely, the absence of a common spin quantization axis due to the presence of SO coupling has much to do with the complex effect of V_{xc} on the subband structure, which may give rise to the presence of spin textures across the wire [Ser05] that can be calculated from the relations (2.58). This is illustrated in Fig. 2.8, corresponding to the situation shown in Fig. 2.7 comparing the situations in which V_{xc} is and is not taken into account. In both panels, the z -component displays the previously found [Gov02, Ser05] spin accumulations of different sign on opposite lateral sides of the wire, indicating the robustness of this effect against V_{xc} . On the contrary, the in-plane spin distributions show remarkable differences between both situations: at $V_{xc} = 0$ it is perfectly aligned along the direction of the magnetic field ($\phi_B = 0$) whereas it deviates pointing along the $\phi_B \approx \pi/4$ direction when V_{xc} is included. This result nicely illustrates the above-mentioned property of V_{xc} that amounts to replace the applied magnetic field by an effective one having different

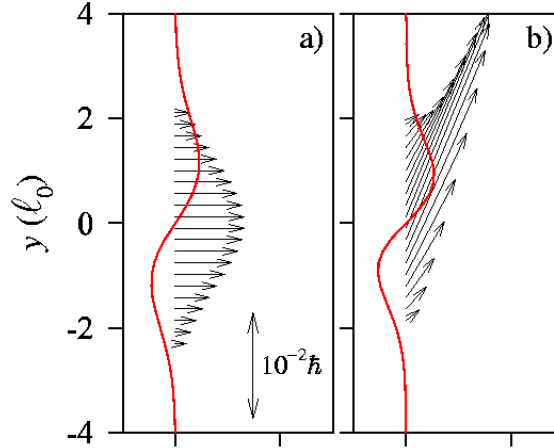


Figure 2.8: Spin textures across the wire (y -direction, in l_0 units) corresponding to the situation displayed in Fig. 2.7. The left panel corresponds to the $V_{xc} = 0$ case. The vector plot shows the in-plane spin, and the solid red line corresponds to the z -component. The spin scale is indicated in panel a).

modulus and direction.

Exchange-correlation effects also appear when both SO contributions are taken into account. Fig. 2.9 shows the energy subband structure for the strong coupling regime and magnetic field with $\phi_B = \pi/2$. In both panels, conspicuous subband gaps and local extrema appear near $k = 0$. The most interesting feature in this case is the weak local maximum at $k > 0$ in even subbands when V_{xc} is not considered (bottom panel). Similar structures have been found in Ref. [Mor99], where the $B = 0$ case is addressed considering only the Rashba SO interaction. One can see that the inclusion of V_{xc} washes out these structures. On the other hand, the well-known [Per04, Ser05] local extrema present in the odd bands remain qualitatively unaffected by the inclusion of the exchange-correlation interaction. These features have important effects on the conductance, as we shall see in the next section.

Finally, the sp energies for a situation corresponding to $B=0$ and a relatively low density are shown in Fig. 2.10, again in the strong SO regime. It can be seen that V_{xc} gives rise to a symmetric subband structure with an energy gap at $k=0$, characteristic of the situation represented in the bottom panel of Fig. 2.7 (in which there is an applied magnetic field). Once more, this exemplifies the **B**-like behavior of V_{xc} .

The spin textures corresponding to the results with $V_{xc} \neq 0$ of Figs. 2.9 and 2.10 are shown in the left and right panels of Fig. 2.11, respectively. The left-panel results correspond to a magnetic field along the positive y -axis that is clearly constraining the in-plane magnetization to essentially point along this direction. However, some straggling of the arrows around the vertical direction persists. As in Fig. 2.8, the z -component displays different sign accumulations on opposite edges of the wire that, when combined with the in-plane distribution, yield a rather complicated spin texturing. The right panel in Fig. 2.11 corresponds to a case with $B = 0$. Hence, in this situation there is no *a priori*

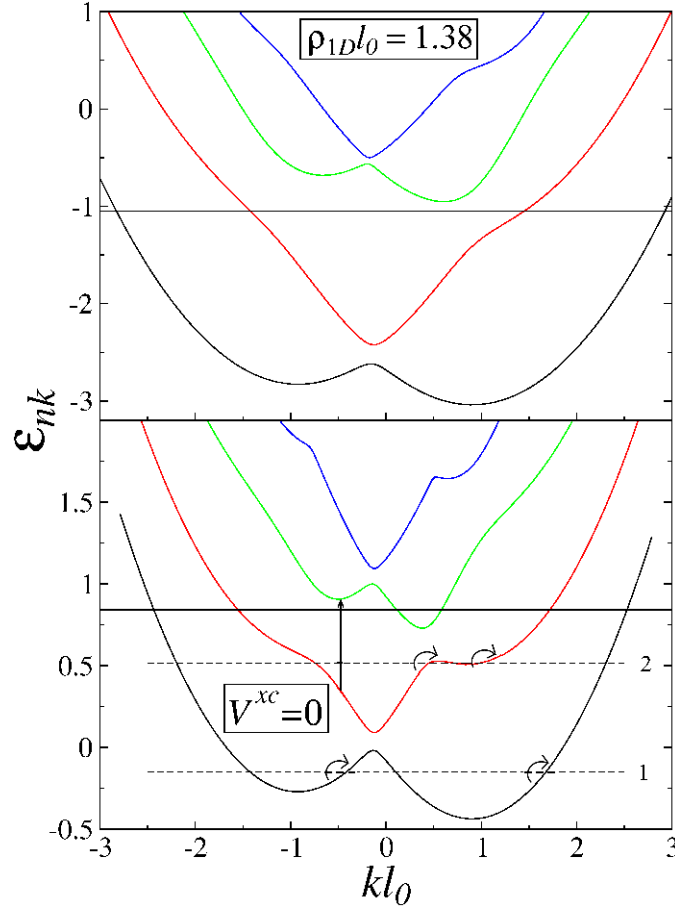


Figure 2.9: Sp energies (in $\hbar\omega_0$ units) for $\rho_{1D}l_0 = 1.38$ and $B = 20$ T, $\phi_B = \pi/2$, in a strong SO regime characterized by $\Delta_R = 0.093$, $\Delta_D = 0.37$, as a function of kl_0 . In both panels, the thin horizontal line represents the chemical potential for the linear density $\rho_{1D}l_0 = 1.38$, whereas the dashed horizontal lines in the bottom panel represent the chemical potential for two smaller linear densities that will be used in the discussion of the conductance in the next section, where the meaning of the arrows displayed in the figure is explained.

preferred direction and the fact that the in-plane spin magnetization selects a certain one is an example of spontaneous symmetry breaking induced by V_{xc} .

It is worth to mention that exchange-correlation effects are also found in the weak SO coupling regime, though in this case no local extrema are found. However, we show in the next section that the effects of V_{xc} on the conductance are also visible in this situation, especially marked at low densities and becoming notably weaker or disappearing for $n \geq 2$, in which case only small k -asymmetries are observed in odd subbands at $B = 0$. When an in-plane magnetic field already acts on the wire, V_{xc} seems to slightly enhance the effects of \mathbf{B} without producing qualitative changes in the subband structure.

To finish this section, we point out that a particular situation appears when $\lambda_D = \lambda_R$ at zero magnetic field. It has already been addressed at $V_{xc} = 0$ [Sch03b] showing that the subband anticrossings disappear when both SO strengths are equal. We have found that the inclusion of the exchange-correlation interaction does not alter this property in any SO regime.

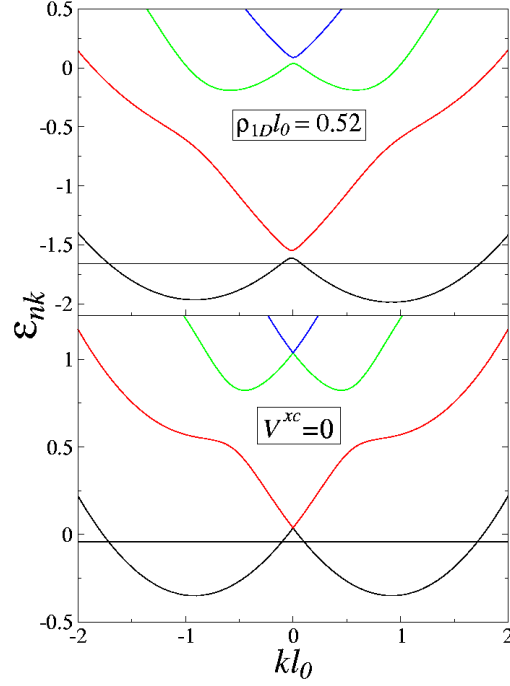


Figure 2.10: Sp energies (in $\hbar\omega_0$ units) for $\rho_{1D}l_0 = 0.52$ and $B = 0$ in a strong SO regime with $\Delta_R = 0.093$, $\Delta_D = 0.37$, as a function of kl_0 .

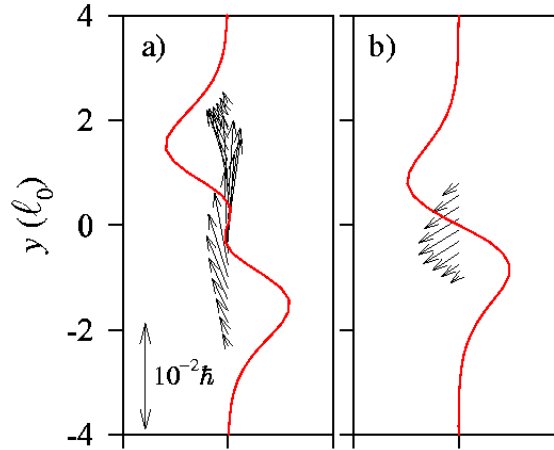


Figure 2.11: Same as Fig. 2.8 for the situations displayed in Fig. 2.9 (left panel) and Fig. 2.10 (right panel) with $V_{xc} \neq 0$.

2.2.3 Conductance

The noncollinear Kohn-Sham calculation discussed in the previous section allows one to evaluate the free -KS (mean-field)- linear density response $\chi_0(q, \omega)$ to a field parallel to the wire -i.e. in the x -direction-, which is given by:

$$\frac{\chi_0(q, \omega)}{L} = \frac{1}{\pi} \sum_n \int dk \frac{\epsilon_{nk,q} |\langle \Psi_{nk+q} | e^{iqx} | \Psi_{nk} \rangle|^2}{(\omega + i\lambda)^2 - \epsilon_{nk,q}^2}, \quad (2.84)$$

where λ is a small real quantity and it is important to notice that the sum runs over all the possible *intrasubband* ($\Delta n = 0$) excitations with energy $\epsilon_{nk,q}$ induced in the ground

state by the density operator $\sum_j e^{iqx_j}$. The longitudinal conductivity associated to $\frac{\chi_0(q, \omega)}{L}$ is given by [Lip03, Pin66]

$$\frac{\sigma(\omega)}{L} = i \frac{e^2 \omega}{q^2} \frac{\chi_0(q, \omega)}{L}, \quad (2.85)$$

whose real part satisfies the relation

$$\text{Re} \left[\frac{\sigma(\omega)}{L} \right] = -\frac{e^2 \omega}{q^2} \text{Im} \frac{\chi_0(q, \omega)}{L}. \quad (2.86)$$

The conductance G is defined as the $q \rightarrow 0$ and $\omega \rightarrow 0$ limits of the above expression. When $q \rightarrow 0$, the operator $\sum_j e^{iqx_j}$ induces intrasubband excitations between the states $|\Psi_{nk}\rangle$ and $|\Psi_{nk+q}\rangle$ with energy

$$\epsilon_{nk,q} = \epsilon_{nk+q} - \epsilon_{nk} = q \left. \frac{\partial \epsilon_{nk}}{\partial k} \right|_{k=k_n} \equiv \alpha_{k_n} q, \quad (2.87)$$

where k_n are the intersections of the n th subband with the chemical potential corresponding to *positive slopes* α_{k_n} . Indeed, it is crucial to realize that for $q > 0$ only intrasubband excitations with $k+q > k$ are allowed. They are gapless and exist due to the confinement in the QW, which breaks the translational invariance of the system along the y -direction and bends the single-particle subbands. Notice that for the energy subband patterns generated in the previous section also intersubband ($\Delta n \neq 0$) electron-hole excitations could be induced. As shown above, though, they do not contribute to the xx DC conductivity of the wire. The bottom panel of Fig. 2.9 displays examples of both kinds of excitations, the intrasubband and intersubband excitations being represented, respectively, by curved and straight arrows.

Since

$$\begin{aligned} \langle \Psi_{nk+q} | e^{iqx} | \Psi_{nk} \rangle &= \int d\mathbf{r} \Psi_{nk+q}^\dagger(\mathbf{r}) e^{iqx} \Psi_{nk}(\mathbf{r}) \\ &= \frac{1}{L} \sum_\eta \int \int dx dy \varphi_{nk+q}^*(y, \eta) e^{-i(k+q)x} e^{iqx} \varphi_{nk}(y, \eta) e^{ikx} = 1 + O(q), \end{aligned} \quad (2.88)$$

in the $q \rightarrow 0$ limit the matrix elements of the operator e^{iqx} can be taken equal to the unity and the phase space for electron-hole excitations is $\int dk = q$ [Lip03], yielding

$$\text{Re} \left[\frac{\sigma(q, \omega)}{L} \right] = \frac{\pi e^2}{q^2} \sum_{k_n} \frac{q}{2\pi} \alpha_{k_n} q \delta(\omega - \alpha_{k_n} q), \quad (2.89)$$

where we have denoted with \sum_{k_n} the sum over all the allowed intrasubband excitations. This amounts to count the number of cuts of the chemical potential with partially occupied subbands corresponding to positive values of α_{k_n} . Taking the cosine Fourier transform, we get

$$\text{Re} \left[\frac{\sigma(y, \omega)}{L} \right] = \frac{e^2}{2\pi} \sum_{k_n} \cos \left(\frac{\omega y}{\alpha_{k_n}} \right). \quad (2.90)$$

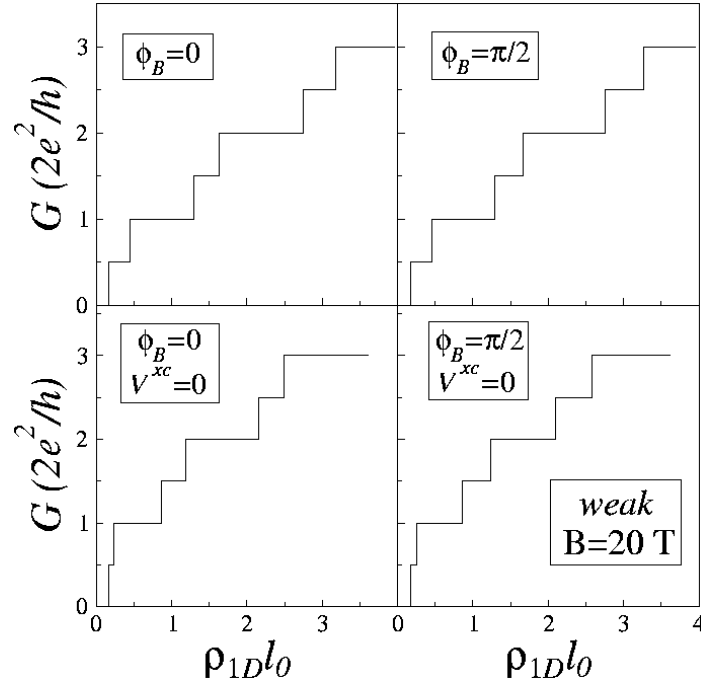


Figure 2.12: Conductance (in G_0 units) as a function of the linear density ρ_{1D} for $B = 20$ T in the weak SO regime. The azimuthal angle of the magnetic field is indicated. Top (bottom) panels show the results when the exchange-correlation interaction is (is not) taken into account.

Thus, in the $\omega \rightarrow 0$ limit, we finally obtain for the conductance:

$$G = \frac{e^2}{h} \sum_{k_n} 1 = \frac{G_0}{2} \sum_{k_n} 1. \quad (2.91)$$

When $V_{xc} = 0$, in the absence of magnetic field and spin-orbit coupling, $\epsilon_{nk} = (n + 1/2)\omega_0 + k^2/2$ and the subbands are spin-degenerate. Therefore, only one intrasubband excitation (one single intersection k_n) for each n contributes –by e^2/h – to the conductance, which thus presents the well-known quantization of the Landauer formalism, namely $G = \frac{G_0}{2} \sum_n 1$. However, different results may arise due to the combined effects of the magnetic field, spin-orbit coupling and V_{xc} on the energy spectrum.

Fig. 2.12 shows the conductance in the weak SO regime when a magnetic field is applied along the $\phi_B = 0$ and $\pi/2$ directions for the situations in which the exchange-correlation interaction is and is not considered. In both cases one can see the plateaus at semi-integer multiples of G_0 and notice as well the larger effect of V_{xc} at low densities. Indeed, the first semi-integer step is clearly wider when the exchange-correlation interaction is taken into account, showing how V_{xc} combines with B giving rise to a larger effective magnetic field. Note also that these steps are apparently narrower than those corresponding to integer multiples of G_0 since the splitting of the subbands due to the confinement –coming from the $(n + 1/2)\omega_0$ term– is much larger than the one induced by ‘ $\mathbf{B}_{V_{xc}}$ ’.

The corresponding strong SO regime is shown in Fig. 2.13. In this case, in addition to the steps at semi-integer values of G_0 , new features appear. Indeed, one can see

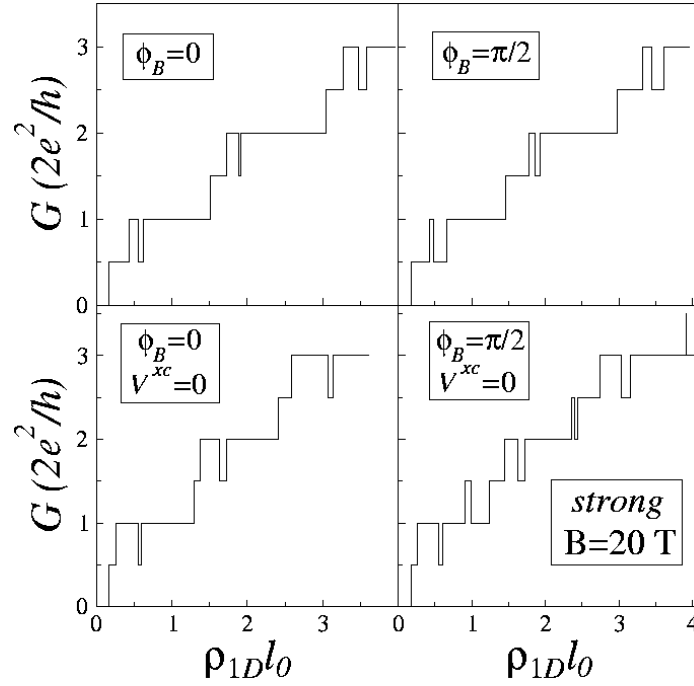


Figure 2.13: Same as Fig. 2.12 for the strong SO regime

that the conductance presents G_0 drops within narrow intervals of the electron density. These anomalies have already been found [Per04, Ser05] without considering the exchange-correlation interaction and are usually referred to as ‘anomalous conductance plateaus’. They are due to the interplay between the spin-orbit interaction and the magnetic field, which in some situations gives rise to the presence of energy gaps at odd-even subband intersections that may reduce the number of possible intrasubband excitations –or k_n points– by one unit. The effects of V_{xc} , dramatically depending on ρ_{1D} , can modify the size of such gaps thus altering the width of these additional plateaus. By comparing the left-top and the left-bottom panels, the latter corresponding to $V_{xc} = 0$ and $\phi_B = 0$, one can see that the inclusion of the exchange-correlation interaction does not alter the main structure of the conductance except for the width of the first semi-integer plateaus (similarly as in the weak SO case). However, new interesting features are found when $\phi_B = \pi/2$ and $V_{xc} = 0$: in this case, in addition to the above-mentioned drops, G presents also ‘bumps’ that increase its value by G_0 , again within small –even more in this case– intervals of ρ_{1D} . Their existence is due to the local maxima at even- n subbands discussed in the previous section that, contrarily as before, yield additional intrasubband excitations. It is worth to stress that these structures are not robust in the sense that they are washed out by the exchange-correlation interaction, as can be seen from the right-top panel of the figure. We also want to point out that, in the general case at $B \neq 0$, the same behavior is found for the subbands –and as a consequence for the conductance– when the angle of the magnetic field is changed from $\phi_B = 0$ to $\pi/2$ and viceversa, provided at the same time the interchanges $\Delta_R \leftrightarrow \Delta_D$ and $k \leftrightarrow -k$ are made. This is due to the particular interplay between the Rashba and Dresselhaus SO terms and the orientation of the magnetic field,

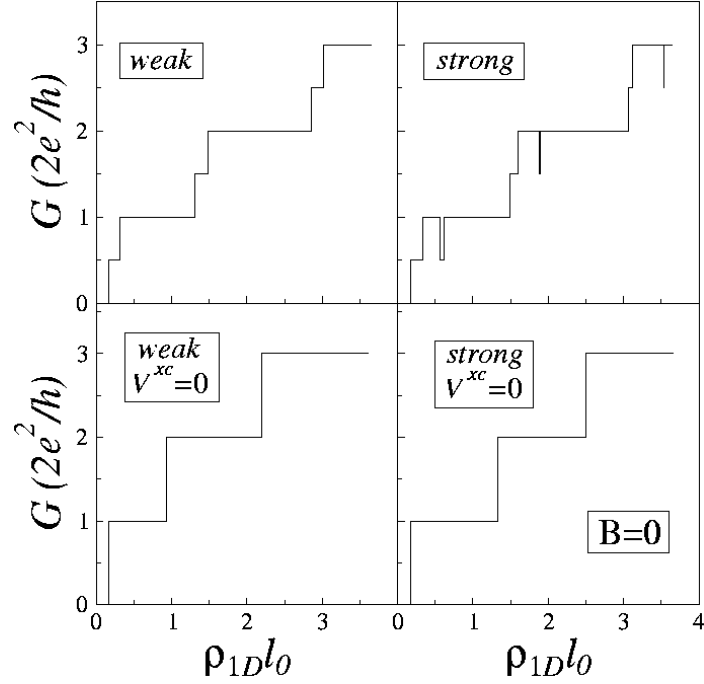


Figure 2.14: Same as Fig. 2.12 for $B = 0$ in the strong and weak SO regimes.

which is discussed in the Appendix B.

Finally, we show in Fig. 2.14 the $B = 0$ case for the weak and strong SO regimes. It can be seen that when $V_{xc} = 0$ the conductance displays the usual plateaus of the spin-degenerate situation (for each value of ρ_{1D} there are always two possible intrasubband excitations). Contrarily, when $V_{xc} \neq 0$ the induced splitting in the energy subbands (see fig. 2.10) gives rise to the presence of plateaus at semi-integer values of G_0 in the weak SO regime, and also of G_0 drops when the spin-orbit coupling is strong, similarly as what happens for $\mathbf{B} \neq 0$. This is clearly a genuine exchange-correlation interaction effect, mimicking an applied magnetic field.

Appendix A

Quantum wells with spin-orbit interaction under tilted magnetic fields

We generalize some of the expressions derived in section 2.1.1 to the case in which B has an in-plane component, namely e.g., $B = (B_x, 0, B_z)$. The Zeeman term then becomes $\frac{1}{2}g^*\mu_B\mathbf{B}\cdot\boldsymbol{\sigma} = -\frac{1}{2}\omega_L^z(\sigma_x \tan\theta + \sigma_z)$, where we have introduced the zenithal angle θ , with $\tan\theta = B_x/B_z$, and the ‘ z -Larmor’ frequency $\omega_L^z = |g^*\mu_B B_z|$, with $\omega_L^z/\omega_c = |g^*|m^*/2$. The Schrödinger equation reads now

$$\begin{bmatrix} \frac{1}{2}(a^+a^- + a^-a^+) - \omega_L^z/(2\omega_c) - \varepsilon & i\tilde{\lambda}_R a^- + \tilde{\lambda}_D a^+ - [\omega_L^z/(2\omega_c)] \tan\theta \\ -i\tilde{\lambda}_R a^+ + \tilde{\lambda}_D a^- - [\omega_L^z/(2\omega_c)] \tan\theta & \frac{1}{2}(a^+a^- + a^-a^+) + \omega_L^z/(2\omega_c) - \varepsilon \end{bmatrix} \begin{pmatrix} \phi_1 \\ \phi_2 \end{pmatrix} = 0 \quad . \quad (\text{A.1})$$

The calculation is performed as before, Eq. (2.7) becoming

$$\begin{aligned} (n + \alpha - \varepsilon) b_n - \frac{\alpha - \beta}{2} \tan\theta a_n - i\tilde{\lambda}_R \sqrt{n} a_{n-1} + \tilde{\lambda}_D \sqrt{n+1} a_{n+1} &= 0 \\ (n + \beta - \varepsilon) a_n - \frac{\alpha - \beta}{2} \tan\theta b_n + i\tilde{\lambda}_R \sqrt{n+1} b_{n+1} + \tilde{\lambda}_D \sqrt{n} b_{n-1} &= 0 \quad , \quad (\text{A.2}) \end{aligned}$$

where $\alpha = (1 + \omega_L^z/\omega_c)/2$ and $\beta = (1 - \omega_L^z/\omega_c)/2$.

Proceeding as in the perpendicular magnetic field situation, one finds the sp spectrum that generalizes Eqs. (2.28):

$$\begin{aligned} E_n^d &= \left(n + \frac{1}{2}\right) \omega_c + \frac{\omega_L^z}{2} \mathcal{S} + 2n \left[\mathcal{U} (\lambda_R^2 + \lambda_D^2) + (\lambda_R^2 \mathcal{V} + \lambda_D^2 \mathcal{Z}) \frac{\omega_c}{\omega_c + \omega_L^z} \mathcal{S} \right] \\ &\quad - 2(n+1) \left[\mathcal{U} (\lambda_R^2 + \lambda_D^2) + (\lambda_R^2 \mathcal{Z} + \lambda_D^2 \mathcal{V}) \frac{\omega_c}{\omega_c - \omega_L^z} \mathcal{S} \right] \\ E_n^u &= \left(n + \frac{1}{2}\right) \omega_c - \frac{\omega_L^z}{2} \mathcal{S} + 2n \left[\mathcal{U} (\lambda_R^2 + \lambda_D^2) + (\lambda_R^2 \mathcal{Z} + \lambda_D^2 \mathcal{V}) \frac{\omega_c}{\omega_c - \omega_L^z} \mathcal{S} \right] \\ &\quad - 2(n+1) \left[\mathcal{U} (\lambda_R^2 + \lambda_D^2) + (\lambda_R^2 \mathcal{V} + \lambda_D^2 \mathcal{Z}) \frac{\omega_c}{\omega_c + \omega_L^z} \mathcal{S} \right] \quad , \quad (\text{A.3}) \end{aligned}$$

where we have defined $\mathcal{S} = 1/\cos\theta$, $\mathcal{U} = \sin^2\theta/4$, $\mathcal{V} = (1 + \cos\theta)^2/4$, and $\mathcal{Z} = (1 - \cos\theta)^2/4$. Notice that when $\theta = 0$, $\mathcal{U} = \mathcal{Z} = 0$, $\mathcal{V} = 1$, and Eqs. (A.3) reduces to Eqs. (2.28).

Appendix B

Analytical second-order perturbation theory solution for noninteracting quantum wires

Noninteracting QWs in the presence of an in-plane magnetic field B have been addressed using second-order perturbation theory, considering only the Rashba term [Ser05]. We extend here these results taking into account both SO contributions. The Hamiltonian can be written in dimensionless form as

$$\begin{aligned} \frac{H_k}{\hbar\omega_0} = & \left(\hat{n}_k + \frac{1}{2} \right) + \frac{1}{2} \left(\frac{l_0}{l_Z} \right)^2 (\cos \phi_B \sigma_x + \sin \phi_B \sigma_y) + \frac{k^2 l_0^2}{2} \\ & + \frac{k l_0^2}{2} (\tilde{l}_D \sigma_x - \tilde{l}_R \sigma_y) + \frac{i l_0}{2\sqrt{2}} (\hat{a}_k^\dagger - \hat{a}_k) (\tilde{l}_R \sigma_x - \tilde{l}_D \sigma_y), \end{aligned} \quad (\text{B.1})$$

where $\tilde{l}_{R,D} \equiv l_{R,D}^{-1} \equiv 2m\lambda_{R,D}/\hbar^2$, $l_0 \equiv \sqrt{\hbar/m\omega_0}$, and $l_Z \equiv \sqrt{\hbar^2/mg^*\mu_B B}$, whereas \hat{a}_k^\dagger and \hat{a}_k are the usual creation and annihilation harmonic oscillator operators

$$\begin{aligned} \hat{a}_k^\dagger |nk\eta\rangle &= \sqrt{n+1} |(n+1)k\eta\rangle \\ \hat{a}_k |nk\eta\rangle &= \sqrt{n} |(n-1)k\eta\rangle, \end{aligned} \quad (\text{B.2})$$

with $\eta = \pm 1$. We split the Hamiltonian as $H_k = H_k^{(0)} + H_k^{SO}$ and consider the SO terms as a small perturbation. The other piece can be exactly solved yielding the unperturbed energies –in $\hbar\omega_0$ units– and eigenvectors

$$E_{nk\eta}^{(0)} = \left(n + \frac{1}{2} \right) + \frac{k^2 l_0^2}{2} + \frac{\eta}{2} \left(\frac{l_0}{l_Z} \right)^2 \quad (\text{B.3})$$

$$|nk\eta\rangle = \frac{1}{\sqrt{2}} \varphi_n(y) e^{ikx} \begin{pmatrix} 1 \\ \eta e^{i\phi_B} \end{pmatrix}. \quad (\text{B.4})$$

We have calculated the first- and second-order energy corrections arising from

$$H_k^{SO} = \frac{k l_0^2}{2} (\tilde{l}_D \sigma_x - \tilde{l}_R \sigma_y) + \frac{i l_0}{2\sqrt{2}} (\hat{a}_k^\dagger - \hat{a}_k) (\tilde{l}_R \sigma_x - \tilde{l}_D \sigma_y) \equiv H_{k,1}^{SO} + H_{k,2}^{SO}. \quad (\text{B.5})$$

The first-order correction is given by

$$\begin{aligned}
E_{nk\eta}^{(1)} &\equiv \langle nk\eta | H_k^{SO} | nk\eta \rangle \\
&= \frac{kl_0^2}{2} \left(\frac{1}{\sqrt{2}} \right)^2 \begin{pmatrix} 1 & \eta e^{-i\phi_B} \end{pmatrix} \begin{pmatrix} 0 & \tilde{l}_D + i\tilde{l}_R \\ \tilde{l}_D - i\tilde{l}_R & 0 \end{pmatrix} \begin{pmatrix} 1 \\ \eta e^{i\phi_B} \end{pmatrix} \\
&= \frac{kl_0^2}{2} \eta (\tilde{l}_D \cos \phi_B - \tilde{l}_R \sin \phi_B) .
\end{aligned} \tag{B.6}$$

As we can see, up to first order only $H_{k,1}^{SO}$ contributes, and setting $\lambda_D = 0$ we recover the result of Ref. [Ser05]. Note also that this correction is zero when the magnetic field is oriented along the direction corresponding to $\tan \phi_B = \lambda_D / \lambda_R$.

Interestingly, we see that up to first order the term that combines with the Zeeman contribution is the Dresselhaus one at $\phi_B = 0$, whereas it is the Rashba term at $\phi_B = \pi/2$, having opposite signs. This result is not sensibly altered by exchange-correlation effects, and helps to understand some of the detailed calculations shown in section 2.2.2. In particular, the conspicuous result that, for the same intensity of the SO interaction, the effect of the Dresselhaus term when $\phi_B = 0$ is the same as that of the Rashba term at $\phi_B = \pi/2$, provided that k is changed by $-k$.

Defining $|j\rangle \equiv |nk\eta\rangle$, the second-order correction is given by

$$E_j^{(2)} = \sum_{i \neq j} \frac{|\langle i | H_k^{SO} | j \rangle|^2}{E_j^{(0)} - E_i^{(0)}} = \sum_{i \neq j} \frac{|\langle i | H_{k,1}^{SO} + H_{k,2}^{SO} | j \rangle|^2}{E_j^{(0)} - E_i^{(0)}} , \tag{B.7}$$

with $|i\rangle \equiv |n'k\eta'\rangle$ since the perturbation is diagonal in k . Now both SO terms contribute. We distinguish different cases:

a) $|i\rangle = |nk\eta'\rangle$, with $\eta' = -\eta$. In this case, $\langle i | H_{k,2}^{SO} | j \rangle = 0$ and we have

$$E_j^{(0)} - E_i^{(0)} = \eta \left(\frac{l_0}{l_Z} \right)^2 \tag{B.8}$$

and

$$\begin{aligned}
\langle i | H_{k,1}^{SO} | j \rangle &= \left(\frac{1}{\sqrt{2}} \right)^2 \frac{kl_0^2}{2} \begin{pmatrix} 1 & -\eta e^{-i\phi_B} \end{pmatrix} \begin{pmatrix} 0 & \tilde{l}_D + i\tilde{l}_R \\ \tilde{l}_D - i\tilde{l}_R & 0 \end{pmatrix} \begin{pmatrix} 1 \\ \eta e^{i\phi_B} \end{pmatrix} \\
&= \frac{kl_0^2}{2} \eta i (\tilde{l}_D \sin \phi_B + \tilde{l}_R \cos \phi_B) .
\end{aligned} \tag{B.9}$$

This yields

$$E_{j,a}^{(2)} = \eta \frac{k^2 l_0^4}{4} \left(\frac{l_Z}{l_0} \right)^2 (\tilde{l}_D \sin \phi_B + \tilde{l}_R \cos \phi_B)^2 . \tag{B.10}$$

b) $|i\rangle = |n'k\eta\rangle$ with $n' \neq n$. Now, $\langle i | H_{k,1}^{SO} | j \rangle = 0$, and

$$E_j^{(0)} - E_i^{(0)} = n - n' , \tag{B.11}$$

yielding

$$\begin{aligned}
E_{j,b}^{(2)} &= \sum_{i \neq j} \frac{|\langle i | H_{k,2}^{SO} | j \rangle|^2}{E_j^{(0)} - E_i^{(0)}} \\
&= - \left| \frac{il_0}{2\sqrt{2} \cdot 2} \begin{pmatrix} 1 & \eta e^{-i\phi_B} \\ \tilde{l}_R - i\tilde{l}_D & 0 \end{pmatrix} \begin{pmatrix} 0 & \tilde{l}_R + i\tilde{l}_D \\ \tilde{l}_R - i\tilde{l}_D & 0 \end{pmatrix} \begin{pmatrix} 1 \\ \eta e^{i\phi_B} \end{pmatrix} \right|^2 \\
&= -\frac{l_0^2}{8} \left(\tilde{l}_D \sin \phi_B - \tilde{l}_R \cos \phi_B \right)^2 .
\end{aligned} \tag{B.12}$$

c) $|i\rangle = |n'k\eta'\rangle$ with $n' \neq n$ and $\eta' = -\eta$. Again, $\langle i | H_{k,1}^{SO} | j \rangle = 0$ and

$$E_j^{(0)} - E_i^{(0)} = n - n' + \eta \left(\frac{l_0}{l_Z} \right)^2 , \tag{B.13}$$

yielding

$$\begin{aligned}
E_{j,c}^{(2)} &= \sum_{i \neq j} \frac{|\langle i | H_{k,2}^{SO} | j \rangle|^2}{E_j^{(0)} - E_i^{(0)}} \\
&= \left| \frac{il_0}{2\sqrt{2} \cdot 2} \begin{pmatrix} 1 & -\eta e^{-i\phi_B} \\ \tilde{l}_R - i\tilde{l}_D & 0 \end{pmatrix} \begin{pmatrix} 0 & \tilde{l}_R + i\tilde{l}_D \\ \tilde{l}_R - i\tilde{l}_D & 0 \end{pmatrix} \begin{pmatrix} 1 \\ \eta e^{i\phi_B} \end{pmatrix} \right|^2 \\
&\quad \times \left[\frac{n+1}{-1 + \eta (l_0/l_Z)^2} + \frac{n}{1 + \eta (l_0/l_Z)^2} \right] \\
&= -\frac{l_0^2}{8} \left(\tilde{l}_R \sin \phi_B + \tilde{l}_D \cos \phi_B \right)^2 \left(\frac{1 + \eta (l_0/l_Z)^2 (2n+1)}{1 - (l_0/l_Z)^4} \right) .
\end{aligned} \tag{B.14}$$

The total second-order correction is therefore

$$\begin{aligned}
E_{nk\eta}^{(2)} &= E_{j,a}^{(2)} + E_{j,b}^{(2)} + E_{j,c}^{(2)} \\
&= \eta \frac{k^2 l_0^4}{4} \left(\frac{l_Z}{l_0} \right)^2 \left(\tilde{l}_D \sin \phi_B + \tilde{l}_R \cos \phi_B \right)^2 \\
&\quad - \frac{l_0^2}{8} \left[\tilde{l}_R^2 + \tilde{l}_D^2 + \left(\tilde{l}_R \sin \phi_B + \tilde{l}_D \cos \phi_B \right)^2 \frac{(l_0/l_Z)^4 + \eta (l_0/l_Z)^2 (2n+1)}{1 - (l_0/l_Z)^4} \right]
\end{aligned} \tag{B.15}$$

showing that both SO terms are entangled and contribute similarly at any angle. Setting $\lambda_D = 0$ we recover again the result of Ref. [Ser05].

Resum, conclusions i perspectives

En aquesta tesi hem estudiat l'estat fonamental, l'espectre d'excitació a l'infraroig llunyà i els efectes de la interacció d'spin-òrbita en nanoestructures quàntiques semiconductorres del tipus AlGaAs/GaAs. Ho hem fet en dos grans blocs diferenciats: un primer, centrant-nos exclusivament en sistemes d'anells quàntics, calculant l'estat fonamental i les respostes dipolars, i un segon bloc on hem estudiat els efectes dels acoblaments d'spin-òrbita de Bychkov-Rashba i de Dresselhaus en pous i fils quàntics sotmesos a camps magnètics aplicats externament, tant continguts en el pla del sistema com perpendiculars a aquest.

En el primer capítol hem utilitzat el formalisme de la *Local Spin-Density Approximation* (LSDA), i l'hem començat estudiant el cas d'un sol anell. Primerament, hem considerat el sistema com a tridimensional, és a dir amb un cert gruix en la direcció de creixement del pou quàntic inicial. El pla de l'anell ha estat descrit amb un potencial confinant mixte compost per una paràbola i una barrera quadrada d'alçada V_0 que hem pres de valor corresponent al *band-offset* de les heteroestructures considerades. Per altra banda, per a la direcció perpendicular al pla del sistema hem pres un pou quadrat de fondària també V_0 . Aquest sistema s'ha simplificat posteriorment a només dues dimensions prenent el mateix confinament en el pla però imposant que la densitat electrònica en la direcció vertical és una delta de Dirac.

La comparació de les energies d'addició dels dos sistemes mostra qualitativament els mateixos resultats: per una banda, els coneguts pics intensos als nombres d'electrons $N = 2, 6, 10, 20, \dots$, corresponents a tancaments de capa (amb spin total zero), i per l'altra els pics a $N = 4, 8, 16, \dots$, conseqüència de la regla de Hund, que com és ben sabut es compleix en aquests sistemes i afavoreix una configuració polaritzada en spin per ompliments de mitja capa. En el cas de tres electrons, però, hem trobat una diferència: l'anell bidimensional té spin màxim ($2S_z = 3$) a causa de la sobreestimació de l'energia d'intercanvi-correlació en dues dimensions. Cal dir, però, que aquest resultat no és un artifici de la LSDA, sinó que ha estat trobat també per altres autors mitjançant càlculs de diagonalització exacta.

Hem estudiat un segon anell bidimensional, modelitzat amb un confinament del tipus Woods-Saxon. En aquest cas hem considerat a més a més l'aplicació simultània d'un camp elèctric (\mathcal{E}) en el pla de l'anell i d'un camp magnètic (B) perpendicular a aquest. L'estudi d'aquest segon sistema ha fet palesa la gran dependència de l'espectre d'addició en la forma del potencial confinant, apreciant-se clares diferències respecte al primer anell.

No obstant això, en absència de camps aplicats hem trobat una gran robustesa dels pics a $N = 6, 8$ i 10 , amb la resta de l'espectre dibuixant en aquest cas un aspecte més pla. Hem vist també que fruit de l'aplicació dels camps externs apareixen puntualment nous pics –per exemple a $N = 2$ o 4 –, al mateix temps que l'estructura general s'aplana encara més, amb l'única excepció del pic a $N = 8$ que es mostra essencialment inalterat a qualssevol dels camps considerats. Hem comprovat també que l'efecte combinat de camps elèctrics i magnètics pot en alguns casos canviar l'spin total del sistema. Així, hem trobat transicions d'estats amb spin zero a d'altres de polaritzats en spin i viceversa fixant un dels dos camps i variant l'altre, propietat que ha estat observada experimentalment. Aquesta última l'hem estudiat també pel cas de dos electrons mitjançant la resolució exacta de l'equació d'Schrödinger. El corresponent diagrama de fases en el pla \mathcal{E} - B mostra clarament l'existència d'illes d'spin' separant regions d'estats singlet i triplet. Finalment, per a aquest anell hem calculat també la resposta dipolar en el canal de densitat amb el sistema sotmès a un camp magnètic fixat. Això últim ho hem fet utilitzant l'aproximació adiabàtica de la LSDA depenent del temps, trobant dues estructures ben definides en l'espectre infraroig llunyà: una a baixes energies i una altra –característica dels anells quàntics– corresponent a altes freqüències de la perturbació externa que origina l'excitació del sistema. En considerar l'aplicació del camp elèctric hem vist que cap de les dues estructures mostra canvis qualitius tot i la presència d'una petita fragmentació general i de l'aparició d'un petit *strength* a molt baixa energia.

Posteriorment, hem considerat dos anells tridimensionals acoblats verticalment, cadascun dels quals hem representat utilitzant el mateix potencial confinant que en el cas d'un sol anell, però ara amb dos pous quàntics en la direcció vertical separats per una distància d . La variació d'aquesta última ens ha permès estudiar, de manera similar a situacions amb molècules reals, diferents règims d'acoblament 'intramolecular'. Seguint aquesta analogia, i tenint en compte que en una possible futura realització experimental de tals sistemes hi haurà inevitablement introduïdes asimetries, hem considerat el cas en què els dos 'àtoms' són idèntics i el cas en què els pous quàntics o radis de cada anell difereixen en una certa quantitat.

En el cas 'homonuclear', mitjançant el càlcul de les energies d'addició hem trobat que a distàncies 'interatòmiques' petites ($d = 2$ nm) el sistema té un comportament qualitativament similar al d'un sol anell: els dos 'àtoms' es troben electrostàtica i quànticament lligats i es comporten com un sistema simple, amb pics pronunciats als valors d' N comentats més amunt. Quan augmentem la separació dels anells fins a una distància mitjana ($d = 4$ nm) l'espectre presenta una estructura més difusa, conservant alguns pics respecte al cas anterior i apareixent-ne de nous. La situació més interessant, no obstant això, és la corresponent a grans separacions ($d = 6$ nm), on la 'molècula' mostra signes inequívocs de dissociació: apareixen pics als mateixos valors d' N que en el cas d'un anell simple però multiplicats per dos, és a dir donant lloc, per exemple, a les combinacions $2+2 \rightarrow 4$, $6+6 \rightarrow 12$ o $10+10 \rightarrow 20$. Tot i això, la presència d'altres estructures més complexes indica que la distància més gran considerada no és suficient per donar lloc a una separació completa

de la molècula. La degeneració dels estats enllaçants i antienllaçants i, especialment, la possibilitat d'aquests de combinar-se en parelles donant lloc a localització electrònica en un anell o altre, té molt a veure amb els resultats obtinguts.

En el cas 'heteronuclear', hem considerat primer com a asimetria entre els dos pous una diferència de fondàries δ –*mismatch*– de l'ordre d'un 1% de V_0 . L'efecte trobat és gairebé inapreciable a distàncies petites i mitjanes, però esdevé molt important per a acoblaments petits, on δ és del mateix ordre que la diferència d'energies entre parelles d'estats enllaçants i antienllaçants. Això dona lloc a un espectre d'addició completament diferent al cas simètric i afavoreix clarament la gairebé total localització dels electrons en un dels dos anells. Quan hem considerat l'asimetria entre els dos radis, tot i considerar una diferència de l'ordre d'un 20% del valor del radi més petit, hem trobat efectes i conclusions similars, amb un espectre d'addició qualitativament igual al cas amb els pous desiguals i que sembla ser, doncs, característic d'aquests tipus de sistemes asimètrics.

Finalment, l'última part del capítol l'hem dedicat a l'estudi de sistemes dobles d'anells concèntrics. En un primer lloc, hem considerat els anells constituents representats per un potencial confinant tridimensional format per la superposició de dues corbes Gaussianes i prenent el radi de l'anell exterior com a variable. Posteriorment, hem considerat un confinament menys realista bidimensional, format per dues paràboles centrades a punts diferents, cadascuna de les quals representant un dels dos anells. En aquest darrer cas, la distància entre tots dos s'ha fixat i hem considerat com a paràmetre del sistema un camp magnètic variable aplicat en la direcció perpendicular al pla de moviment dels electrons.

En els sistemes concèntrics, a camp magnètic zero, la localització electrònica en un o altre anell és resultat de la competició entre l'energia cinètica, el confinament i la repulsió Coulombiana. Així doncs, en el cas tridimensional hem començat 'desconnectant' la interacció electró-electró per tal d'entendre millor els efectes de cada contribució. A la distància entre anells més petita considerada, hem trobat que els estats menys energètics es localitzen a l'anell més petit, desplaçant-se cap al més gran a mida que augmentem la separació entre tots dos. Pel que fa a les energies d'addició, aquestes mostren, tant per a petites com per a grans distàncies de separació, una estructura similar a la d'un sol anell –exceptuant òbviament els pics corresponents a ompliments de mitja capa degut a l'absència d'interacció de Coulomb i en particular de la part d'intercanvi-correlació. A distàncies mitjanes, en canvi, l'espectre mostra una nova estructura, amb variacions relatives entre els pics degudes a la quasi-degeneració dels estats corresponents a $n=0$ i $n=1$ i a les diferents respectives separacions energètiques entre valors de moment angular consecutius.

En considerar la interacció electró-electró, hem trobat que la transferència electrònica cap a l'anell de fora comença a separacions més petites que en el cas no-interactuant, com a conseqüència de la repulsió entre les partícules. Hem vist que, clarament, aquesta última esdevé molt crítica a l'hora de repartir els electrons entre els dos anells, especialment en el règim mitjà de separació, on trobem sistemes altament correlacionats. Aquest fet es reflexa en les energies d'addició, que mostren diferències evidents respecte al cas en què

no considerem la interacció de Coulomb, amb espectres totalment irregulars a aquestes distàncies. Una característica destacable que hem trobat per aquest sistema és que el terme d'intercanvi-correlació pot donar lloc a situacions en les quals l'anell de dins es troba totalment polaritzat en spin mentre que el de fora té spin zero.

En fixar els radis dels dos anells i considerar l'acció d'un camp magnètic perpendicular al pla del sistema, per la distància entre anells seleccionada hem trobat que la localització depèn altament de la intensitat del camp aplicat, i que en absència o per a valors petits d'aquest els electrons es troben essencialment deslocalitzats. Per altra banda, a mida que B augmenta –a partir d'uns 2 Tesla– trobem que els orbitals amb moment angular baix van distribuïnt-se a l'anell de dins mentre que els corresponents a l 's grans se'n van cap al de fora. Similarment al cas tridimensional, els dos anells tenen magnetitzacions d'spin diferents, donant lloc al fet que algunes parelles d'estats (spin amunt-spin avall) amb un l donat estiguin degenerades mentre que d'altres no ho estiguin, en funció de l'anell on es trobin majoritàriament localitzades. A més a més, per a valors grans de B amb el sistema totalment polaritzat en spin hem trobat una característica destacable: la presència en alguns casos d'orbitals desocupats amb veïns –és a dir l 's immediatament inferior i superior– ocupats, amb el 'radi' de l'estat buit corresponent aproximadament a la posició del màxim del potencial confinant (punt d'intersecció entre les dues paràboles).

Finalitzant el primer capítol, hem estudiat les respostes dipolars en els canals de càrrega i d'spin per al sistema bidimensional. En el cas deslocalitzat, és a dir a camps magnètics petits, l'espectre és bastant similar al conegut per un sol anell: hi ha modes d'excitació de *bulk* i d'*edge* a altes i baixes energies respectivament, amb els segons corresponent a les vores interna i externa de l'anell. En canvi, quan augmentem el camp magnètic, la conseqüent localització dels electrons en un o altre anell dóna lloc a un espectre molt més ric, amb nous modes d'*edge* de baixa energia associats a la vora externa de l'anell més petit i a la vora interna del més gran. Com a norma general, hem trobat que les excitacions en el canal de càrrega es troben a una energia més gran que en el d'spin a causa dels signes de les respectives interaccions residuals (lligada al terme de Coulomb directe –positiu– en el primer, i al d'intercanvi-correlació –negatiu– en el segon). Per alguns valors del camp magnètic, a més a més, trobem que ambdós modes estan acoblats, és a dir que l'operador dipolar de densitat excita modes en el canal d'spin i viceversa.

En el segon capítol hem començat estudiant els efectes dels acoblaments d'spin-òrbita de Rashba i de Dresselhaus en un pou quàntic sotmès a un camp magnètic perpendicular al pla que el conté. Ho hem fet mitjançant una aproximació analítica que té com a punt de partida l'expansió de les components dels spinors representant els estats del sistema en termes d'una base d'oscil·lador.

Quan només es considera una de les dues contribucions d'spin-òrbita, el problema té solució exacta, però no és així quan ambdues es tenen en compte. En aquest cas hem fet l'aproximació que un nivell donat $|n\rangle$ del sistema només s'acobla als nivells $|n-1\rangle$ i $|n+1\rangle$. D'aquesta manera, hem obtingut una solució analítica vàlida fins a segon ordre en les constants de Rashba i de Dresselhaus, l'aplicabilitat de la qual –tant per a grans com per

a petits camps magnètics– hem comprovat mitjançant la seva comparació amb la solució numèrica del problema. Així hem pogut obtenir uns nivells de Landau generalitzats, incorporant efectes d’spin-òrbita. Representant-los en funció de la intensitat relativa dels dos acoblaments respecte al terme de Zeeman, hem trobat que presenten creuaments deguts a la competició de les dues interaccions.

L’obtenció d’aquests nivells de Landau generalitzats ens ha permès també estudiar transicions de partícula independent induïdes per una perturbació externa depenent del temps, representada aquí per un camp electromagnètic d’una certa freqüència. D’aquesta manera hem pogut trobar les correccions a les energies de ciclotró i de Larmor degudes a la interacció d’spin-òrbita, així com a les excitacions degudes als operadors de densitat d’spin.

Posteriorment, hem estudiat els efectes d’afegir la interacció electró-electró en aquest sistema mitjançant una aproximació basada en les regles de suma. La consideració simultània de les interaccions de Coulomb i d’spin-òrbita ens ha permès poder explicar, calculant les regles de suma mixtes amb els operadors de ciclotró i de densitat d’spin, l’experimentalment observada dependència en el *filling factor* de l’*splitting* de la ressonància de ciclotró en aquests sistemes. En particular, trobem un *splitting* als valors senars $\nu = 3, 5$ i 7 i absència d’aquest per a valors parells de ν (quan l’estat fonamental té spin total zero). En el cas $\nu=1$, els dos operadors exciten els mateixos modes i els resultats obtinguts coincideixen amb les freqüències de ciclotró i de Larmor trobades quan no hem tingut en compte la interacció de Coulomb, donant lloc a un *splitting* nul.

Per acabar la secció, hem considerat la possibilitat que el camp magnètic aplicat tingui una component en el pla del sistema. Recalculant per a aquesta situació els nivells de Landau generalitzats i l’*splitting* de la ressonància de ciclotró, hem vist que la no-perpendicularitat del camp pot donar lloc a una amplificació dels efectes d’spin-òrbita en una mesura que depèn de les magnituds efectives –en particular de la massa i el factor giromagnètic– dels electrons de conducció del semiconductor considerat. L’efecte no és massa important en el cas del GaAs però sí ho pot ser, per exemple, per al InSb.

En la segona part del capítol hem estudiat els efectes de la interacció d’intercanvi-correlació, representada pel potencial V_{xc} , en fils quàntics sotmesos a un camp magnètic aplicat sobre el pla del sistema i amb presència d’acoblaments d’spin-òrbita de diferents intensitats. A causa d’aquests últims els spins del sistema són no-colineals, amb la seva orientació depenent de la posició espacial dins del fil i dels nombres quàntics dels estats electrònics. Per tant, en aquestes condicions la LSDA –que suposa d’entrada una direcció comú per a tots els spins del sistema– no és vàlida i hem hagut de recórrer a la seva versió generalitzada aplicable a aquestes situacions. Considerant a més a més l’aproximació d’apantallament total del terme de Coulomb directe, hem calculat les subbandes d’energia i la conductància del fil.

Hem trobat que les subbandes es veuen afectades per la interacció d’intercanvi-correlació en una mesura que depèn altament de la densitat del sistema i amb els efectes més grans a baixes densitats. En aquest règim, l’asimetria de les subbandes respecte al punt $k=0$,

així com els *gaps* als punts d'intersecció entre subbandes corresponents a transicions d' n senar a parell, es poden veure amplificats o modificats com a causa de l'efecte de V_{xc} . En general, hem trobat que aquest sembla actuar de manera anàloga a un camp magnètic, amb una intensitat i orientació que varien en funció de la configuració considerada i que hem trobat difícil de sistematitzar tot i que, com era d'esperar, té els efectes més grans a baixes densitats. Aquest 'camp magnètic' es manifesta tant en absència de camp aplicat externament com quan aquest últim és no nul donant lloc a un d'efectiu. Cal destacar una característica important de les subbandes i que desapareix quan s'inclou l'intercanvi-correlació: la presència de màxims locals en subbandes amb n parell quan es consideren valors intensos dels acoblaments d'spin-òrbita en combinació amb el camp magnètic.

Per acabar, hem calculat la conductància G del fil com a resposta lineal del sistema a l'aplicació en la seva direcció longitudinal d'un camp elèctric constant. Així, el valor de G per a un valor de la densitat donat s'infereix de la corresponent estructura de subbandes: cada possible excitació amb $\Delta n=0$ –dins d'una mateixa subbanda– contribueix en la unitat fonamental G_0 . D'aquesta manera, a camp magnètic nul hem trobat, com a efecte de l'intercanvi-correlació, la presència d'esglaons a múltiples semi-enteros de G_0 i, per a acoblaments d'spin-òrbita intensos, també de les conegudes caigudes de valor G_0 en la conductància que donen lloc als sovint anomenats 'esglaons anòmals' per a petits intervals de la densitat. En considerar un camp magnètic extern trobem, a més a més, la presència de nous esglaons anòmals deguts a l'existència dels màxims locals comentada anteriorment. Aquests es manifesten com a 'bons' d'alçada G_0 , també per a petits valors de la densitat i novament amb els efectes més grans a baixes densitats. A diferència dels primers esglaons anòmals, que es mostren essencialment robustos contra l'efecte de l'intercanvi-correlació, els segons desapareixen quan aquesta última interacció s'inclou en els càlculs.

Com a continuació del treball exposat en aquesta tesi, hi ha diverses possibilitats. Per una banda, hem començat ja l'estudi dels anells acoblats verticalment considerant el sistema sota l'efecte d'un camp magnètic aplicat perpendicularment i que es podria considerar amb una orientació arbitrària. Això pot donar lloc a la presència de 'fases d'isospí' en funció de la intensitat del camp extern i de la distància de separació entre els dos anells, que podrien ser observades experimentalment.

Per altra banda, els anells concèntrics es poden estudiar amb tècniques de diagonalització exacta fent servir com a base els estats obtinguts amb la LSDA. La idea és veure els possibles efectes de localització electrònica, tant radial com angular, en funció de la separació entre els anells o de la intensitat d'un camp magnètic aplicat. Aquesta localització podria donar lloc a configuracions que es podrien manifestar experimentalment en l'espectre d'excitació del sistema. Aquest últim, a més, es pot calcular utilitzant la versió dependent del temps de la LSDA, permetent una comparació amb els resultats obtinguts de la diagonalització. Els efectes de les oscil·lacions d'Aharonov-Bohm, especialment en el cas dels anells concèntrics feblement acoblats, també poden ser de gran interès. A més a més, els càlculs presentats aquí es poden estendre a excitacions de més alta polaritat

o considerar-ne de provinents d'operadors d'ona plana, no només en el cas considerat bidimensional, sinó també prenent un confinament més realista en tres dimensions.

Concernint els efectes de l'acoblament d'spin-òrbita, el formalisme utilitzat per estudiar els pous quàntics es pot aplicar a punts i fils quàntics sota l'acció d'un camp magnètic perpendicular. La consideració, a més, d'un camp elèctric aplicat sobre el pla del sistema ens permetria calcular la magnetoconductivitat longitudinal i transversal, podent-ne estudiar els efectes induïts per les interaccions de Rashba i/o Dresselhaus. En aquest cas caldria recórrer al teorema de Kohn generalitzat, vàlid quan el confinament que forma el punt o el fil quàntic és parabòlic.

Finalment, el formalisme de la LSDA no-colineal es podria aplicar a l'estudi de sistemes més complexos, com per exemple un fil atravesant una 'illa' amb presència de les interaccions d'spin-òrbita i/o d'intercanvi-correlació. Això simularia un punt o un anell quàntic 'obert' on el fil faria el paper d'uns contactes elèctrics que en un muntatge experimental serien necessàriament presents per tal de poder mesurar, per exemple, la conductivitat del sistema. Aquesta generalització de la LSDA es podria aplicar també a sistemes d'anells quàntics, estudiant el seu estat fonamental i també el seu espectre d'excitació.

Bibliography

- [Abr72] *Handbook of mathematical functions*, M. Abramowitz and I. A. Stegun, Eds. (Dover, New York 1972).
- [Aha59] Y. Aharonov and D. Bohm, Phys. Rev. **115**, 485 (1959).
- [Aic06] M. Aichinger, S.A. Chin, E. Krotscheck, and E. Räsänen, Phys. Rev. B **73**, 195310 (2006).
- [Ale01] I.L. Aleiner and V. I. Fal'ko, Phys. Rev. Lett. **87**, 256801 (2001).
- [Ama01] S. Amaha, D.G. Austing, Y. Tokura, K. Muraki, K. Ono, and S. Tarucha, Solid State Commun. **119**, 183 (2001).
- [Anc03] F. Ancilotto, D.G. Austing, M. Barranco, R. Mayol, K. Muraki, M. Pi, S. Sasaki, and S. Tarucha, Phys. Rev. **B67**, 205311 (2003).
- [And82] T. Ando, A.B. Fowler and F. Stern, Rev. Mod. Phys. **54**, 437 (1982).
- [And99] E. de Andrada e Silva, Phys. Rev. B **60**, 8859 (1999).
- [Asa98] Y. Asano, Phys. Rev. B **58**, 1414 (1998).
- [Ash93] R.C. Ashoori, H.L. Stormer, J.S. Weiner, L. N. Pfeiffer, K.W. Baldwin, and K.W. West, Phys. Rev. Lett. **71**, 613 (1993).
- [Att02] C. Attacalite, S. Moroni, P. Gori-Giorgi, and G.B. Bachelet, Phys. Rev. Lett. **88**, 256601 (2002); Erratum *ibid.* **91**, 109902 (2003).
- [Aus04] D.G. Austing, S. Tarucha, H. Tamura, K. Muraki, F. Ancilotto, M. Barranco, A. Emperador, R. Mayol, and M. Pi, Phys. Rev. B **70**, 045324 (2004).
- [Bar72] U. von Barth and L. Hedin, J. Phys. C **5**, 1629 (1972).
- [Bar94] M. Barranco and E. S. Hernández, Phys. Rev. B **49**, 12078 (1994).
- [Bar00] M. Barranco, L. Colletti, E. Lipparini, A. Emperador, M. Pi, and Ll. Serra, Rev. B **61**, 8289 (2000).
- [Bar01] K. Barnham and D. Vvedensky, *Low-dimensional semiconductor structures* (Cambridge University Press, U.K. 2001).

- [Bay03] M. Bayer, M. Korkusinski, P. Hawrylak, T. Gutbrod, M. Michel, and A. Forchel, *Phys. Rev. Lett.* **90**, 186801 (2003).
- [Bim98] Dieter Bimberg, M. Grundman, and N.N. Ledentsov, *Quantum dot heterostructures* (John Wiley & Sons, U.K. 1999).
- [Boh79] O. Bohigas, A.M. Lane, and J. Martorell, *Phys. Rep.* **51**, 267 (1979).
- [Bou00] P. Boucaud, J.B. Williams, K.S. Gill, M.S. Sherwin, W.V. Schoenfeld, and P.M. Petroff, *Appl. Phys. Lett.* **77**, 4356 (2000).
- [Bur97] G. Burkard, G. Seelig, and D. Loss, *Phys. Rev. B* **56**, 15 760 (1997).
- [Bur99] G. Burkard, D. Loss, and D.P. DiVincenzo, *Phys. Rev. B* **59**, 2070 (1999).
- [Bur00] G. Burkard, G. Seelig, and D. Loss, *Phys. Rev. B* **62**, 2581 (2000).
- [But83] M. Büttiker, Y. Imry, and R. Landauer, *Phys. Lett. A* **96**, 365 (1983).
- [Byc84] Y.A. Bychkov and E.I. Rashba, *Sov. Phys.-JETP Lett.* **39**, 78 (1984).
- [Cal05] M. Califano, T. Chakraborty, and P. Pietilainen, *Phys. Rev. Lett.* **94**, 246801 (2005).
- [Can99] C-M. Hu, J. Nitta, T. Akazaki, H. Takayanagai, J. Osaka, P. Pfeffer, and W. Zawadzki, *Phys. Rev. B* **60**, 7736 (1999).
- [Cep78] D.M. Ceperley, *Phys. Rev. B* **18**, 3126 (1978).
- [Cha94] T. Chakraborty and P. Pietiläinen, *Phys. Rev. B* **50**, 8460 (1994).
- [Cio01] M. Ciorga, A.S. Sachrajda, P. Hawrylak, C. Gould, P. Zawadzki, Y. Feng, and Z. Wasilewski, *Physica E* **11**, 35 (2001).
- [Cio02] M. Ciorga, A. Wensauer, M. Pioro-Ladriere, M. Korkusinski, J. Kyriakidis, A.S. Sachrajda, and P. Hawrylak, *Phys. Rev. Lett.* **88**, 256804 (2002).
- [Cio03] M. Ciorga, A.S. Sachrajda, and P. Hawrylak, *J. Supercond.* **16**, 743 (2003).
- [Cli03] J.I. Climente, J. Planelles, and W. Jaskolski *Phys. Rev. B* **68**, 075307 (2003).
- [Cli05] J.I. Climente, J. Planelles, and F. Rajadell, *J. Phys.: Condens. Matter* **17**, 1573 (2005).
- [Cli06] J.I. Climente, J. Planelles, M. Barranco, F. Malet, and M. Pi, *Phys. Rev. B* **73**, 235327 (2006).
- [Dah93] C. Dahl, J.P. Kotthaus, H. Nickel, and W. Schlapp, *Phys. Rev. B* **48**, 15 480 (1993).

- [Das90] B. Das, S. Datta and R. Reifengerger, Phys. Rev. B **41**, 8278 (1990).
- [Dav97] H.D.M. Davies, J.C. Harris, J.F. Ryan, and A.J. Turberfield, Phys. Rev. Lett. **78**, 4095 (1997).
- [Deb05] S. Debal and B. Kramer, Phys. Rev. B **71**, 115322 (2005).
- [Dre55] G. Dresselhaus, Phys. Rev. **100**, 580 (1955).
- [Dob88] M. Dobers, K. v. Klitzing, and G. Weimann, Phys. Rev. B **38**, 5453 (1988).
- [Dun00] D.S. Duncan, D. Goldhaber-Gordon, R.M. Westervelt, K.D. Maranowski, and A.C. Gossard, Appl. Phys. Lett. **77**, 2183 (2000).
- [Emp99] A. Emperador, M. Barranco, E. Lipparini, M. Pi, and Ll. Serra, Phys. Rev. B **59**, 15 301 (1999).
- [Emp00] A. Emperador, M. Pi, M. Barranco, and A. Lorke, Phys. Rev. B **62**, 4573 (2000).
- [Emp01] A. Emperador, M. Pi, M. Barranco, and E. Lipparini, Phys. Rev. B **64**, 155304 (2001).
- [Eri99] M.A. Eriksson, A. Pinczuk, B.S. Dennis, S.H. Simon, L.N. Pfeiffer, and K.W. West, Phys. Rev. Lett. **82**, 2163 (1999).
- [Fal93] V.I. Fal'ko, Phys. Rev. B **46**, R4320 (1992).
- [Fer94] M. Ferconi and G. Vignale, Phys. Rev. B **50**, 14722 (1994).
- [Fol01] J.A. Folk, C.M. Marcus, R. Berkovits, I.L. Kurland, I.L. Aleiner, and B.L. Altshuler, Physica Scripta **T90**, 26 (2001).
- [Fol01b] J. A. Folk, S.R. Patel, K.M. Birnbaum, C.M. Marcus, C.I. Duruöz, and J.S. Harris, Jr, Phys. Rev. Lett. **86**, 2102 (2001).
- [Fol05] P. Földi, B. Molnár, M.G. Benedict and F.M. Peeters, Phys. Rev. B **71**, 033309 (2005).
- [Fri05] M. Frigo and S.G. Johnson, 'The Design and Implementation of FFTW3', Proceedings of the IEEE **93** (2), 216 (2005).
- [Fuh01] A. Fuhrer, S. Lüscher, T. Ihn, T. Heinzl, K. Ensslin, W. Wegscheider, and M. Bichler, Nature **413**, 822 (2001). T. Ihn, A. Fuhrer, T. Heinzl, K. Ensslin, W. Wegscheider, and M. Bichler, Physica E **16**, 83 (2003).
- [Fuh03] A. Fuhrer, T. Ihn, K. Ensslin, W. Wegscheider, and M. Bichler, Phys. Rev. Lett. **91**, 206802 (2003).

- [Fus04] G. Fuster, M. Pacheco, and Z. Barticevic, *Braz. J. Phys.* **34**, 666 (2004).
- [Gov02] M. Governale and U. Zülicke, *Phys. Rev. B* **66**, 073311 (2002).
- [Gra05] D. Granados, J.M. García, T. Ben, and S.I. Molina, *Appl. Phys. Lett.* **86**, 071918 (2005).
- [Gud95] V. Gudmundsson, A. Brataas, P. Grambow, B. Meurer, T. Kurth, and D. Heitmann, *Phys. Rev. B* **51**, 17744 (1995).
- [Hal96] V. Halonen, P. Pietiläinen, and T. Chakraborty, *Europhys. Lett.* **33**, 377 (1996).
- [Hal01] B.I. Halperin, A. Stern, Y. Oreg, J.N.H.J. Cremers, J.A. Folk, and C.M. Marcus, *Phys. Rev. Lett.* **86**, 2106 (2001).
- [Han01] A.E. Hansen, A. Kristensen, S. Pedersen, C.B. Sorensen, and P.E. Lindelof, *Phys. Rev. B* **64**, 45327 (2001).
- [Han03] R. Hanson, B. Witkamp, L.M.K. Vandersypen, L.H.Willems. van Beveren, J.M. Elzerman, and L.P. Kouwenhoven, *Phys. Rev. Lett.* **91**, 196802 (2003).
- [Har99] P.Harrison, *Quantum wells, wires and dots* (John Wiley & Sons, U.K. 1998).
- [Hau04] H. Haug and S.W. Koch, *Quantum Theory of the Optical and Electronic Properties of Semiconductors*, 4th. edition (World Scientific, Singapore 2004).
- [Hei99] O. Heinonen, J. M. Kinaret, and M. D. Johnson, *Phys. Rev. B* **59**, 8073 (1999).
- [Hoh64] P. Hohenberg and W. Kohn, *Phys. Rev. B* **136**, 864 (1964).
- [Hu96] J. Hu, E. Dagotto, and A. H. MacDonald, *Phys. Rev. B* **54**, 8616 (1996).
- [Hu00] X. Hu and S. DasSarma, *Phys. Rev. A* **61**, 062301 (2000).
- [Hut03] A.K. Hüttel, H. Quin, A.W. Holleitner, R.H. Blick, K. Neumaier, D. Weinmann, K. Eberl, and J.P. Kotthaus, *Europhys. Lett.* **62**, 712 (2003).
- [Ihn03] T. Ihn, A. Fuhrer, T. Heinzl, K. Ensslin, W. Wegscheider, and M. Bichler, *Physica E* **16**, 83 (2003).
- [Ihn05] T. Ihn, A. Fuhrer, K. Ensslin, W. Wegscheider, and M. Bichler, *Physica E* **26**, 225 (2005).
- [Jac98] L. Jacak, P. Hawrylak and A. Wójs, *Quantum dots* (Springer-Verlag, Berlin 1998).
- [Jac04] D. Jacob, B. Wunsch, and D. Pfannkuche, *Phys. Rev. B* **70**, 081314(R) (2004).
- [Jou00] B. Jouault, G. Santoro, and A. Tagliacozzo, *Phys. Rev. B* **61**, 10242 (2000).

- [Kal84] C. Kallin and B.I. Halperin, Phys. Rev. B **30**, 5655 (1984).
- [Kan00] M. Kang, A. Pinczuk, B.S. Dennis, M.A. Eriksson, L.N. Pfeiffer, and K.W. West, Phys. Rev. Lett. **84**, 546 (2000).
- [Kit05] C. Kittel, *Introduction to Solid State Physics* (John Wiley & Sons, U.S.A. 2005).
- [Kna96] W. Knap, C. Skierbiszewski, A. Zduniak, E. Litwin-Staszewska, D. Bertho, F. Kobbi, J. L. Robert, G. E. Pikus, F. G. Pikus, S. V. Iordanskii, V. Mosser, K. Zekentes and Yu. B. Lyanda-Geller, Phys. Rev. B **53**, 3912 (1996).
- [Kno05] J. Knobbe and Th. Schäpers, Phys. Rev. B **71**, 035311 (2005).
- [Koc99] Wolfram Koch and Max C. Holthausen, *A chemist's guide to Density Functional Theory*, Wiley-Vch (1999).
- [Koh65] W. Kohn and L.J Sham, Phys. Rev. A **140**, 1133 (1965).
- [Kon05] J. Könenmann, R.J. Haug, D.K. Maude, V.I. Fal'ko, and B.L. Altshuler, Phys. Rev. Lett. **94**, 226404 (2005).
- [Koo90] S.E. Koonin and D.C. Meredith, *Computational Physics* (Addison-Wesley, 1990).
- [Kos97] M. Koskinen, M. Manninen, and S.M. Reimann, Phys. Rev. Lett. **79**, 1389 (1997).
- [Kos01] M. Koskinen, M. Manninen, B. Mottelson, and S.M. Reimann Phys. Rev. B **63**, 205323 (2001).
- [Kou97] L.P. Kouwenhoven, T.H. Oosterkamp, M.W.S. Danoesastro, M. Eto, D.G. Austing, T. Honda, and S. Tarucha, Science **278**, 1788 (1997).
- [Kur05] T. Kuroda, T. Mano, T. Ochiai, S. Sanguinetti, K. Sakoda, G. Kido, and N. Koguchi, Phys. Rev. B **72**, 205301 (2005).
- [Kyr02] J. Kyriakidis, M. Pioro-Ladriere, M. Ciorga, A.S. Sachrajda, and P. Hawrylak, Phys. Rev. B **66**, 035320 (2002).
- [Le96] N.N. Ledentsov, V.A. Shchukin, M. Grundmann, N. Kirstaedter, J. Böhrer, O. Schmidt, D. Bimberg, V.M. Ustinov, A. Yu. Egorov, A.E. Zhukov, P.S. Kop'ev, S.V. Zaitsev, N.Yu. Gordeev, Zh.I. Alferov, A.I. Borovkov, A.O. Kosogov, S.S. Ruvimov, P. Werner, U. Gösele, and J. Heydenreich, Phys. Rev. B **54**, 8743 (1996).
- [Lee04] B.C. Lee and C.P. Lee, Nanotechnology **15**, 848 (2004).

- [Li05] S.S. Li, and J.B. Xia, *J. Appl. Phys.* **89**, 3434 (2001); A. Puente, and Ll. Serra, *Phys. Rev. B* **63**, 125334 (2001); J.I. Climente, J. Planelles, and F. Rajadell, *J. Phys.: Condens. Matter* **17**, 1573 (2005).
- [Lin01] J.C. Lin and G.Y. Guo, *Phys. Rev. B* **65**, 035304 (2001).
- [Lin02] S. Lindemann, T. Ihn, T. Heinzel, W. Zwerger, K. Ensslin, K.D. Maranowski, and A.C. Gossard, *Phys. Rev. B* **66**, 195314 (2002).
- [Lip89] E. Lipparini and S. Stringari, *Phys. Rep.* **175**, 103 (1989).
- [Lip99] E. Lipparini, M. Barranco, A. Emperador, M. Pi, and Ll. Serra, *Phys. Rev. B* **60**, 8734 (1999).
- [Lip03] E. Lipparini, *Modern Many Particle Physics-Atomic Gases, Quantum Dots and Quantum Fluids* (World Scientific, Singapore 2003).
- [Lom85] G. Lommer, F. Malcher and U. Rössler, *Phys. Rev. B* **32**, 6965 (1985).
- [Lor00] A. Lorke, R.J. Luyken, A.O. Govorov, J.P. Kotthaus, J.M. Garcia, and P.M. Petroff, *Phys. Rev. Lett.* **84**, 2223 (2000).
- [Los98] D. Loss and D.P. DiVincenzo, *Phys. Rev. A* **57**, 120 (1998).
- [Lun83] S. Lundqvist, *Theory of the Inhomogeneous Electron Gas*, edited by S. Lundqvist and N. H. March (Plenum, New York, 1983).
- [Lus01] S. Lüscher, T. Heinzel, K. Ensslin, W. Wegscheider, and M. Bichler, *Phys. Rev. Lett.* **86**, 2118 (2001).
- [Mal86] F. Malcher, G. Lommer, and U. Rössler, *Superlattices and Microstructures* **2**, 267 (1986); G. Lommer, F. Malcher, and U. Rössler, *ibid.* **2**, 273 (1986).
- [Mal00] A.G. Mal'shukov and K.A. Chao, *Phys. Rev. B* **61**, R2413 (2000).
- [Mal05] F. Malet, M. Pi, M. Barranco, and E. Lipparini, *Phys. Rev. B* **72**, 205326 (2005).
- [Mal06] F. Malet, E. Lipparini, M. Barranco, and M. Pi, *Phys. Rev. B* **73**, 125302 (2006).
- [Man01] M. Manger, E. Batke, R. Hey, K.J. Friedland, K. Köhler, and P. Ganser, *Phys. Rev. B* **63**, 121203(R) (2001).
- [Man05] T. Mano, T. Kuroda, S. Sanguinetti, T. Ochiai, T. Tateno, J. Kim, T. Noda, M. Kawabe, K. Sakoda, G. Kido and N. Koguchi, *Nanoletters* **5**, 425 (2005).
- [Mar00] L. Martín-Moreno, L. Brey, and C. Tejedor, *Phys. Rev. B* **62**, R10 633 (2000); D. Sánchez, L. Brey, and G. Platero, *ibid.* **64**, 235304 (2001).

- [Mat02] P. Matagne, J.P. Leburton, D.G. Austing, and S. Tarucha, *Phys. Rev. B* **65**, 085325 (2002).
- [May97] O. Mayrock, S.A. Mikhailov, T. Darnhofer, and U. Rössler, *Phys. Rev. B* **56**, 15 760 (1997).
- [Mil03] J.B. Miller, D.M. Zumbuhl, C.M. Marcus, Y.B. Lyanda-Geller, D. Goldhaber-Gordon, K. Campman, and A.C. Gossard, *Phys. Rev. Lett.* **90**, 076807 (2003).
- [Mir01] F. Mireles and G. Kirczenow, *Phys. Rev. B* **64**, 024426 (2001).
- [Mit99] V.V. Mitin, V.A. Kochelap, and M. A. Stroschio, *Quantum heterostructures: Microelectronics and optoelectronics* (Cambridge University Press, U.K. 1999).
- [Mor99] A.V. Moroz and C.H.W. Barnes, *Phys. Rev. B* **60**, 14 272 (1999).
- [Nit97] J. Nitta, T. Akazaki, H. Takayanagi and T. Enoki, *Phys. Rev. Lett.* **78**, 1335 (1997).
- [Ono02] K. Ono, D.G. Austing, Y. Tokura, and S. Tarucha, *Science* **297**, 1313 (2002).
- [Pal95] J.J. Palacios and P. Hawrylak, *Phys. Rev. B* **51**, 1769 (1995).
- [Par00] B. Partoens and F.M. Peeters, *Phys. Rev. Lett.* **84**, 4433 (2000); *Europhys. Lett.* **56**, 86 (2001).
- [Ped02] F. Pederiva, A. Emperador, and E. Lipparini, *Phys. Rev. B* **66**, 165314 (2002).
- [Per81] J. P. Perdew and A. Zunger, *Phys. Rev. B* **23**, 5048 (1981).
- [Per04] Y.V. Pershin, J.A. Nesteroff, and V. Privman, *Phys. Rev. B* **69**, 121306(R) (2004).
- [Pi98] M. Pi, M. Barranco, A. Emperador, E. Lipparini, and Ll. Serra, *Phys. Rev. B* **57**, 14 783 (1998).
- [Pi01] M. Pi, A. Emperador, M. Barranco, F. Garcias, K. Muraki, S. Tarucha, and D.G. Austing, *Phys. Rev. Lett.* **87**, 066801 (2001).
- [Pi01a] M. Pi, A. Emperador, M. Barranco, and F. Garcias, *Phys. Rev. B* **63**, 115316 (2001).
- [Pi04] M. Pi, F. Ancilotto, E. Lipparini, and R. Mayol, *Physica. E* **24**, 297 (2004).
- [Pi05] M. Pi, D.G. Austing, R. Mayol, K. Muraki, S. Sasaki, H. Tamura, and S. Tarucha, in *Trends in Quantum Dots Research*, P. A. Ling, editor p. 1 (Nova Science Pu. 2005).
- [Pie06] P. Pietiläinen and T. Chakraborty, *Phys. Rev. B* **73**, 155315 (2006).

- [Pik95] F.G. Pikus and G.E. Pikus, Phys. Rev. B **51**, 16928 (1995).
- [Pin66] D. Pines and P. Nozières, *The Theory of Quantum Liquids* (Benjamin, New York 1966).
- [Pla05] J. Planelles, and J.I. Climente, Eur. Phys. J. B **48**, 65 (2005).
- [Pro92] C.R. Proetto, Phys. Rev. B **46**, R16 174 (1992).
- [Pue99] A. Puente and Ll. Serra, Phys. Rev. Lett **83**, 3266 (1999).
- [Pue01] A. Puente and Ll. Serra, Phys. Rev. B **63**, 125334 (2001).
- [Rac97] P.N. Racec, T. Stoica, C. Popescu, M. Lepsa, and T.G. van de Roer, Phys. Rev. B **56**, 3595 (1997).
- [Raj78] A. K. Rajagopal, Phys. Rev. B **17**, 2980 (1978).
- [Ras60] E.I. Rashba, Fiz. Tverd. Tela (Leningrad) **2**, 1224 (1960) [Sov. Phys. Solid State **2**, 1109 (1960)].
- [Ras84] Yu. A. Bychkov and E.I. Rashba, J. Phys. C **17**, 6039 (1984).
- [Rei99] S.M. Reimann, M. Koskinen, and M. Manninen, Phys. Rev. B **59**, 1613 (1999).
- [Rei01] D. J. Reilly, G. R. Facer, A. S. Dzurak, B. E. Kane, R. G. Clark, P. J. Stiles, R. G. Clark, A. R. Hamilton, J. L. O'Brien, N. E. Lumpkin, L. N. Pfeiffer, and K. W. West, Phys. Rev. B **63**, R121311 (2001).
- [Rei02] S.M. Reimann and M. Manninen, Rev. Mod. Phys. **74**, 1283 (2002).
- [Ric99] D. Richards and B. Jusserand, Phys. Rev. B **59**, R2506 (1999).
- [Rok01] L.P. Rokhinson, L.J. Guo, S.Y. Chou, and D.C. Tsui, Phys. Rev. B **63**, 035321 (2001).
- [Ron98] M. Rontani, F. Rossi, F. Manghi, and E. Molinari, Appl. Phys. Lett. **72**, 957 (1998).
- [Ron99] M. Rontani, F. Rossi, F. Manghi, and E. Molinari, Solid State Commun. **112**, 151 (1999); M. Rontani, F. Troiani, U. Hohenester, and E. Molinari, *ibid.* **119**, 309 (2001); M. Rontani, S. Amaha, K. Muraki, F. Manghi, E. Molinari, S. Tarucha, and D.G. Austing, Phys. Rev. B. **69**, 085327 (2004).
- [Ron99b] M. Rontani, F. Rossi, F. Manghi, and E. Molinari, Phys. Rev. B **59**, 10165 (1999).
- [Sal01] G. Salis, D.D. Awschalom, Y. Ohno, and H. Ohno, Phys. Rev. B **64**, 195304 (2001).

- [Sch95] T. Schmidt, M. Tewordt, R.H. Blick, R.J. Haug, D. Pfannkuche, K. v. Klitzing, A. Förster, and H. Lüth, Phys. Rev. B **51**, 5570 (1995).
- [Sch03] J. Schliemann, J.C. Egues, and D. Loss, Phys. Rev. B **67**, 085302 (2003).
- [Sch03b] J. Schliemann, J. C. Egues, and D. Loss, Phys. Rev. Lett. **90**, 146801 (2003).
- [Ser89] Ll. Serra, F. Garcias, M. Barranco, J. Navarro, C. Balbás, A. Rubio, and A. Mañanes, J. Phys. Cond. Matt. **1**, 10391 (1989).
- [Ser99] Ll. Serra, M. Barranco, A. Emperador, M. Pi, and E. Lipparini, Phys. Rev. B **59**, 15 290 (1999).
- [Ser99b] Ll. Serra, M. Pi, A. Emperador, M. Barranco and E. Lipparini, Eur. Phys. J. D **9**, 643 (1999).
- [Ser05] Ll. Serra, D. Sánchez, and R. López, Phys. Rev. B **72**, 235309 (2005).
- [Sha04] E. Shafir, M. Shen, and S. Saikin, Phys. Rev. B **70**, 241302(R) (2004).
- [Sih04] V. Sih, W.H. Lau, R.C. Myers, A.C. Gossard, M.E. Flatté, and D.D. Awschalom, Phys. Rev. B **70**, 161313(R) (2004).
- [Sol96] G.S. Solomon, J.A. Trezza, A.F. Marshall, and J.S. Harris, Jr., Phys. Rev. Lett. **76**, 952 (1996).
- [Ste82] D. Stein, K. v. Klitzing, and G. Weimann, Phys. Rev. Lett. **51**, 130 (1982).
- [Sua04] F. Suárez, D. Granados, M.L. Dotor, and J.M. García, Nanotechnology **15**, S126 (2004).
- [Sza05] B. Szafran and F.M. Peeters, Phys. Rev. B **72** 155316 (2005).
- [Tan89] B. Tanatar and D.M. Ceperley, Phys. Rev. B **39**, 5005 (1989).
- [Tar96] S. Tarucha, D.G. Austing, T. Honda, R.J. van der Hage, and L.P. Kouwenhoven, Phys. Rev. Lett. **77**, 3613 (1996); S. Tarucha, D.G. Austing, Y. Tokura, W.G. van der Wiel, and L.P. Kouwenhoven, *ibid.* **84**, 2485 (2000).
- [Tar00] S. Tarucha, D.G. Austing, Y. Tokura, W.G. van der Wiel, and L.P. Kouwenhoven, Phys. Rev. Lett. **84**, 2485 (2000).
- [Tho96] K. J. Thomas, J. T. Nicholls, M. Y. Simmons, M. Pepper, D. R. Mace, and D. A. Ritchie, Phys. Rev. Lett. **77**, 135 (1996).
- [Tho04] K. J. Thomas, D.L. Sawkey, M. Pepper, W.R. Tribe, I. Farrer, M.Y. Simmons, and D.A. Ritchie J. Phys. Cond. Matt. **16**, L279 (2004).
- [Ton04] P. Tonello and E. Lipparini, Phys. Rev. B **70**, 081201(R) (2004).

- [Ull02] C.A. Ullrich and M.E. Flatté, Phys. Rev. B **66**, 205305 (2002).
- [Val02a] M. Valín-Rodríguez, A. Puente, Ll. Serra, and E. Lipparini, Phys. Rev. B **66**, 165302 (2002).
- [Val02b] M. Valín-Rodríguez, A. Puente, and Ll. Serra, Phys. Rev. B **66**, 045317 (2002).
- [Val02c] M. Valín-Rodríguez, A. Puente, Ll. Serra, and E. Lipparini, Phys. Rev. B **66**, 235322 (2002).
- [Val06] M. Valín-Rodríguez and R. G. Nazmitdinov, Phys. Rev. B **73**, 235306 (2006).
- [Vig88] G. Vignale and M. Rasolt, Phys. Rev. B **37**, 10685 (1988).
- [Vos00] A. Voskoboynikov, S.S. Liu, C.P. Lee, and O. Tretyak, J. App. Phys. **87**, 1 (2000).
- [Vos01] O. Voskoboynikov, C.P. Lee, and O. Tretyak, Phys. Rev. B **63**, 165306 (2001).
- [War00] R.J. Warburton, C. Schäfflein, D. Haft, F. Bickel, A. Lorke, K. Karrai, J.M. García, W. Schoenfeld, and P.M. Petroff, Nature **405**, 926 (2000).
- [Wei78] M. Weissbluth, *Atoms and Molecules* (Academic Press, New York 1978).
- [Wen96] L. Wendler, V. M. Fomin, A.V. Chaplik, and A.O. Govorov Phys. Rev. B **54**, 4794 (1996).
- [Wen99] W.T. Wenckebach, *Essentials of Semiconductor Physics* (John Wiley & Sons, U.K. 1999).
- [Wen00] A. Wensauer, O. Steffens, M. Suhrke, and U. Rössler, Phys. Rev. B **62**, 2605 (2000).
- [Wie03] W.G. van der Wiel, S. De Franceschi, J.M. Elzerman, T. Fujisawa, S. Tarucha, and L.P. Kouwenhoven, Rev. Mod. Phys. **75**, 1 (2003).
- [Zar96] E. Zaremba, Phys. Rev. B **53**, R10 512 (1996).
- [Zha06] S. Zhang, R. Liang, E. Zhang, L. Zhang, and Y. Liu, Phys. Rev. B **73**, 155316 (2006).
- [Zhu96] J.-L. Zhu, J.-Z. Yu, Z.-Q. Li, and Y. Kawazoe, J. Phys.: Condens. Matter **8**, 7857 (1996).
- [Zhu05] J.L. Zhu, S. Hu, Z. Dai, and X. Hu, Phys. Rev. B **72**, 075411 (2005).

Curriculum Vitae

Name: Francesc Malet Giralt

Birth: Barcelona. October 27, 1979

Academic degrees

1. Graduate in Physics. University of Barcelona, 2003.
2. PhD studies at Departament d'Estructura i Constituents de la Matèria, University of Barcelona. Biennium 05-07.

Publications in Journals

1. F. Malet, M. Pi, M. Barranco and E. Lipparini, *Ground state structure and conductivity of quantum wires of infinite length and finite width*, Phys. Rev. B **72**, 205326 (2005).
2. J.I. Climente, J. Planelles, M. Pi and F. Malet, *Magnetic-field dependence of hole levels in self-assembled InGaAs quantum dots*, Phys. Rev. B **72**, 233305 (2005).
3. F. Malet, E. Lipparini, M. Barranco and M. Pi, *Spin-orbit effects on the Larmor dispersion relation in GaAs quantum wells*, Phys. Rev. B **73**, 125302 (2006).
4. J.I. Climente, J. Planelles, M. Barranco, F. Malet and M. Pi, *Electronic structure of few-electron concentric double quantum rings*, Phys. Rev. B **73**, 235327 (2006).
5. F. Malet, M. Barranco, E. Lipparini, R. Mayol, M. Pi, J.I. Climente and J. Planelles, *Vertically coupled double quantum rings at zero magnetic field*, Phys. Rev. B **73**, 245324 (2006).
6. E. Lipparini, M. Barranco, F. Malet, M. Pi and Ll. Serra, *Spin-orbit effects in GaAs quantum wells: Interplay between Rashba, Dresselhaus, and Zeeman interactions*, Phys. Rev. B **74** 115303 (2006).

7. F. Malet, M. Pi, M. Barranco, E. Lipparini and Ll. Serra, *Optical response of two-dimensional few-electron concentric double quantum rings: A local-spin-density-functional theory study*, Phys. Rev. B **74** 193309 (2006).
8. F. Malet, M. Pi, M. Barranco, Ll. Serra and E. Lipparini, *Exchange-correlation effects on quantum wires with spin-orbit interactions under the influence of in-plane magnetic fields*, Phys. Rev. B **76** 115306 (2007).
9. F. Malet, M. Pi, M. Barranco, Ll. Serra and E. Lipparini, *Addition energies and density dipole response of quantum rings under the influence of in plane electric fields*, Phys. Rev. B **76** 245302 (2007).
10. F. Malet, M. Pi, M. Barranco, Ll. Serra and E. Lipparini, *Singlet-triplet transition of a two-electron quantum ring in magnetic and electric fields*, Physica E **40** 1492 (2008).

Publications in Proceedings

1. F. Malet, M. Barranco, E. Lipparini, R. Mayol, M. Pi, J.I. Climente i J. Planelles, *Vertical quantum ring molecules*, in *HPC-Europa*, Barcelona, 2005.
2. F. Malet, E. Lipparini, M. Barranco and M. Pi, *Spin-orbit effects on the Larmor dispersion relation in GaAs quantum wells*, in *HPC-Europa*, Barcelona, 2005.
3. F. Malet, M. Barranco, E. Lipparini, R. Mayol, M. Pi, J.I. Climente and J. Planelles, *Vertical homonuclear quantum ring molecules*, in *Physica Status Solidi C* **3**, 11 (3652-3655) (2006).

